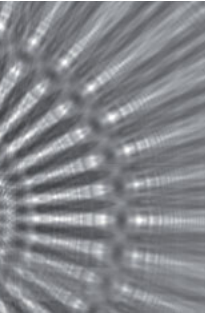
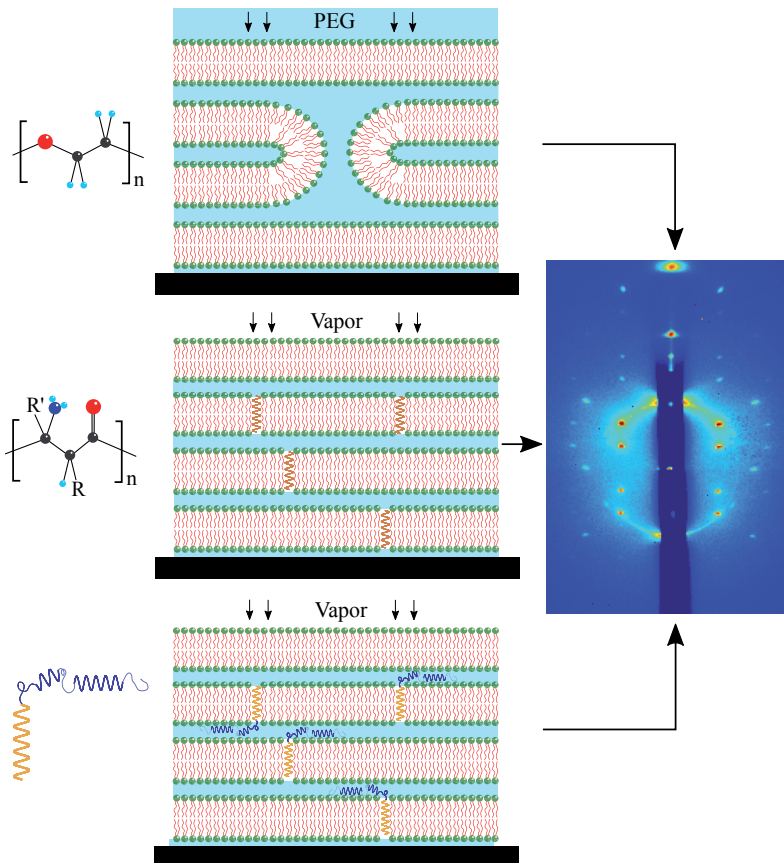




Göttingen Series in
X-ray Physics



Yihui Xu
Extending the X-ray Study of
Membrane Fusion in Supported Multibilayers
towards Physiological Conditions



Universitätsverlag Göttingen

Yihui Xu

Extending the X-ray Study of Membrane Fusion in Supported Multibilayers
towards Physiological Conditions

This work is licensed under a [Creative Commons Attribution-ShareAlike 4.0 International License](https://creativecommons.org/licenses/by-sa/4.0/).



Published in 2017 by Universitätsverlag Göttingen
as volume 22 in the series “Göttingen series in X-ray physics”

Yihui Xu

Extending the X-ray Study
of Membrane Fusion
in Supported Multibilayers
towards Physiological
Conditions

Göttingen series in X-ray physics
Volume 22



Universitätsverlag Göttingen
2017

Bibliographic information published by the Deutsche Nationalbibliothek

The Deutsche Nationalbibliothek lists this publication in the Deutsche Nationalbibliografie; detailed bibliographic data are available on the Internet at <http://dnb.dnb.de>.

This work was financially supported by SFB 803 “Functionality Controlled by Organization in and Between Membranes” of Deutsche Forschungsgemeinschaft (DFG)

Address of the Author

Yihui Xu

e-mail: yxu1@uni-goettingen.de

Dissertation

for the award of the degree

“Doctor of Philosophy”

Division of Mathematics and Natural Sciences

of the Georg-August-Universität Göttingen

within the doctoral program PBCS, GGNB

of the Georg-August University School of Science (GAUSS)

Thesis Committee:

Prof. Dr. Tim Salditt, Institut für Röntgenphysik, Universität Göttingen

Prof. Dr. Ulf Diederichsen, Institut für Organische und Biomolekulare Chemie, Universität Göttingen

Prof. Dr. Andreas Janshoff, Institut für Physikalische Chemie, Universität Göttingen

This work is protected by German Intellectual Property Right Law.

It is also available as an Open Access version through the publisher’s homepage and the Göttingen University Catalogue (GUK) at the Göttingen State and University Library (<http://www.sub.uni-goettingen.de>).

The license terms of the online version apply.

Set and layout: Yihui Xu

Cover: Jutta Pabst

Cover image: Yihui Xu

© 2017 Universitätsverlag Göttingen

<http://univerlag.uni-goettingen.de>

ISBN: 978-3-86395-304-1

DOI: <https://doi.org/10.17875/gup2017-1043>

ISSN: 2191-9860

Preface of the series editors

The Göttingen series in x-ray physics is intended as a collection of research monographs in x-ray science, carried out at the Institute for X-ray Physics at the Georg-August-Universität in Göttingen, and in the framework of its related research networks and collaborations.

It covers topics ranging from x-ray microscopy, nano-focusing, wave propagation, image reconstruction, tomography, short x-ray pulses to applications of nanoscale x-ray imaging and biomolecular structure analysis.

In most but not all cases, the contributions are based on Ph.D. dissertations. The individual monographs should be enhanced by putting them in the context of related work, often based on a common long term research strategy, and funded by the same research networks. We hope that the series will also help to enhance the visibility of the research carried out here and help others in the field to advance similar projects.

Prof. Dr. Tim Salditt
Prof. Dr. Sarah Köster
Editors
Göttingen June 2014

Preface to the present volume

Biomimetic lipid membranes are model systems for their more complex biological counterparts.

In a well controlled manner they allow us to study biomolecular structure, phase behavior and interactions of lipids, peptides and proteins the important self-assembled environment of fluid membranes. Interface sensitive x-ray scattering provides a powerful tool to analyze such systems with nanoscale resolution, preserving a clear distinction between lateral and vertical momentum transfer. That is, if the model membranes can be oriented on solid support. Unfortunately, there is a catch. The organic solvents required in spreading of the lipid films impede the incorporation of proteins, which would simply denature. Therefore, x-ray reflectivity and grazing incidence diffraction has been restricted to relatively simple multilamellar model systems consisting of lipids and small peptides, but excluding membrane proteins.

The present thesis, while addressing the important phenomenon of membrane fusion and teaching us about ‘magic lipid mixtures’ which promote membrane fusion, has made a surprising step forward: it shows how highly oriented protein-containing lipid multilamellar model systems can be prepared without solvent, simply from a vesicle suspension. This enables a new (x-ray) perspective of membrane protein assembly and interactions.

Prof. Dr. Tim Salditt

Contents

Introduction	1
1 Stalk formation in pure lipid bilayers in aqueous solutions	5
1.1 Principles of stalk formation in pure lipid bilayers	5
1.2 Search for the “magic lipid mixture”	9
1.3 Investigation of selected mixtures in PEG aqueous solutions . .	31
1.4 Summary and outlook	38
2 X-ray studies of transmembrane β-peptides	39
2.1 Fundamentals of β -peptides	40
2.2 Sample preparation	42
2.3 Sample characterization	45
2.4 Summary and outlook	55
3 Preparation of SNARE-reconstituted proteolmicelles, proteoliposomes and multibilayers	57
3.1 Fundamentals of SNAREs	57
3.2 Advantages of supported lipid multibilayers	59
3.3 Existing preparation methods of supported lipid multibilayers .	61
3.4 Expression and purification of SNAREs	63
3.5 SNARE reconstitution into supported multibilayers by sVS . . .	65
4 SAXS studies of SNARE-reconstituted proteomicelles and proteoliposomes	69
4.1 Beamline BM29	69
4.2 General SAXS theories	74
4.3 SAXS modeling and fitting of proteomicelles	75
4.4 SAXS modeling and fitting of pure lipid vesicles and SNARE-reconstituted proteoliposomes	82
4.5 Summary and outlook	98
5 X-ray characterizations of SNARE-reconstituted multibilayers	99
5.1 GISAXS characterizations of SNARE-reconstituted multibilayers at ID01	99
5.2 In-house x-ray reflectivity studies of SNARE-reconstituted multibilayers	106

5.3 In-house GISAXS investigations of SNARE-reconstituted multi-bilayers	114
5.4 Summary and outlook	118
6 Conclusion and outlook	121
Appendix	123
A.1 Major x-ray reflectivity measurements in Chap. 1	123
A.2 Filter parameters of the in-house reflectometer Wendi	124
A.3 Reflectivity curves of PC-PE-DOG 45:45:10	125
A.4 Reflectivity curves of PC-PE-Chol 40:40:20	126
A.5 Reflectivity curves of PC-PE-PIP ₂ 35:35:30	127
B.1 Preparation and fitting conditions of vesicles investigated in this work	128
B.2 The MATLAB code to fit micelle SAXS curves	129
B.3 The MATLAB code to fit vesicle SAXS curves	130
C.1 Estimation of N _{SNARE} per Micelle	131
C.2 Estimation of N _{SNARE} per Vesicle	132
D.1 Attenuator parameters of the in-house diffractometer Rosi . . .	133
Bibliography	135
Own publications	153
Acknowledgment	155
Curriculum vitae	157

Introduction

Many cellular and subcellular events such as virus infection [1], fertilization [2] and exocytosis [3] require two initially distinct bilayers to merge into one; this process is called membrane fusion [4, 5]. Lipid bilayers, however, do not fuse spontaneously with each other [3] due to the rather strong repulsive force between them. As a matter of fact, in *in vivo* membrane fusion is predominantly mediated by fusion proteins [6]. For instance, soluble *N*-ethylmaleimide-sensitive factor attachment protein receptors (SNAREs) are known to mediate vesicle fusion [7]. The assembly of SNARE four-helix bundles overcomes the repulsive force to bring opposing bilayers into proximity, and merges them into one [8, 9].

Although planar bilayers can evolve into fusion pores via different fusion pathways [10], the hemifusion stalk seems to be an indispensable intermediate structure in this process [11]. As shown in Fig. 1, the proximal leaflets of stalks are connected with each other, while the distal leaflets stay separated [3]. Soon after the stalk model was proposed, it was supported by many theoretical calculations [11] and simulations [12]. Finally, in 2002, YANG and HUANG [13] evidenced that stalk structures could be observed on model lipid bilayers under partial dehydration, which was the first direct experimental observation of the hemifusion stalk [14]. Moreover, 3d electron density maps were reconstructed from x-ray diffraction patterns, revealing the structure of stalks at the angstrom scale.

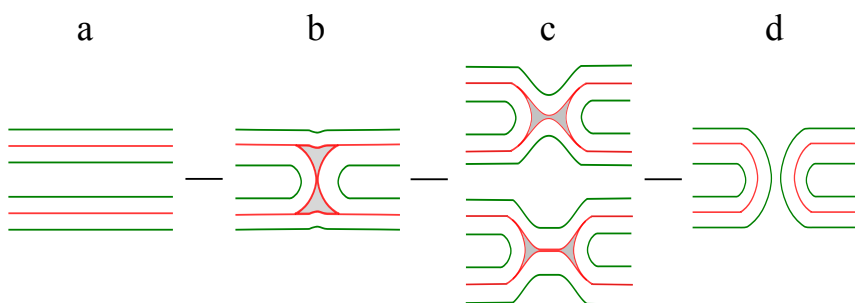


Figure 1: *Cartoon illustration of the membrane fusion pathway. (a) flat bilayers, (b) hemifusion stalk, (c) transmembrane contact/hemifusion diaphragm and (d) full fusion pore. The void space is colored gray. Reproduced from [3] with permission.*

Our group has long been devoted to the study of solid-supported lipid multibilayers under dehydration conditions, and many intrinsic physical properties

of lipid bilayers were investigated both experimentally [15, 16] and theoretically [17]. Our study has also been combined with molecular dynamic (MD) simulations which together offer a powerful toolkit for structural and energetical investigations of lipid bilayers [18]. With respect to stalk formation in particular, in the past the influence of some lipid species of great biological importance (e.g. cholesterol [19] and PIP₂ [20]) on stalk formation was carefully evaluated, taking advantage of our house-built vapor chamber where the relative humidity was precisely controlled. More recently, ÄFFNER *et al.* [21] systematically investigated the 3d structures of stalks of several common lipid compositions at increased spatial resolution, revealing that the favorable interbilayer distance of stalks is rather constant ($\sim 9 \text{ \AA}$) for all investigated compositions.

Fruitful results have been achieved with this simple humidity setup in pure lipid systems, and we now would like to extend this method to more complex systems closer to actual physiological conditions. To this end, two principle limitations of our current model system have to be overcome: (i) In our previous studies, the supported multibilayers were mounted in the vapor chamber where the desired osmotic pressure was facilitated by aqueous vapor. Despite the small amount of osmotic pressure induced by small molecules, biomembranes are normally not subject to such harsh dehydration. More importantly, in the vapor environment it is impossible to vary the physiological parameters such as ion strength and pH level. We thus would like to switch to aqueous solutions. For this purpose, we have to find an alternative route to facilitate osmotic pressure, and meanwhile search for a “*magic lipid mixture*” which is able to form stalks under mild dehydration of aqueous solutions. (ii) There are a wide variety of methods for the preparation of supported model lipid multibilayers. Previously, we were using the conventional spreading organic solution (sVS) method [15, 22] due to its high efficiency and convenience. In this protocol, lipids are first dissolved by organic solvents and then sprayed onto clean substrates. After solvent evaporation, highly oriented lipid stacks form on the substrates. However, organic solvent can lead to significant protein denaturation [23]. Consequently, the organic solvent method inhibits the reconstitution of fusion proteins into model multibilayers [24]. In order to study protein-mediated fusion in the multibilayer system, a new protocol has to be developed.

After this introduction, *Chap. 1* presents the key principles of pure lipid bilayer fusion, the search for the “*magic lipid mixture*” which forms stalk under low osmotic pressure, and the first study of stalk formation in multibilayers of obtained candidate lipid mixtures in the aqueous environment.

Chap. 2 introduces the design and synthesis of heavy-atom labeled transmembrane β -peptides, the incorporation of such β -peptides into model lipid bilayers, and the x-ray characterizations of peptide conformations in the bilayers.

Chap. 3 presents the novel protein compatible protocol for supported multibilayers, namely the spreading vesicle suspension (sVS) method, which can be used to reconstitute membrane proteins such as SNAREs. The sVS preparation is composed of three stages: (i) the micelle stage, (ii) the vesicle stage and (iii) the multibilayer stage.

Chap. 4 takes advantage of the small-angle x-ray scattering (SAXS) technique and model fitting to investigate proteomicelles and proteoliposomes prepared by the novel sVS method. The influence of preparation methods, lipid compositions (only for vesicles) and SNARE reconstitution on micelle and vesicle structures are carefully evaluated.

Chap. 5 first presents the preliminary grazing-incidence small-angle x-ray scattering (GISAXS) study on supported multibilayers reconstituted with SNAREs at only a few hydration conditions, followed by systematic in-house x-ray reflectivity and GISAXS characterizations performed at a large number of hydration conditions.

Chap. 6 summarizes the results within the framework of this thesis and discusses future improvements of the newly established model systems and methods in this work.

1 Stalk formation in pure lipid bilayers in aqueous solutions

Part of this chapter is based on the published manuscript: Z. Khattari, S. Köhler, Y. Xu, S. Äffner and T. Salditt. Stalk formation as a function of lipid composition studied by x-ray reflectivity. BBA-Biomembranes (2015) [25].

The goal of this work is to achieve stalk formation in pure lipid multibilayers in aqueous solution. However, due to the lack of sufficient external energy to overcome the energy barrier between the lamellar phase and the rhombohedral (stalk) phase, pure lipid bilayers do not spontaneously form stalk structures in aqueous solutions. It is well known that water soluble polymers, e.g. polyethylene glycol (PEG) [26], introduces osmotic pressure to aqueous solution, and thus can mediate stalk formation [27] as well as full fusion [28] in pure lipid bilayers. Unfortunately, the osmotic pressure induced by PEG is rather weak [29, 30] compared with the requirements of fusion in supported multibilayers [21, 25]. In this chapter we first introduce basic principles of stalk formation in pure lipid bilayers, followed by the search for a “magic lipid mixture” which forms stalks at low osmotic pressure (high relative humidity), and finally the preliminary attempt to observe stalks in PEG solutions with the resulting “magic lipid mixture”.

1.1 Principles of stalk formation in pure lipid bilayers

Although in *vivo* fusion events are driven by fusion proteins, lipids which form fluid matrices for membrane proteins also have significant impact on fusion events [31]. In *vitro* we can make pure lipid membranes fuse by offering external energy such as heat [32], osmotic pressure [33], electric field [34], *etc.*, so that the effect of lipids on fusion can be separately evaluated. This section introduces the basic principles of stalk formation in pure lipid bilayers under controlled osmotic pressure.

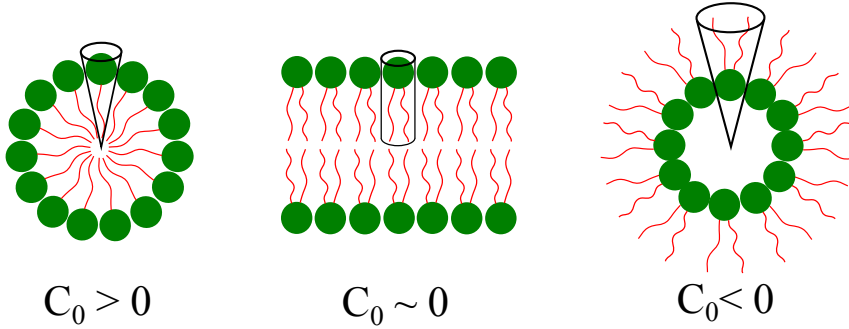


Figure 1.1: Cartoon illustration of the average intrinsic curvature C_0 defined by $C_0 = 2(V/A l - 1)/l$. V is the volume of the entire lipid, l is its full length and A is the cross-section area of the headgroup. In the unrestrained state, $C_0 > 0$ leads to micelles, $C_0 \sim 0$ leads to planar bilayers and $C_0 < 0$ leads to inverted phases [36,37]

1.1.1 The effect of lipid properties on the stalk energy

Chemical properties of the lipids such as their shape, charge, chain length, chain saturation, *etc.*, can largely influence the overall phase behavior of lipid bilayers [35]. Here we briefly introduce a few lipid properties that may significantly lower the stalk energy (the energy barrier between the lamellar phase and the stalk phase).

Lipid shape

A lipid's shape can be quantitatively described by the spontaneous curvature $C_0 = 2(V/A l - 1)/l$ [37,38], where V denotes the volume of the entire lipid, l is its full length and A is the cross-section area of the headgroup. As illustrated by Fig. 1.1, in the unstrained state lipids with positive C_0 tend to form micelles [36], lipids with C_0 close to zero tend to form planar bilayers, and lipids with negative C_0 tend to form inverted structures [39]. For mixed lipid monolayers, the average spontaneous curvature $C_{0,ave}$ is a molar average of C_0 of all lipids within the monolayers [40,41].

KOZLOVSKY and KOZLOV [42] have shown that lipid mixtures with smaller $C_{0,ave}$ (defined as spontaneous splay J_s therein) leads to lower stalk energy. For example, the C_0 of pure 1,2-dioleoyl-*sn*-glycero-3-phosphocholine (DOPC) is -0.1 nm^{-1} and the C_0 of 2-dioleoyl-*sn*-glycero-3-phosphoethanolamine (DOPE) is -0.35 nm^{-1} [40], which result in the stalk energy of $45 k_B T$ for DOPC and -30

$k_B T$ for DOPE [42]. Adding DOPE to DOPC can significantly reduce $C_{0,ave}$ [40], hence lower the stalk energy [42]. Therefore, we will incorporate lipids with lower C_0 such as DOPE, cholesterol (Chol) and 1-2-dioleoyl-*sn*-glycerol (DOG) into the “magic mixture”, aiming at the lowest stalk energy by combining these lipids.

Charges

In nature, charged lipids such as phosphatidylinositol 4,5-bisphosphate (PIP₂) help to mediate synaptic vesicle fusion by coupling with synaptotagmin [43]. In pure lipid systems, charged lipids are also found to promote fusion. For instance, oppositely charged lipids can together promote the fusion process of their host vesicles [44]. Vesicles containing phosphatidylserine (PS), a negatively charged lipid, can fuse with each other in the presence of a few mM Ca²⁺ [45, 46]. Besides the electrostatic interaction between bilayers, another possible reason for the fusion-promoting effect of charged lipids is that the surface charge density can alter the bending modulus k and Gaussian curvature k_G of the host membrane [46, 47], and thus reduce the stalk energy [42]. In this study we test the stalk-promoting effect of PIP₂ together with other lipids, based on the fact that at lower molar concentrations PIP₂ reduces the osmotic pressure needed to form stalks when mixed with DOPC [20].

Alkyl chain saturation

It is widely accepted that saturated lipids, such as sterols and glycosphingolipids, tend to form highly packed gel-phase lipid rafts which float in the membrane and achieve dedicated cellular functions [48]. In contrast, adding one C=C bond into the acyl chain region can dramatically lower the chain ordering and packing. Thus, monounsaturated lipids usually make up the majority of the liquid disordered phase (L_d) at physiological conditions [49]. By applying certain osmotic pressure, such membranes can transform from the L phase to the R (stalk) phase [13, 21].

Although most lipids in cell membranes are either saturated or monounsaturated, abundant polyunsaturated lipids which contain more than one C=C bond in the acyl chain region are found in many tissues [50]. It has been reported that polyunsaturated fatty acids are able to act like “oil” to activate the assembly of syntaxin 3 and SNAP-25, and thus promote synaptic vesicle fusion [51]. In pure lipid systems, similar promoting effect is also observed.

TEAGURE *et al.* have found that in contrast to DOPE, for which certain osmotic pressure is required to form the H_{II} phase, six-fold unsaturated 1-stearoyl-2-docosahexaenoic acid phosphatidylethanolamine (SDPE) can already form the H_{II} phase at zero osmotic pressure. This finding can be explained by the fact that the polyunsaturated chains greatly increase the flexibility of the acyl chains and reduce the bending energy between lamellar and non-lamellar phases [52]. Therefore, we shall evaluate whether 1-stearoyl-2-docosahexaenoic acid phosphocholine (SDPC) and SDPE can effectively reduce the stalk energy in our model system as well, in comparison to their monounsaturated counter-lipids DOPC and DOPE.

1.1.2 Approaches to apply osmotic pressure to lipid bilayers

The vapor method

Osmotic pressure is one of the most common energy source for bilayer phase transitions [53, 54]. In our previous studies, osmotic pressure was mostly applied with aqueous vapor (the vapor method) [19, 20]. To briefly summarize, two N_2 flows, one wet one dry were pumped into a dedicated vapor chamber. By tuning the ratio of the wet and dry flows, the osmotic pressure, i.e. relative humidity (RH), could be precisely regulated on the time scale of a few minutes. The aqueous vapor can also be produced by equilibrating the chamber with aqueous solutions, typically aqueous solutions of salts [55, 56]. This method has high absolute precision but requires equilibrating time up to several hours or even days. Hence it is more often used as a calibration approach [55, 57].

The dispersion method

Another classic approach to apply osmotic pressure to lipid bilayers is to mix water and dry bilayers at desired ratios [58–60]. After full equilibration in a sealed environment, the re-dehydrated bilayers can be assumed to be subject to certain effective osmotic pressure [60].

The PEG method

Similar to salts, water soluble polymers such as polyethylene glycol (PEG) and polyvinylpyrrolidone (PVP) [61] can also apply osmotic pressure to lipid bilayers in an aqueous environment. As stated in the motivation of this chapter,

we intend to take advantage of the osmotic pressure facilitated by PEG [26] to replace the vapor method. In doing so, the sample environment switches from the gas to fluid state and therefore allows for the influence of physiological conditions, such as pH level and ion strength on stalk formation, to be evaluated in model lipid multibilayers [62]. The osmotic pressure resulting from PEG strongly depends on its molar fraction and molecular weight [30]. The investigation of the dependence of osmotic pressure on PEG concentrations will be presented later in this chapter.

1.2 Search for the “magic lipid mixture”

In the last section, we have pre-selected a series of stalk-promoting lipids from literature as well as our previous study, on the basis of lipid properties that can lower the stalk energy. In this section, we will investigate these lipids in a mixed fashion in order to find a “magic mixture” which requires the lowest stalk energy. We continue to use the conventional vapor method to bring in the osmotic pressure so that the stalk energy of various lipid mixtures can be efficiently analyzed and compared. The basic information of x-ray reflectivity measurements in this section is summarized in Appendix A.1.

1.2.1 Materials and methods

Preparation of supported multibilayers by spreading organic solution (sVS)

Eight lipids are investigated in this chapter, which are 1,2-dioleoyl-*sn*-glycero-3-phosphocholine (DOPC), 1,2-dioleoyl-*sn*-glycero-3-phosphoethanolamine (DOPE), cholesterol (Chol), phosphatidylinositol 4,5-bisphosphate (PIP₂), 1-2-dioleoyl-*sn*-glycerol (DOG), docosahexaenoic acid phosphocholine (SDPC), docosahexaenoic acid phosphatidylethanolamine (SDPE) and porcine brain sphingomyelin (SM). Fig. 1.2 shows the structural formulas of these lipids. All lipids were purchased from Avanti Polar Lipids (Alabaster, AL, USA) and used without further purification. Solid-supported multibilayers which contain ~ 1000 lipid bilayers were prepared by spreading organic solution (sVS) [15, 22]. Prior to deposition, all lipids except PIP₂ were dissolved by the 1:1 (*vol/vol*) mixture of chloroform/2,2,2-trifluoroethanol (TFE) at 10 mg/ml lipid concentration. PIP₂ was dissolved by the 20:9:1 (*vol/vol/vol*) mixture of chloroform,

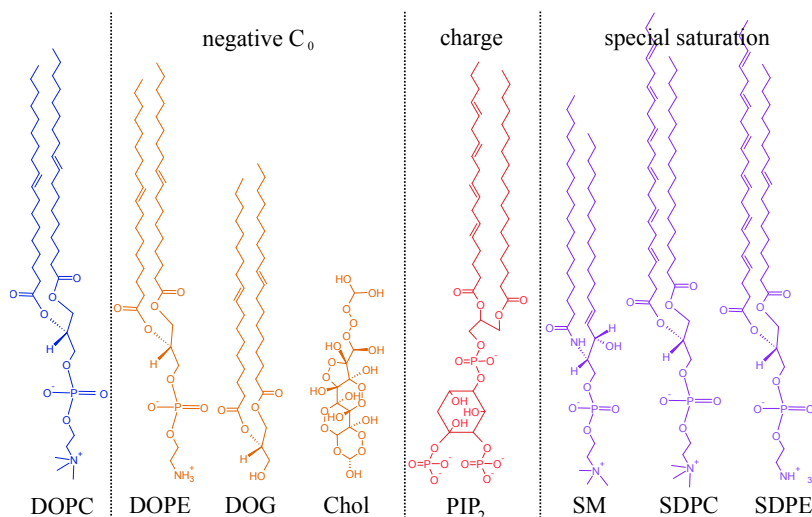


Figure 1.2: Structural formulas of lipids used in this chapter. DOPC is one of the most commonly used bilayer-forming lipid with its spontaneous curvature $C_0 \approx 0$, no net charge and monounsaturated acyl chains. Other lipids are added to DOPC based on their special properties such as negative C_0 , charge and special chain saturation, in order to lower the stalk energy. All structures are drawn with ChemSketch freeware.

methanol and water also at 10 mg/ml lipid concentration. Meanwhile, silicon wafers with $\langle 100 \rangle$ orientation (Silchem, Freiberg, Germany) were first polished, cut to $15 \times 25 \text{ mm}^2$ pieces and cleaned by ultrasonic bath with ultrapure water and methanol iteratively for $5 \times 15 \text{ m}$ in total. The resulting Si wafers were then surface treated in a plasma cleaner (Harrick PDC-002) for 5 min in order to fabricate hydrophilic SiO_2 layers on top of the wafers. $200 \mu\text{l}$ lipid organic solution containing the desired lipid mixture was gently pipetted onto each wafer. After $\sim 2 \text{ h}$ of in-air evaporation, the bulk solvent evaporated while a small amount remained inside. Hence samples were transferred into vacuum oven and stayed overnight to yield dry lipid multibilayers. For highly complex multibilayers which might contain a large number of defects, a slow annealing process was performed by heating the samples up to $40\sim 50 \text{ }^\circ\text{C}$ in a sealed vapor chamber. In the end, the resulting supported multibilayers were stored in the $4 \text{ }^\circ\text{C}$ refrigerator before measurements.

X-ray reflectivity

X-ray reflectivity experiments were performed with the laboratory x-ray 2-circle

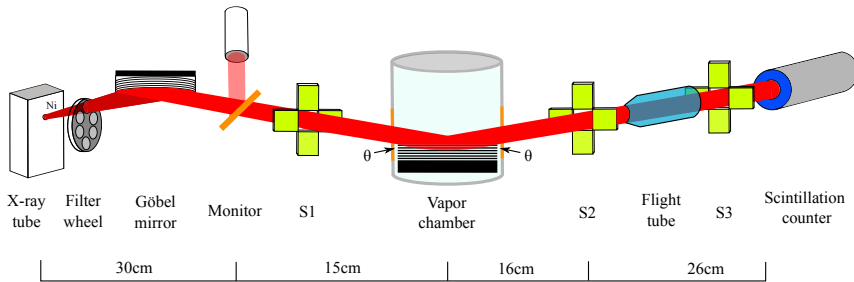


Figure 1.3: Layout of the laboratory diffractometer **Wendi** from the side view. S1, S2 and S3 denote the three sets of slits. The distances between key components are noted under the layout.

diffractometer **Wendi** [19, 63], which is sketched in Fig. 1.3. The long fine focus x-ray tube (Dx-Cu 12×0.4-S GE-Seifert), operating at $U = 35\text{ kV}$ and $I = 40\text{ mA}$, generated a line-focus Cu K_{α} ($\lambda = 1.54\text{ nm}$, $E = 8.048\text{ keV}$) beam at 6° take-off angle. Here "long" refers to the length (12 mm) and "fine" refers to the width (0.4 mm) of the focal spot. A nickel window was mounted at the exit of the tube to attenuate the Cu K_{β} emission. A macro-controlled, motorized filter wheel was mounted and controlled by macros to avoid over-exposure. The thickness and transmission of these filters are summarized in Appendix A.2. The resulting beam was collimated and further monochromated by a multilayer Göbel mirror (FOX 1D CU 12-INF, Xenocs). The beam size at the sample was defined to be $6 \times 1\text{ mm}^2$ by a set of beam-cleaning slits (S1 in Fig. 1.3). After all these optics the characteristic primary intensity was $\sim 2 \times 10^8$ cps with no filter in position. A monitor (GE-Seifert) was mounted between S1 and the sample position, allowing for the inspection of the intensity. Wafers carrying lipid multibilayers were placed in a self-built vapor chamber which was mounted on the 6-axis goniometer stage (Huber) with 3 translational axes (x_s , y_s and z_s) and 3 rotational axes (θ , ϕ and χ). Via iterative scans in these directions the wafer was accurately aligned with the beam. For reflectivity scans, the incident angle θ was coupled with the exit angle Θ so that $\Theta = 2\theta$. Downstream the sample position, the other two sets of slits (S2 and S3 in Fig. 1.3) were mounted to attenuate the scattering in non-specular directions. In the end the specular beam was collected by a fast scintillation counter (Cyberstar, Oxford-Danfysik) in each $\theta/2\theta$ position. For a typical reflectivity scan, the incident angle was scanned from $0-10^{\circ}$ with 0.01° step size and 2 s exposure time per step. Both motor movements and beam collection were controlled by the software SPEC (Certified Scientific Software).

Humidity control

A dry nitrogen flow of constant pressure (5 bar) was equally divided into two branches. One was kept dry while the other was hydrated to RH \sim 100% by passing through pure water. A mass flow controller (Type 657C, MKS Instruments, Germany) mixed the two nitrogen flows at desired ratios and delivered them into the humidity chamber. Both the RH and temperature inside the humidity chamber were measured by a bifunctional sensor (Driesen+Kern GmbH, Germany). Humidity control was integrated into another SPEC console called SPEC-PID via a proportional-integral-derivative (PID) algorithm based macro. In order to reach higher RH, the tubing of the nitrogen flows was heated so that more H₂O could be delivered into the humidity chamber. The highest achievable RH of this setup was \sim 95%.

1.2.2 Data reduction and analysis

The data reduction and analysis process followed our previous studies [19, 20, 64] and has been introduced in great detail in SEBASTIAN ÄFFNER's PhD thesis [65].

Data import

The original reflectivity data produced by the SPEC software was in **.spec** format, which was converted to plain **.txt** format by the **Unspec** software. Since the intensity $I(q_z)$ was recorded at specular conditions, the incident angle θ was converted to perpendicular momentum transfer q_z with $q_z = 4\pi \sin\theta/\lambda$. The resulting $I(q_z) - q_z$ curves were imported into MATLAB (MathWorks Inc.) for further processing.

Background subtraction

The obtained intensity $I(q_z)$ is a superposition of the reflectivity from multiple lipid bilayers as well as the Si substrate. Either offset scans [66] or full q_z range fitting [17, 67] could extract the contribution of the multibilayer from $I(q_z)$. Such a full q_z range fitting was based on the master formula of reflectivity

$$R(q_z) = R_F(q_z) \left| 1/\rho_{12} \int_{-\infty}^{\infty} d\rho(z)/dz e^{iq_z z} dz \right|^2, \quad (1.1)$$

where R_F is the Fresnel reflectivity, ρ_{12} is the electron density between the two

media and $\rho(z)$ is the electron density profile along the normal direction \mathbf{z} . In our setup however, long counting time, low thermal fluctuation, large bilayer numbers, and high membrane orientation together gave rise to typically more than 8 sharp Bragg orders, which clearly separate from the weak scattering of the substrates (Fig. 1.4a). Therefore, only a simple background subtraction was performed to yield form factor modulus $|F_n|$ in the n^{th} Bragg position [65].

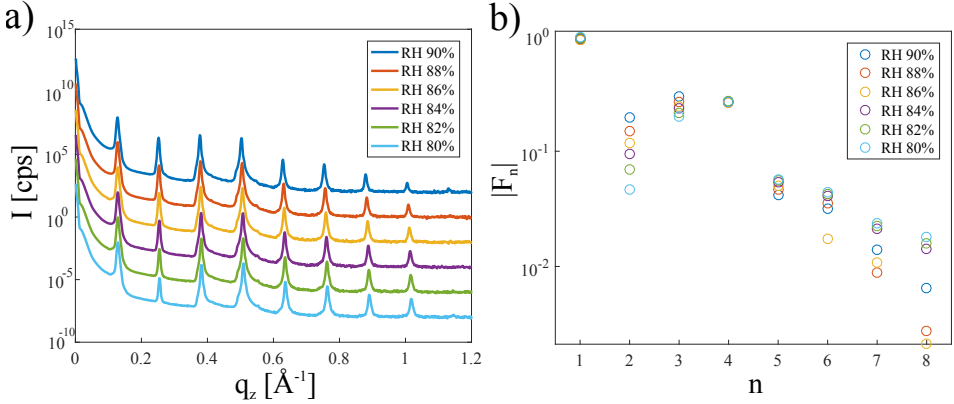


Figure 1.4: (a) Reflectivity curves of pure DOPC multibilayer at RH 90-80%. The intensity is plotted in logarithmic scale and curves are shifted downwards for clarity. (b) Form factor modulus $|F_n|$ in the n^{th} Bragg position derived from the Bragg peak areas in (a).

Intensity correction

Prior to the derivation of form factor $F(q_z)$ from $I(q_z)$, a few corrections were applied to $I(q_z)$ using

$$I_{corr}(q_z) = KC_{abs}C_{pol}C_{Lor}C_{ill}C_{mul}I(q_z), \quad (1.2)$$

which have been introduced in [63, 65]. K denotes the global scaling factor depending on the instrumentation.

C_{abs} denotes the absorption factor resulting from radiation absorption of the membrane, with

$$C_{abs} = \frac{1 - \exp(-2\mu D/\sin\theta)}{2\mu D/\sin\theta}, \quad (1.3)$$

where μ is the absorption coefficient and D is the thickness of the membrane.

C_{pol} is the polarization factor. Unlike synchrotron radiation, an x-ray beam generated by a sealed x-ray tube is not polarized, so that

$$C_{pol} = \frac{1}{2} [1 + \cos^2(2\theta)] . \quad (1.4)$$

C_{Lor} is the Lorentz factor which is a decay factor depending on the experimental geometry and sample morphology. For reflectivity of oriented bilayers,

$$C_{Lor} = (\sin 2\theta)^{-1} \propto q_z^{-1} . \quad (1.5)$$

C_{ill} denotes the illumination factor caused by off-target illumination at small incident angle θ . For $\theta < \arcsin(h/l)$,

$$C_{ill} = h/(l \sin \theta) ; \quad (1.6)$$

while for $\theta \geq \arcsin(h/l)$, $C_{ill} = 1$. Here h and l represent the beam sizes in the vertical and horizontal directions of the sample position.

C_{mul} is the multiplicity factor resulting from a number of non-lamellar indices contributing to the same diffraction order. For the Bragg peaks in reflectivity experiments, $C_{mul} \equiv 1$.

Finally, form factor modulus $|F_n|$ in the n^{th} Bragg position was obtained with $|F_n| = \sqrt{I_{corr}(n)}$, where $I_{corr}(n)$ denotes the area of the n^{th} Bragg peak.

Electron density profile (EDP) reconstruction

The electron density $\rho(z)$ along the membrane normal z can be calculated with F_n derived above [25, 68] with

$$\rho(z) = \sum_n v_n |F_n| \cos(q_n z) , \quad (1.7)$$

where v_n denotes the phase of the n^{th} Bragg order. The sVS method results in highly symmetric bilayers, and thus v_n can only be +1 or -1. The swelling method [13, 33] was then applied in combination with the minus fluid model [69, 70]. The resulting minus-fluid form factor $F^{-1}(q_z)$ is a continuous function of q_z and independent of the RH. The best phase combination was found when

$$\sum_{RH} \sum_n |v_n F_n - F^{-1}(q_n)|^2 = \min . \quad (1.8)$$

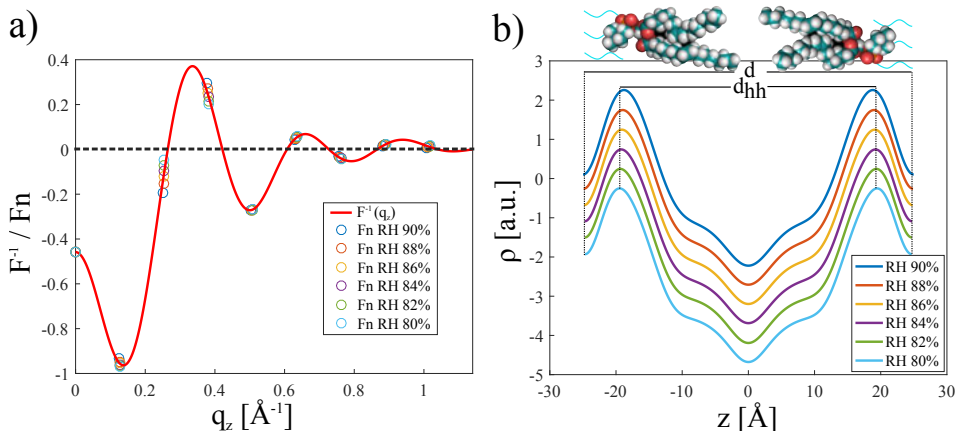


Figure 1.5: (a) Phased form factor $v_n F_n$ and continuous minus-fluid form factor $F^{-1}(q_z)$ as a function of q_z . $v_n F_n$ adopts different values at various RHs while $F^{-1}(q_z)$ is RH independent. The same data set as in Fig 1.4 is used. Here the best phase combination is shown. (b) Electron density profiles reconstructed with the phased form factor $v_n F_n$. The electron densities (EDPs) are in arbitrary units, and shifted for clarity. DOPC models are placed on top to illustrate the origin of the electron density.

Fig. 1.5a plots phased form factor $v_n F_n$ and minus-fluid form factor $F^{-1}(q_z)$ against q_z with the best phase combination. It is clear that in this case $v_n F_n$ matches $F^{-1}(q_z)$ well for all investigated RHs.

Fig. 1.5b shows the corresponding EDPs reconstructed with $v_n F_n$ determined in Fig. 1.5a with the swelling method. The two maxima of the EDP stand for the headgroup region of the bilayer, while the minimum in the middle represents the bilayer mid-plane. The bilayer thickness d_{hh} can be derived from the positions of the two maxima. Consequently, the water layer thickness $d_w = d - d_{hh}$. Both the phase retrieval and EDP reconstruction were performed with the MATLAB script `swelling_lamellar.m` [65].

*The determination of the RH**

In this study, the fusiogenicity (the ability for stalk to form) of a certain lipid mixture is parameterized by the critical relative humidity RH^* , where the L phase transforms into the R phase. Such a transition is usually determined by grazing-incidence small-angle x-ray scattering (GISAXS) technique (Fig. 1.6a) [19, 71], which can undoubtedly reveal the bilayer phases. However, GISAXS experiments take a rather long time especially when measured with in-house in-

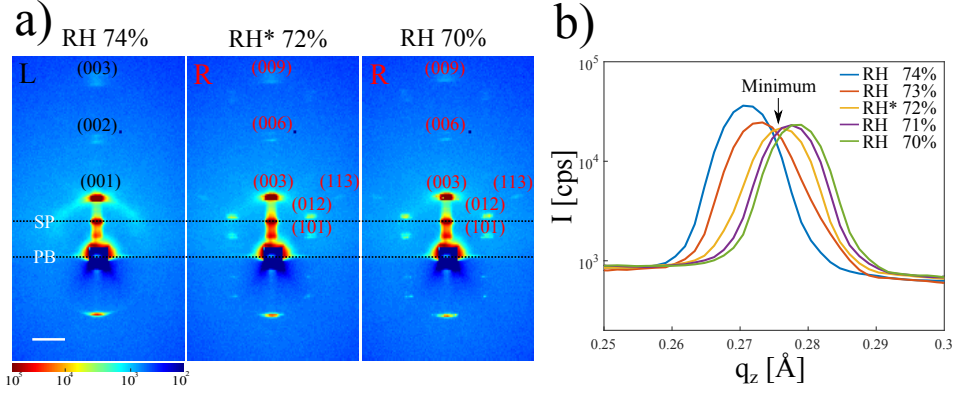


Figure 1.6: (a) GISAXS determination of the critical RH (RH^*) of the $L-R$ transition of DOPC-DOPE 1:1 multibilayer. At RH 72% the typical R phase diffraction pattern is observed indicating $L-R$ phase transition. Images were recorded with the in-house beamline **Rosi** (see Section 5.3.1) at 0.6° incident angle for 1800 s each. Images are shown in logarithmic scale and the white scale bar denotes 20 pixels. Dashed lines denote the positions of the primary beam (PB) and specular peak (SP). The lamellar indices are denoted in black and rhombohedral indices in red. The rectangular shadow in all images results from the beamstop.

(b) Reflectivity determination of the RH^* of the same multibilayer as above. The 2nd Bragg peaks of the reflectivity curves measured at RH 74-70% are shown in logarithmic scale. At RH 72% the minimum intensity is found.

struments (a few hours per diffraction pattern) due to its relatively low flux. In previous reflectivity studies we found that when the L phase transforms into R phase, the intensity of higher order Bragg peaks (2nd, 3rd, 4th, etc.) first decreases and then increases again (Fig. 1.6b). Fig. 1.6b demonstrates that the 2nd Bragg intensity reaches the minimum at the RH^* determined by GISAXS [25]. This way, we developed a more efficient approach to determine the RH^* for $L-R$ phase transition.

Hydration repulsion potential

For bilayers in the equilibrium state, the osmotic pressure Π is balanced by the hydration pressure $P_{hyd}(d_w)$ and van der Waals pressure $P_{vdW}(d_w)$ with

$$\Pi + P_{hyd}(d_w) + P_{vdW}(d_w) = 0. \quad (1.9)$$

Typical d_w values (8-14 Å) [21] in our model system lead to negligible $P_{vdW}(d_w)$ compared with the other terms [65]. We hence obtain

$$\Pi + P_{hyd}(d_w) = 0. \quad (1.10)$$

In the vapor environment, the osmotic pressure Π is a function of the relative humidity RH , with

$$\Pi(RH) = -\frac{k_B T}{v_w} \ln \left(\frac{RH}{100\%} \right), \quad (1.11)$$

where the volume per water molecule $v_w \approx 30 \text{ \AA}^3$ if we assume a constant water density of 1 g/ml. $P_{hyd}(d_w)$ can be empirically written as an exponential decay function with respect to d_w [56, 72, 73]:

$$P_{hyd}(d_w) = P_0 \exp \left(\frac{-d_w}{\lambda_h} \right), \quad (1.12)$$

where λ_h is the characteristic decay length and P_0 is the pre-exponential factor. Combining Eq. 1.10, Eq. 1.11 and Eq. 1.12, we finally arrive at

$$\frac{k_B T}{v_w} \ln \left(\frac{RH}{100\%} \right) = P_0 \exp \left(\frac{-d_w}{\lambda_h} \right). \quad (1.13)$$

With d_w extracted from the EDPs and the experimental RH values, P_0 and λ_h can be fitted to provide an insight into the dehydration behaviors of certain lipid mixtures. Lower P_0 and higher λ_h indicate that it is easier to bring the bilayers into close contact [56].

1.2.3 Binary lipid mixtures

Stalk formation of natural lipids have been extensively studied with their $RH^* \leq 43\%$ [21, 65]. The corresponding Π is too high for PEG aqueous solutions to achieve [30]. We therefore mix different natural lipids in hope of a higher RH^* , i.e. lower Π . One prerequisite of such a mixture is that lipid mixtures must adopt the L phase (planar bilayers) at high hydration conditions. DOPC is one of the most commonly studied bilayer-forming lipids from nature which has a spontaneous curvature C_0 close to zero [38]. Moreover, the RH^* of DOPC is slightly higher than other lipids of its kind [65]. Based on these reasons, we attempt to add one of the stalk-promoting lipids that we have introduced in the last section into DOPC in order to further increase the RH^* . In this section, the phase diagrams and hydration repulsion results of DOPC-DOPE, DOPC-DOG, DOPC-Chol, DOPC-SDPC, DOPC-SDPE and DOPC-PIP₂ will be presented.

DOPC-DOPE

DOPE is regarded as the “gold standard” of non-lamellar lipids [42, 52, 74–76]. It has the same carbon chain as DOPC but a smaller headgroup (sketched in

Fig. 1.7b), hence negative spontaneous curvature. As a result, DOPC and DOPE are often studied in a mixed fashion to evaluate how spontaneous curvature influences bilayer properties [38, 60, 77]. DOPE is known to reduce the necessary temperature [39] and osmotic pressure [72] for the $L-H_{II}$ phase transition, and to cause lipid segregation at higher molar concentrations [60, 77]. However, the R phase, i.e. the phase of the stalk intermediate was not well characterized in early studies of DOPC/DOPE mixtures. Following the pioneering work of Yang and Huang [13, 78], a few years ago our group has carefully investigated the formation of the R phase of pure DOPC, DOPC/DOPE 3:1 and DOPC/DOPE 1:1 [21, 65]. Results show that less osmotic pressure is required to achieve the same dehydration level (d_w) in bilayers with higher DOPE concentration. Besides, neither of the DOPC-DOPE bilayers shows phase separation under all tested conditions.

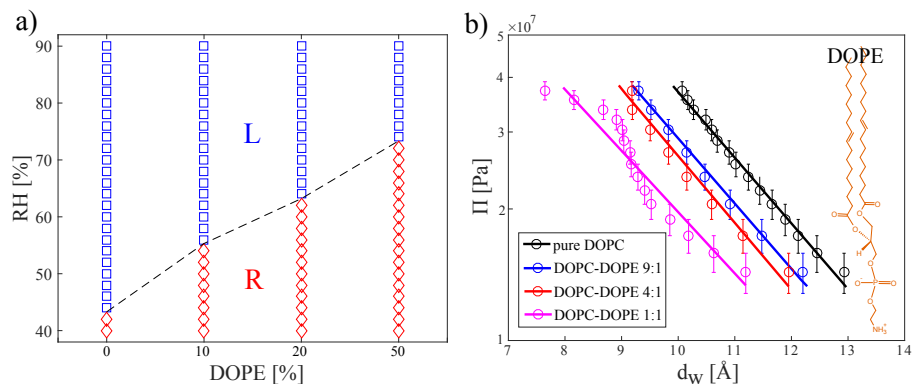


Figure 1.7: (a) The phase diagram of DOPC-DOPE mixtures at RH 90-40%. Each symbol represents one individual scan, with blue squares denoting the L phase and red diamonds denoting the R phase.

(b) Hydration repulsion plots of DOPC-DOPE mixtures in natural logarithmic scale. Only the data of lamellar hydration conditions are used in fitting. Circles denote the experimental data and the solid lines denote the fits, resulting in $P_0 = 1.19, 0.90, 0.89$ and 0.50×10^9 Pa, $\lambda_h = 2.89, 2.91, 2.84$ and 3.09 Å for pure DOPC, DOPC-DOPE 9:1, 4:1 and 1:1 (mol/mol) respectively. The structural formula of DOPE is sketched on the right side of the plot.

In this work, DOPC and DOPE are investigated by x-ray reflectivity at more DOPC/DOPE molar ratios. Fig. 1.7a shows the phase diagram of DOPC-DOPE mixtures at RH 90-40% with the RH^* determined by the reflectivity method. Similar to previous studies, increasing the DOPE concentration consistently leads to a higher RH^* , from 42% to 72%, with no phase separation appearing. No higher DOPE molar fractions are studied to avoid phase separation, which leads to difficult phase identification. Fig. 1.7b shows the hydration repulsion

curves of the DOPC-DOPE mixtures at RH 90-76%. d_w is derived from the EDPs reconstructed from the reflectivity data (not shown). Curves shift consistently towards the left when increasing DOPE fraction, indicating smaller d_w at the same RH. Data is then fitted using Eq. 1.13, resulting in $P_0 = 1.19, 0.90, 0.89$ and 0.50×10^9 Pa, $\lambda_h = 2.89, 2.91, 2.84$ and 3.09 Å for pure DOPC, DOPC-DOPE 9:1, 4:1 and 1:1 (*mol/mol*) respectively. The decrease of P_0 and the increase of λ_h imply that it is easier to dehydrate the bilayers when more DOPE is added. Note that P_0 and λ_h of the same lipid mixture can sometimes vary dramatically between different measurements [21, 25], due to various experimental conditions and fitting ranges.

DOPC-DOG mixtures

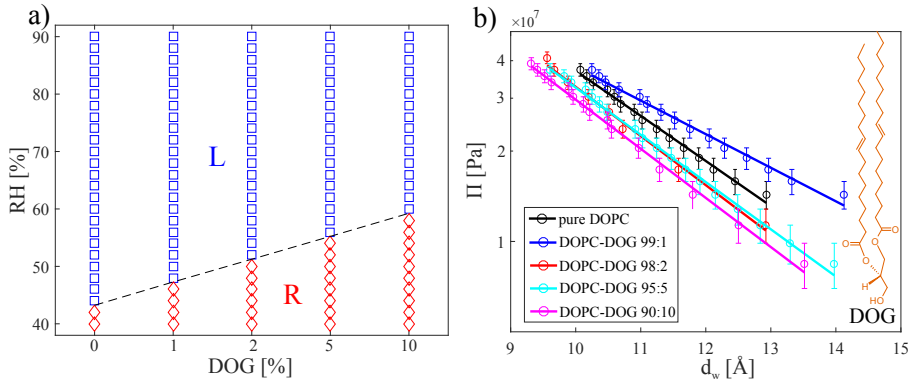


Figure 1.8: (a) The phase diagram of DOPC-DOG mixtures at RH 90-40%. Each symbol represents one individual scan, with blue squares denoting the L phase and red diamonds denoting the R phase.

(b) Hydration repulsion results of DOPC-DOG mixtures plotted in natural logarithmic scale. Only the data of lamellar hydration conditions fitted. Circles denote the experimental data and the solid lines denote the fits, resulting in $P_0 = 1.19, 0.50, 1.42, 1.22$ and 1.28×10^9 Pa, $\lambda_h = 2.89, 3.88, 2.65, 2.76$ and 2.62 Å for pure DOPC, DOPC-DOG 99:1, 98:2, 95:5 and 90:10 (*mol/mol*) respectively. The structural formula of DOG is sketched on the right side of the plot.

As sketched in Fig. 1.8b, DOG has a even smaller headgroup than DOPE and thus a more negative spontaneous curvature. We therefore incorporate DOG into DOPC in the hope of a higher RH* than DOPC-DOPE mixtures. Fig. 1.8a shows the phase diagram of DOPC-DOG mixtures at RH 90-40% with the RH* determined by the reflectivity method. The RH* increases consistently with the molar fraction of DOG, from 42% of pure DOPC to 58% of DOPC-DOG 9:1 (*mol/mol*). DOG leads to larger Δ RH than DOPE at the same molar ratio. For

instance, the RH^* for DOPC-DOG 9:1 is 58% while 56% for DOPC-DOPE 9:1. This result meets our expectation based on lipid shapes. Nonetheless, reflectivity curves of DOPC-DOG 9:1 (data not shown) already show phase separation at lower RHs, which prevents further addition of DOG into DOPC and further increase of the RH^* by this means. Fig. 1.8b shows the hydration repulsion curves of the DOPC-DOG mixtures at RH 90-74%. Curves shift slightly towards the left as DOG amount increases, indicating a mild decrease of d_w at the same RH due to DOG. Fitting results in $P_0 = 1.19, 0.50, 1.42, 1.22$ and 1.28×10^9 Pa, $\lambda_h = 2.89, 3.88, 2.65, 2.76$ and 2.62 Å for pure DOPC, DOPC-DOG 99:1, 98:2, 95:5 and 90:10 (*mol/mol*) respectively. Both parameters of all samples except DOPC-DOG 99:1 fall into a narrow range, indicating similar dehydration behaviors.

DOPC-Chol mixtures

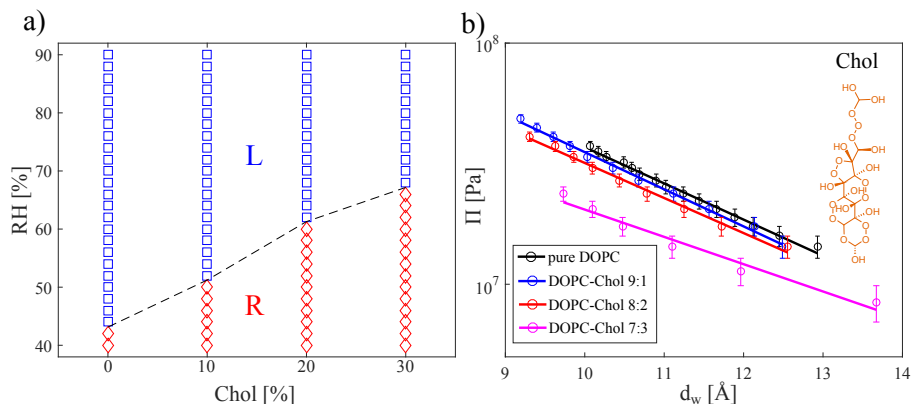


Figure 1.9: (a) The phase diagram of DOPC-Chol mixtures at RH 90-40%. Each symbol represents one individual scan, with blue squares denoting the L phase and red diamonds denoting the R phase. (b) Hydration repulsion results of DOPC-Chol mixtures in natural logarithmic scale. Data kindly provided by Sebastian Äffner. Only lamellar hydration conditions are analyzed (RH 84-94% for DOPC-Chol 7:3 and 90-76% for others). Fitting (circles) yields $P_0 = 1.19, 1.15, 0.99$ and 0.29×10^9 Pa, $\lambda_h = 2.89, 2.76, 2.75,$ and 3.53 Å for pure DOPC, DOPC-Chol 9:1, 8:2 and 7:3 (*mol/mol*) respectively. The structural formula of Chol is sketched on the right side of the plot.

Another natural lipid with negative spontaneous curvature is Chol, whose structural formula is sketched in Fig. 1.9b. Fig. 1.9a shows the phase diagram DOPC-Chol mixtures at RH 90-40% which was previously determined by SEBASTIAN ÄFFNER with the GISAXS method [19]. The RH^* increases almost linearly with 30% Chol bringing the RH^* to 66%. When Chol concentration increases further, the cubic phase and H_{II} phases appear beside the regular L and R phases [19]. Hence it is difficult to further increase the RH^* by adding Chol. Fig. 1.11b shows

the hydration repulsion curves of the DOPC-Chol mixtures at RH 90-76% (94-84% for DOPC-Chol 7:3). Generally the plots shift to the left when more Chol is added, indicating smaller d_w at the same RH due to Chol. The fit results in $P_0 = 1.19, 1.15, 0.99$ and 0.29×10^9 Pa, $\lambda_h = 2.89, 2.76, 2.75,$ and 3.53 Å for pure DOPC, DOPC-Chol 9:1, 8:2 and 7:3 (*mol/mol*) respectively. These results demonstrate that Chol leads to lower P_0 and higher λ_h , i.e. easier dehydration.

DOPC-SDPC and DOPC-SDPE mixtures

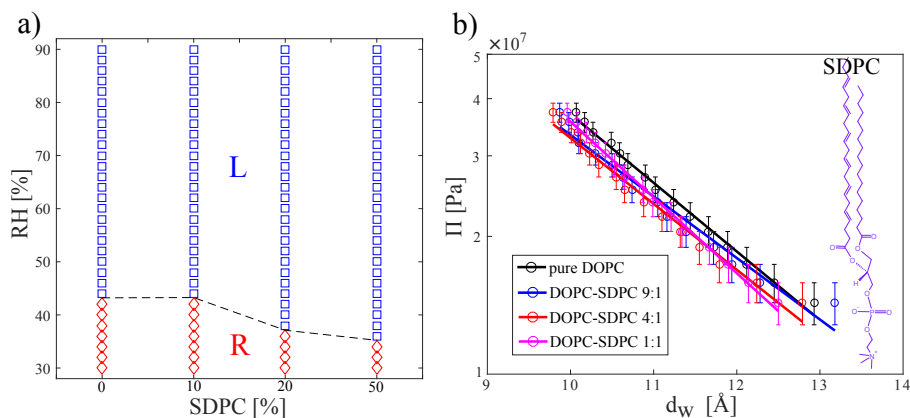


Figure 1.10: (a) The phase diagram of DOPC-SDPC mixtures at RH 90-30%. Each symbol represents one individual scan, with blue squares denoting the L phase and red diamonds denoting the R phase.

(b) Hydration repulsion results of DOPC-SDPC mixtures plotted in natural logarithmic scale. Only the data of lamellar hydration conditions are used in fitting. Circles denote the experimental data and the solid lines denote the fits, resulting in $P_0 = 1.19, 0.73, 0.90$ and 1.61×10^9 Pa, $\lambda_h = 2.89, 3.23, 3.02$ and 2.62 Å for pure DOPC, DOPC-SDPC 9:1, 4:1 and 1:1 (*mol/mol*) respectively. The structural formula of SDPC is sketched on the right side of the plot.

Now we take a look at the lipids with polyunsaturated carbon chains. As sketched in Fig. 1.10b, SDPC has the same phosphatidylcholine headgroup as DOPC but a six-fold unsaturated docosahexaenoic acid carbon chain. Figure 1.10a shows the phase diagram of DOPC-SDPC mixtures at RH 90-30% with the RH* determined by the reflectivity method. Surprisingly the RH* goes down from 42% to 34%, indicating a stalk-inhibiting effect of SDPC in our model system. Fig. 1.10b shows the hydration repulsion curves of the DOPC-SDPC mixtures at RH 90-76%. The plots are very close to each other meaning that the hydration behaviors are not dramatically changed by the addition of SDPC. Fitting results in $P_0 = 1.19, 0.73, 0.90$ and 1.61×10^9 Pa, $\lambda_h = 2.89, 3.23, 3.02$ and

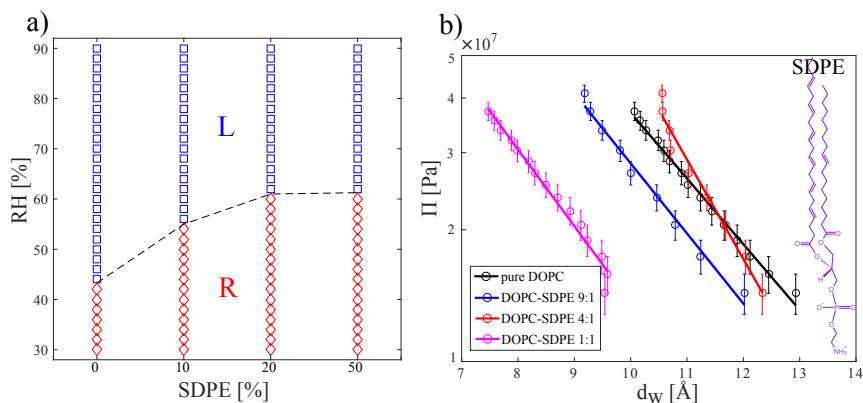


Figure 1.11: (a) The phase diagram of DOPC-SDPE mixtures at RH 90-30%. Each symbol represents one individual scan, with blue squares denoting the L phase and red diamonds denoting the R phase.

(b) Hydration repulsion results of DOPC-SDPE mixtures plotted in natural logarithmic scale. Only the data of lamellar hydration conditions are used in fitting. Circles denote the experimental data and the solid lines denote the fits, resulting in $P_0 = 1.19, 1.13, 9.10$ and 0.77×10^9 Pa, $\lambda_h = 2.89, 2.71, 1.91$ and 2.48 Å for pure DOPC, DOPC-SDPE 9:1, 4:1 and 1:1 (mol/mol) respectively. The structural formula of SDPE is sketched on the right side of the plot.

2.62 Å for pure DOPC, DOPC-SDPC 9:1, 4:1 and 1:1 (mol/mol) respectively.

As sketched in Fig. 1.11b, SDPE has the same phosphatidylethanolamine head-group as DOPE and the same docosahexaenoic acid carbon chain as SDPC. Fig. 1.11a shows the phase diagram of DOPC-SDPE mixtures at RH 90-30% with the RH* determined by the reflectivity method. The RH* increases from 42% to 62% upon the addition of SDPE, indicating a similar stalk-promoting effect as reported in [51, 52]. However, such a promoting effect is much weaker if we compare it with DOPE, which has increased the RH* from 42% to 72% at the same molar ratio. Fig. 1.11b shows the hydration repulsion curves of the DOPC-SDPE mixtures at RH 90-76%. All plots shift towards the left side with the increase of SDPE molar fraction except for DOPC-SDPE 4:1 (mol/mol), indicating smaller d_w at the same RH for bilayers containing more SDPE. Fitting results in $P_0 = 1.19, 1.13, 9.10$ and 0.77×10^9 Pa, $\lambda_h = 2.89, 2.71, 1.91$ and 2.48 Å for pure DOPC, DOPC-SDPE 9:1, 4:1 and 1:1 (mol/mol) respectively. The fitting results of DOPC-SDPE 4:1 seem to be out of order either due to experimental error or a special coupling effect of DOPC and SDPE.

In summary, the addition of SDPC actually lowers the RH*, indicative of an unexpected stalk-inhibiting effect of SDPC when mixed with DOPC; whereas the

addition of SDPE does increase the RH^* but probably due to the PE headgroup rather than the polyunsaturated acyl chain, because the ΔRH^* resulted from SDPE is smaller than from DOPE at equal molar ratios. These results demonstrate that in our model system, in particular when mixed with DOPC, the polyunsaturated chains do not provide desired stalk-promoting effect. Therefore, we no longer take them into consideration in the following study.

DOPC-PIP₂ mixtures

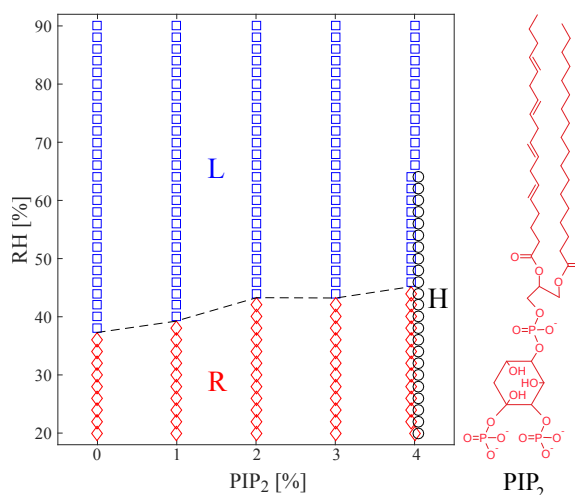


Figure 1.12: The phase diagram of DOPC-PIP₂ mixtures at RH 90-10%, redrawn with permission [20]. Results at higher PIP₂ molar concentration are not shown. Each symbol represents one individual scan, with blue squares denoting the L phase, red diamonds denoting the R phase and black circles denoting the H_{II} phase. The structural formula of PIP₂ is sketched on the right side of the plot.

As sketched in Fig. 1.12, PIP₂ is a negatively charged lipid which should also be able to reduce the RH^* of DOPC. Previously in our group, GHOSH *et al.* have systematically studied the phase behavior of DOPC-PIP₂ mixtures at low PIP₂ molar concentrations (1-10%) by the GISAXS method [20]. It is found that on the one hand PIP₂ is able to increase the RH^* from 38 to 44% at molar concentrations of 1-4%, and on the other hand it leads to an additional H_{II} phase at molar concentrations $\geq 4\%$ but no further increase of the RH^* .

Conclusion

By incorporating other natural stalk-promoting lipids into DOPC, we find that lipids such as DOPE, DOG, Chol and PIP₂ are able to increase the RH*, whereas the polyunsaturated lipids SDPC and SDPE do not manifest the expected stalk-promoting effect. Among the lipids with significant stalk-promoting effect, DOPE gives rise to the highest Δ RH with 50% DOPE leading to a RH* ~ 72%. Moreover, at investigated molar ratios, DOPC-DOPE mixtures do not show any signs of phase separation. Although compared with RH* = 43% for pure DOPC, RH* = 72% is already a great leap forward, its corresponding osmotic pressure is still difficult for the PEG method [30]. Therefore, we choose DOPC-DOPE 1:1 (*mol/mol*) as the base mixture, and add other stalk-promoting lipids to further raise the RH*. In the next section, we will investigate the RH* and dehydration behaviors of ternary lipid mixtures, aiming at a even higher RH* in the absence of phase separation.

1.2.4 Ternary lipid mixtures

Seeing that binary lipid mixtures are unable to yield a sufficiently high RH*, we now proceed to ternary lipid mixtures. DOPC-DOPE 1:1 (*mol/mol*, hereafter referred to as PC-PE 1:1) is used as the base mixture because it has the highest RH* among all tested binary mixtures that exhibit single phase; other stalk-promoting lipids that we have verified above, namely DOG, Chol and PIP₂, are added in to it. In this section, phase diagrams and hydration repulsion results of PC-PE-DOG, PC-PE-Chol and PC-PE-PIP₂ at various molar concentrations of the third lipid component will be presented. This part of data is published in [25], with the PC-PE-Chol data being re-measured.

PC-PE-DOG

Fig. 1.13a shows the phase diagram of PC-PE-DOG mixtures at RH 93-70%. PC-PE molar ratio is kept at 1:1, and 1, 5 and 10% DOG is added into it. On the one hand similar to DOPC-DOG mixtures, DOG slightly increases the RH*, from 72% to 79%. On the other 10% DOG here results in a phase coexistence throughout the entire measured RH range, in contrast to DOPC-DOG 9:1 where the phase coexistence occurs only at lower RHs (for reflectivity curves see Appendix A.3. This is probably because DOG and DOPE together bring about an extremely negative spontaneous curvature, so that energetically bilayers can not maintain single phase even at high RHs. Fig. 1.13b shows the hydration re-

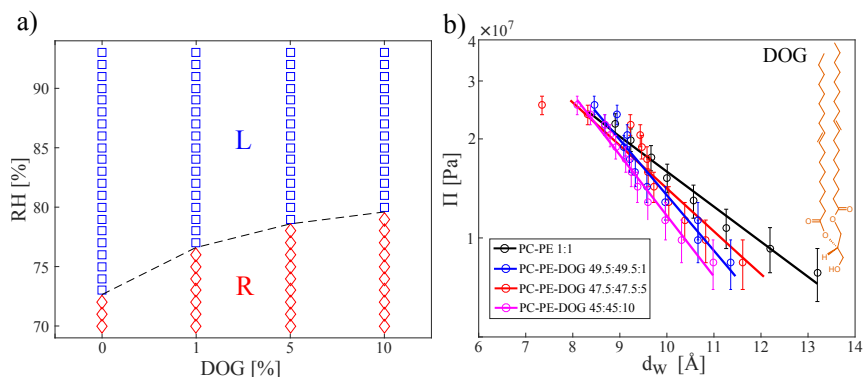


Figure 1.13: (a) The phase diagram of PC-PE-DOG at RH 93-70%. Each symbol represents one individual scan, with blue squares denoting the L phase, red diamonds denoting the R phase. (b) Hydration repulsion results of PC-PE-DOG mixtures at RH 93-83% plotted in natural logarithmic scale. Circles denote the experimental data and the solid lines denote the fits, resulting in $P_0 = 1.99, 0.82, 0.65,$ and 0.28×10^9 Pa, $\lambda_h = 1.95, 2.35, 2.57$ and 3.32 \AA for pure PC-PE 1:1, PC-PE-DOG 49.5:49.5:1, 47.5:47.5:5 and 45:45:10 (molar ratio) respectively. The structural formula of DOG is sketched on the right side of the plot.

pulsion curves of the PC-PE-DOG mixtures at RH 93-83%. All plots stay close to each other but tilts upon the addition of DOG, indicating a easier dehydration resulted from DOG. Fitting yields $P_0 = 1.99, 0.82, 0.65,$ and 0.28×10^9 Pa, $\lambda_h = 1.95, 2.35, 2.57$ and 3.32 \AA for pure PC-PE 1:1, PC-PE-DOG 49.5:49.5:1, 47.5:47.5:5 and 45:45:10 (molar ratio) respectively. P_0 decreases and λ_h increases consistently upon DOG addition.

PC-PE-Chol

In the binary section, Chol brings about the second highest ΔRH^* following DOPE, but leads to the appearance of an additional cubic phase at Chol > 30%. Here we incorporate Chol into PC-PE 1:1 mixture to see if the stalk-promoting effect of PE and Chol is cumulative. Fig. 1.14a shows the phase diagram of PC-PE-Chol mixtures at RH 93-70%. It is exciting to see that Chol brings the RH^* to a much higher level: 5% of Chol is already able to increase the RH^* from 72% to 82%. Subsequently 10% Chol brings the RH^* to 85% and 20% Chol further brings it to 87%, which is the highest RH^* we have ever achieved. However, phases coexistence begins to occur at Chol 20%, as shown by the double Bragg peaks in its reflectivity curves (Appendix A.4). 10% Chol on the other hand, yields a RH^* of 85% which is slightly lower, but mono-phase bilayers at

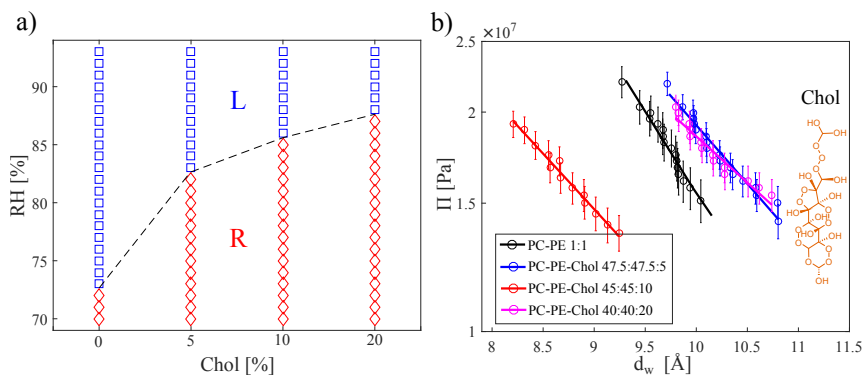


Figure 1.14: (a) The phase diagram of PC-PE-Chol at RH 93-70%. Each symbol represents one individual scan, with blue squares denoting the L phase, red diamonds denoting the R phase. (b) Hydration repulsion results of PC-PE-Chol mixtures at RH 93-83% plotted in natural logarithmic scale. Circles denote the experimental data and the solid lines denote the fits, resulting in $P_0 = 1.99, 0.90, 0.35,$ and 0.45×10^9 Pa, $\lambda_h = 1.95, 2.43, 2.62$ and 2.90 Å for pure PC-PE 1:1, PC-PE-Chol at molar ratios of 49.5:49.5:1, 47.5:47.5:5, 45:45:10 and 40:40:20 respectively. The structural formula of Chol is sketched on the right side of the plot.

all investigated RHs. Fig. 1.14b shows the hydration repulsion curves of the PC-PE-Chol mixtures at RH 93-83%. The hydration repulsion plot of PC-PE-Chol 45:45:10 lies far away from the other three, exhibiting a distinct dehydration behavior. Although PC-PE-Chol 40:40:20 has a higher RH^* , the accompanying cubic phase probably affects its dehydration behavior. Fitting results in $P_0 = 1.99, 0.90, 0.35,$ and 0.45×10^9 Pa, $\lambda_h = 1.95, 2.43, 2.62$ and 2.90 Å for pure PC-PE 1:1, PC-PE-Chol at molar ratios of 49.5:49.5:1, 47.5:47.5:5, 45:45:10 and 40:40:20 respectively. The lowest P_0 (0.35×10^9 Pa) can be found from the PC-PE-Chol 45:45:10 mixture whereas the highest λ_h (2.90 Å) is obtained from the PC-PE-Chol 40:40:20 sample.

PC-PE-PIP₂

When mixed with DOPC, PIP₂ greatly increases the RH^* but introduces an additional H_{II} phase at PIP₂ molar concentrations greater than 5% [20]. In contrast, when mixed with PC-PE 1:1 no clear phase coexistence occurs, even at 30% PIP₂ (for reflectivity curves see Appendix A.5). Figure 1.15a shows the phase diagram of PC-PE-PIP mixtures at mono-phase molar concentrations (0-20%). Interestingly, 5%, 10% and 20% PIP₂ yields the same RH^* (80%), slightly higher than the RH^* of PC-PE 1:1 (72%) but lower than the RH^* of PC-PE-Chol 45:45:10 (85%). It

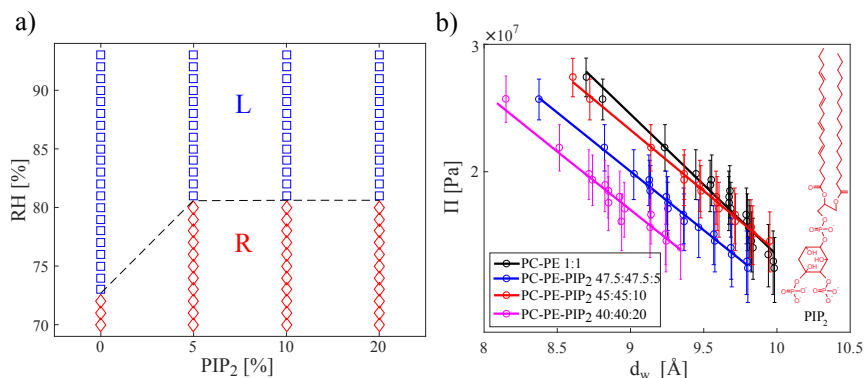


Figure 1.15: (a) The phase diagram of PC-PE-PIP₂ at RH 93-70%. Each symbol represents one individual scan, with blue squares denoting the L phase, red diamonds denoting the R phase. (b) Hydration repulsion results of PC-PE-Chol mixtures at RH 93-83% plotted in natural logarithmic scale. Circles denote the experimental data and the solid lines denote the fits, resulting in $P_0 = 1.99, 0.65, 0.43,$ and 0.34×10^9 Pa, $\lambda_h = 1.95, 2.43, 2.82$ and 2.83 Å for pure PC-PE 1:1, PC-PE-PIP₂ at molar ratios of 49.5:49.5:1, 47.5:47.5:5, 45:45:10 and 40:40:20 respectively. The structural formula of PIP₂ is sketched on the right side of the plot.

seems that the RH* of PC-PE-PIP₂ mixtures quickly reaches saturation at PIP₂ molar concentration as low as 5%. Fig. 1.15b shows the hydration repulsion curves of PC-PE-PIP₂ mixtures. The curves shift towards the left when more PIP₂ is added, indicating smaller d_w at the same RH for bilayers containing more PIP₂. Fitting yields $P_0 = 1.99, 0.65, 0.43,$ and 0.34×10^9 Pa, $\lambda_h = 1.95, 2.43, 2.82$ and 2.83 Å for pure PC-PE 1:1, PC-PE-PIP₂ at molar ratios of 49.5:49.5:1, 47.5:47.5:5, 45:45:10 and 40:40:20 respectively. P_0 decreases while λ_h increases consistently as more PIP₂ is added, meaning that bilayers dehydrate more easily in the presence of PIP₂, which agrees with the DOPC-PIP₂ results.

Summary

In this section, three stalk-promoting lipids, DOG, Chol and PIP₂ are added into PC-PE 1:1, the “best” binary mixture that we have determined in the last section. Results show that the stalk promoting effect is indeed cumulative as indicated by the further increased RH*. Such an increase is significant at lower molar concentrations of the third component, but saturates as soon as higher amount is added. Meanwhile, higher amount of the third component also leads to noticeable phase separation. PC-PE-Chol 40:40:20 for example, yields the highest RH* (87%) among all ternary mixtures, but exhibits strong phase separation. In con-

trast PC-PE-Chol 45:45:10 yields a slightly lower RH^* (85%) but without phase separation. Moreover, $RH^* = 85\%$ of PC-PE-Chol 45:45:10 is still much higher than the RH^* of PC-PE-DOG and PC-PE-PIP₂ mixtures, and is already achievable by the PEG method [30]. Considering that we will introduce PEG and other physiological conditions in the following study, PC-PE-Chol 45:45:10 with clean mono-phase is certainly more favorable.

1.2.5 Quaternary lipid mixtures

In the last section we have determined that PC-PE-Chol 45:45:10 facilitates a high RH^* (85%) as well as clean mono-phase. Additionally, PIP₂ and DOG are also able to increase the RH^* of PC-PE but less effective than Chol. We now add either 1% DOG or 5% PIP₂ to PC-PE-Chol 45:45:10 in hopes of a even higher RH^* without introducing new phases.

Another quaternary mixture studied in this section is PC-PE-Chol-SM 35:30:15:20. It is regarded as the “Nature’s own fusiogenic mixture” [79] because of its similar lipid composition as synaptic vesicle membranes. HAQUE *et al.* [79] have revealed that this mixture is able to promote fusion and reduce vesicle rupture. It is thus interesting to evaluate its stalk-promoting effect in the supported multibilayer system.

PC-PE-Chol-DOG

Fig. 1.16 shows the reflectivity curves of PC-PE-Chol-DOG at molar ratio of 44.5:44.5:10:1 at RH 92-75%. Phase coexistence occurs at almost all investigated RHs. It is an unexpected result since PC-PE-Chol 45:45:10 exhibits clean single phase and here only 1% DOG is added. Moreover, at lower hydration conditions (e.g. RH 75%), less Bragg orders can be observed with some showing 3-fold peaks, indicating a even stronger phase separation and reduced lamellar ordering. Similar to PC-PE-DOG mixtures, DOG’s highly negative spontaneous curvature again seems to be unfavorable among the majority of the lipids and thus leads to phase separation. As a result of the severe phase separation, it difficult to undoubtedly identify the RH^* with the reflectivity determination.

PC-PE-Chol-PIP₂

Fig. 1.17 shows the reflectivity curves of PC-PE-Chol-PIP₂ at molar ratio of 42.5:42.5:10:5 at RH 94-80%. At higher hydration conditions (RH 94-91%), only

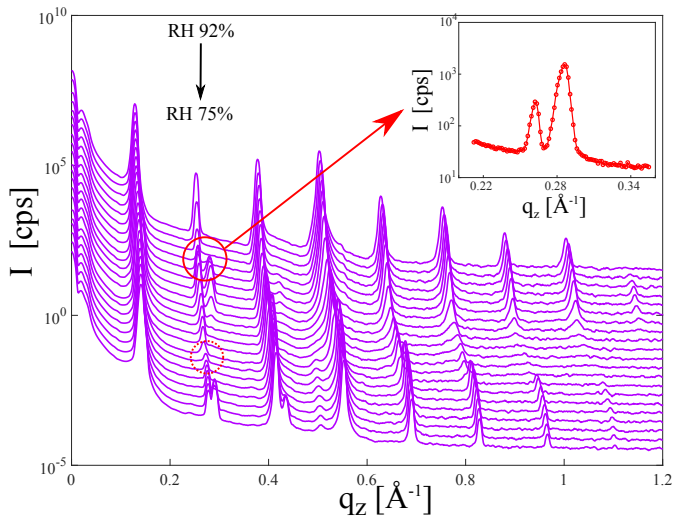


Figure 1.16: Reflectivity curves of PC-PE-Chol-DOG 44.5:44.5:10:1 at RH 92-75% from top to bottom. Data plotted in logarithmic scale and scaled for clarity. Inset: Zoom of the 2nd Bragg peak at RH 87%.

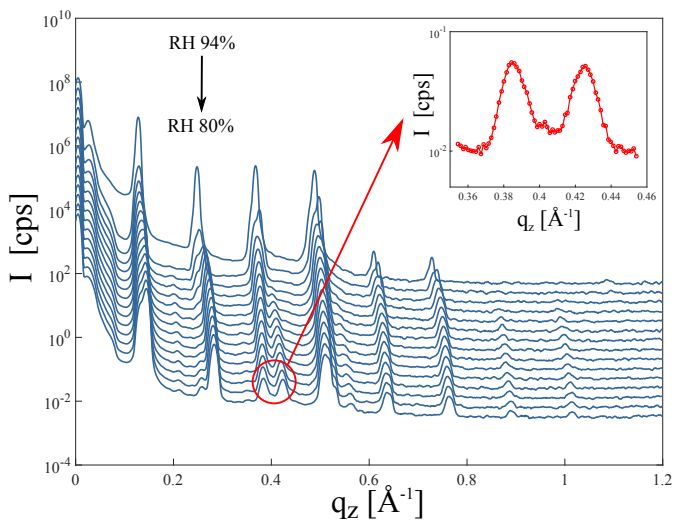


Figure 1.17: Reflectivity curves of PC-PE-Chol-PIP₂ 42.5:42.5:10:5 at RH 94-80% from top to bottom. Data plotted in logarithmic scale and scaled for clarity. Inset: Zoom of the 3rd Bragg peak at RH 87%.

one phase appears; whereas at lower hydration conditions a new phase with smaller bilayer periodicity emerges, which is perhaps the H_{II} phase [20]. This observation is not in line with the results of PC-PE-Chol 45-45-10 and PC-PE-PIP₂ 47.5-47.5-5 where single phase persists. We hence assume that the coexistence of Chol and PIP₂ leads to large packing stress [80], and the membrane reacts to it by forming an additional H_{II} phase. Consequently, we can not undoubtedly identify the RH* of PC-PE-Chol-PIP₂ 42.5:42.5:10:5 with the reflectivity determination.

PC-PE-Chol-SM

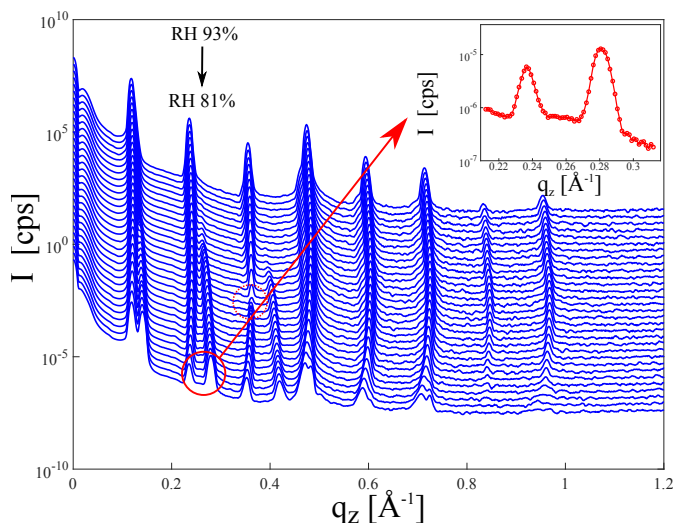


Figure 1.18: Reflectivity curves of PC-PE-Chol-SM 35:30:15:20 at RH 93-81% from top to bottom. Data plotted in logarithmic scale and scaled for clarity. The dashed circle shows the minimum of the 3rd Bragg peaks at RH 89%. Inset: Zoom of the 2nd Bragg peak at RH 83%.

Fig. 1.18 shows the reflectivity curves of the “nature’s own fusigenic mixture”, PC-PE-CH-SM 35:30:15:20 at RH 95-83%. There is only one phase at higher hydration conditions (RH 93-91%); whereas the second phase start to appear at RH \sim 90% and persists until RH 83%. Despite the phase coexistence at lower RHs, we are still able to clearly figure out the intensity minimum of the Bragg peaks, as denoted by the blue circle in Fig. 1.18 at RH 89%. Indeed, the “nature’s own fusigenic mixture” is able to deliver a even higher RH* than solely PC-PE-CH, bu at the cost of phase separation.

Summary

In this section reflectivity scans at various RHs are performed on three quaternary lipid mixtures, namely PC-PE-Chol-DOG 44.5:44.5:10:1, PC-PE-Chol-PIP₂ 42.5:42.5:10:5 and PC-PE-Chol-SM 35:30:15:20. All mixtures show certain degrees of phase separation, either throughout all test RHs or at lower RHs. It certainly disturbs our determination of the RH* and more importantly limits the possible extension of this model system towards physiological conditions. Consequently, the ternary mixture PC-PE-Chol 45:45:10 with a RH* of 85% and clean mono-phase that we have find in the last section is still the best candidate “magic mixture”.

1.3 Investigation of selected mixtures in PEG aqueous solutions

According to the van't Hoff equation, a solution of volume V containing n moles of solute will have an osmotic pressure $\Pi = nRT/V$, where R is the gas constant and T is the temperature [81]. Polymers such as low-molecular-weight PEG are highly soluble in H₂O and thus can be used as a stresser to bring osmotic pressure into aqueous solutions [26, 82]. Moreover, PEG has also been widely used to achieve membrane phase transition [83] as well as membrane fusion [62, 84]. In this section we use PEG-400 instead of the previously used aqueous vapor to apply the osmotic pressure and to promote L - R phase transition.

1.3.1 Osmotic pressure induced by PEG

First of all the effective RH of PEG-400 at various mass concentrations was measured and then converted to Π with

$$\Pi(RH) = -\frac{k_B T}{v_w} \ln\left(\frac{RH}{100\%}\right). \quad (1.14)$$

Results were compared with literature results to check its validity.

Petri dishes containing PEG aqueous solutions at 30, 40, 50, 60, 70 and 80% mass concentrations were placed in the same vapor chamber as in the vapor method. The chamber was entirely sealed so that an equilibrium state could be slowly reached at room temperature. For lower PEG concentrations (30, 40 and 50 wt%) ~ 24 h was needed for the equilibrium state, while for higher PEG

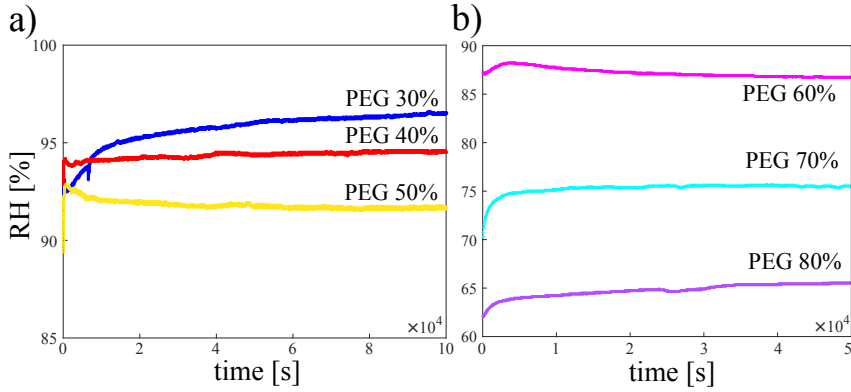


Figure 1.19: RH-time plots of PEG-400 at (a) 30, 40 and 50 wt%, (b) 60, 70 and 80 wt%. The RHs were detected simultaneously by three sensors (Driesen+Kern, Germany).

concentrations (60, 70 and 80 wt%) \sim 12 h was needed. Three humidity sensors (Driesen+Kern GmbH, Germany) were installed in parallel to yield more accurate RH results. Fig. 1.19a shows the RH-time plots of lower PEG concentrations, resulting in equilibrium RHs of 97.51%, 94.45% and 91.52% for PEG 30, 40 and 50 wt% respectively. Fig. 1.19b shows the RH-time plots of higher PEG concentrations, resulting in equilibrium RHs of 86.36%, 75.87% and 66.25% for PEG 60, 70 and 80 wt% respectively.

Fig. 1.20 displays in-house experimental data (black) that we have obtained from Fig. 1.19, as well as three sets of literature data [29, 30, 85]. Our data is fitted via a third-degree polynomial, resulting in

$$RH[\%] = -7.95 \cdot 10^{-5} C_{PEG}^3 + 1.95 \cdot 10^{-3} C_{PEG}^2 - 7.42 \cdot 10^{-2} C_{PEG} + 99.99, \quad (1.15)$$

where C_{PEG} is the mass fraction of PEG-400 in %. The RH is converted to Π with Eq. 1.14 and shown by the right Y axis. At lower PEG concentrations, the RH decreases slightly, staying above 90%. When PEG-400 concentration exceeds 50% on the other hand, the RH decreases rapidly: 80 wt% PEG-400 brings about a surprisingly low RH = 66.25%. It can be found that all literature data shows a similar tendency as our own measurements. Furthermore, different measuring techniques yield results with large variation, especially in the non-measured concentration range (> 50 wt%). Our results show median values, which are the closest to RAND's data [85]. We have determined in the last section that the best candidate "magic mixture" PC-PE-Chol 45:45:10 forms clean stalk phase at RH lower than 85%. From fig. 1.20 we can anticipate that the necessary RH

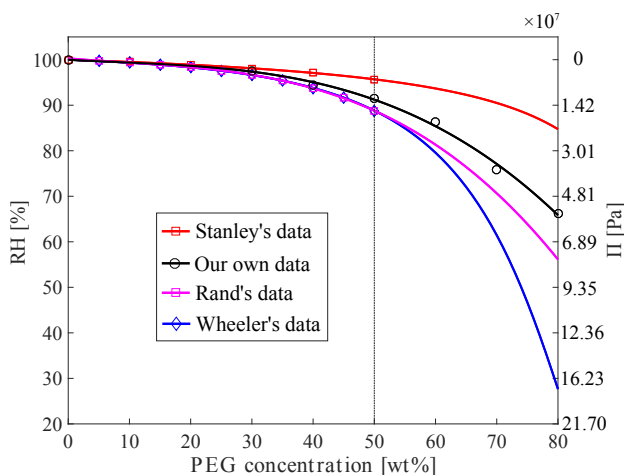


Figure 1.20: The dependence of the RH (the left Y axis) and Π (the right Y axis, derived from RH) on the mass concentration of PEG-400. RHs were measured after equilibrium at room temperature ($\sim 20^\circ\text{C}$). 1 set of in-house data as well as 3 sets of literature data [29, 30, 85] is plotted. Each symbol denotes one individual measurement and the lines are fits of the experimental data.

for stalk formation can be accomplished by PEG-400 aqueous solution of PEG mass concentration $\sim 58\%$.

1.3.2 DOPC in PEG aqueous solutions

Since the bilayer structure and phase behaviors of DOPC is well known, we thus use it as the standard sample to yield an insight of the interactions between PEG-400 and lipid bilayers. Additionally, due to its small size, we shall also inspect whether PEG-400 enters the lipid bilayers. Therefore, before we evaluate the candidate “magic mixture”, we first evaluate how DOPC multibilayer responds to various PEG-400 aqueous solutions.

X-ray reflectivity results

X-ray reflectivity experiments were performed with the commercially available D8 Advance x-ray diffractometer (Bruker-AXS, Germany). The beam generated by a Mo source at 40 mA and 40 kV first passed through a $65\ \mu\text{m}$ thick Zr filter to remove the $K\beta$ emission. The resulting Mo $K\alpha$ beam had a much higher energy ($E = 17.48\ \text{keV}$, $\lambda = 0.071\ \text{nm}$) compared with Cu $K\alpha$ ($E = 8.02\ \text{keV}$, $\lambda = 1.54\ \text{nm}$)

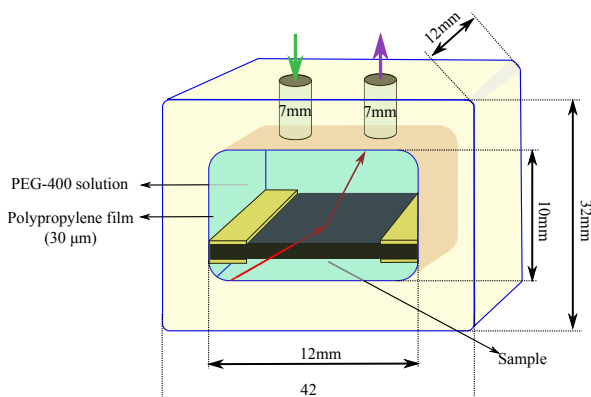


Figure 1.21: Sketch of the self-built fluid chamber [86] designed for x-ray characterizations of lipid multibilayers in solutions. The chamber interior is sealed by two polypropylene films ($30\ \mu\text{m}$) on both sides. The inlet and outlet in the upper part of the chamber can be used for dynamic flow, while in this work they are kept sealed to achieve equilibrated osmotic pressure.

that we used in the vapor method. Thus it could penetrate the aqueous solution with much less absorption. After being collimated by a Göbel mirror the beam was further defined by a set of horizontally wide open slits with $65\ \mu\text{m}$ slit size in the vertical direction. The beam then entered the self-built fluid chamber (Fig. 1.21), where the Si wafer carrying the multibilayer was mounted in the wafer slot on the bottom of the inner chamber [86]. After passing through another set of slits, the exit beam was finally detected by a scintillation counter. Scans were recorded from $\theta = 0$ to 2.5° at intervals of 0.001° for 2 s per step.

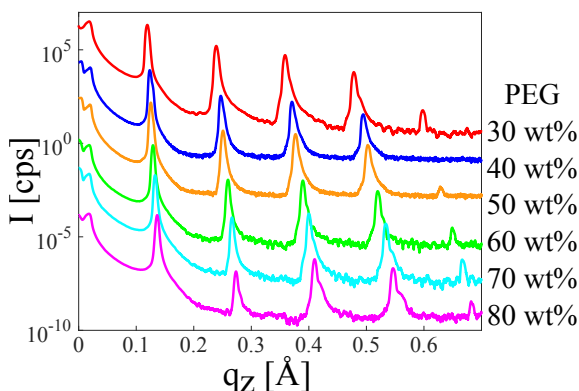


Figure 1.22: Reflectivity curves of DOPC in PEG-400 aqueous solutions at several PEG mass fractions. Curves are plotted in logarithmic scale and shifted downwards for clarity.

Fig. 1.22 shows the reflectivity curves of DOPC in PEG-400 aqueous solutions of PEG mass fractions of 30, 40, 50, 60, 70 and 80 wt%. The curves exhibit relatively high experimental errors compared with the reflectivity curves measured in vapor chamber, as indicated by the rough baseline. For almost all PEG concentrations 5 sharp Bragg peaks can be clearly observed. When PEG concentration increases, the Bragg peaks shift towards lower q_z due to the osmotic pressure induced by PEG.

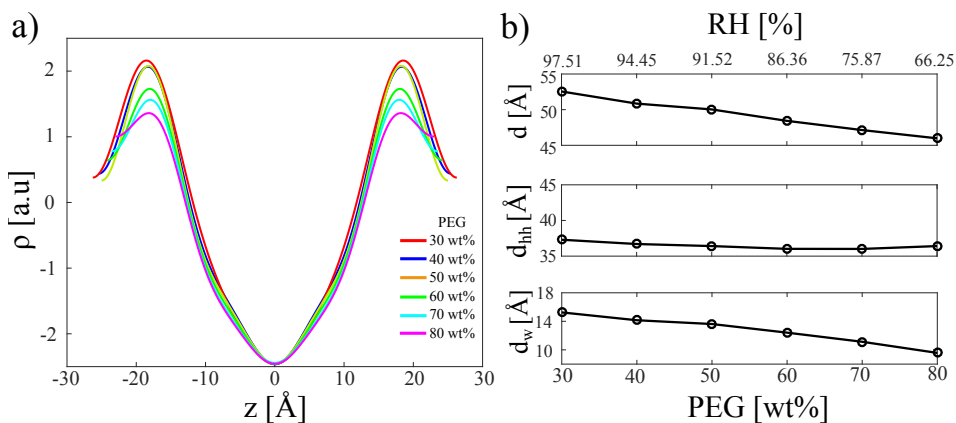


Figure 1.23: (a) EDPs reconstructed with the reflectivity curves in Fig. 1.22, using the phase combination of $-1, +1, -1, +1, -1$. Curves are normalized by the electron density of the methyl dip. (b) Bilayer parameters derived from the EDPs and a function of PEG mass fraction (the lower X-axis). PEG mass fraction is converted to the RH and denoted in the higher X-axis. Standard deviations are too small to be shown.

Fig. 1.23a shows the EDPs reconstructed with the reflectivity curves above, using the phase combination of $-1, +1, -1, +1, -1$. Firstly, all EDPs display the typical cross-bilayer lineshape, implying no significant PEG-400 penetration into the bilayers. Secondly, the electron densities between the water layer and the headgroup region tend to smear out when more PEG is added. This might originate from the PEG molecules that enter the water layer, lead to a higher electron density of the water layer. Lastly, the EDPs of the acyl chains largely overlap with each other, demonstrating an unaltered cross-bilayer structure in the presence of PEG-400, which again proves that no PEG penetrates the bilayers.

Fig. 1.23b shows the bilayer parameters extracted from the EDPs on the left, including the bilayer periodicity d , bilayer thickness d_{hh} and water layer thickness d_w . PEG-400 drastically reduces both d and d_w but barely changes d_{hh} , which is analogous to bilayers' reaction to aqueous vapor [25, 65]. This is an

encouraging result because it validates the method of using PEG to induce osmotic pressure and to promote bilayer phase transition in our model system. Furthermore at lower PEG concentrations, both d and d_w values are comparable to literature values under the same dehydration conditions [65,87], whereas at higher PEG concentrations, slightly lower d and d_w are obtained. For example in our measurement $d \approx 46 \text{ \AA}$ at PEG 80 wt% (RH = 66.25%), while $d \approx 49 \text{ \AA}$ in [65, 87] at RH 66%. It is possibly because that there might be a larger error in the estimated osmotic pressure at higher PEG concentrations (see Fig. 1.20), where the osmotic pressure increase rapidly with the PEG concentration.

1.3.3 PC-PE-Chol in PEG aqueous solutions

Having proved that PEG-400 yields desired osmotic pressure without penetrating the lipid bilayers, we now set the candidate “magic mixture”, PC-PE-Chol 45:45:10 into the same series of PEG-400 solutions. Unlike the vapor method where dehydration conditions can be efficiently tuned by software-controlled pumps, in the PEG method one has to manually prepare PEG solutions and mount the samples for each hydration condition. Although automated strategies like continuous pumping can be developed to mix PEG and H₂O with higher efficiency, currently we can not identify the *L-R* phase transition in PEG solutions using the reflectivity determination, as it usually requires a large number of reflectivity curves at various conditions. We therefore turn to the GISAXS method. Considering the high Cu-K α absorption coefficient of PEG solutions, high-energy synchrotron radiation is used.

GISAXS experiments were performed at the undulator beamline ID01 of the European Synchrotron Radiation Facility (ESRF) in Grenoble, France. The photon energy was set to 17.91 keV by the Si $\langle 111 \rangle$ double crystal monochromator. A series of beamline optics yielded a beam size of $160 \times 20 \mu\text{m}^2$ on the sample, which was set in the fluid chamber (Fig. 1.21). A 6-circle sample tower carried the chamber and enabled sample alignment in 3 translational and 3 rotational directions. A 4-unit 2D pixel detector (Medipix TAA22PC) with 516×516 pixels and $55 \mu\text{m} \times 55 \mu\text{m}$ pixel size was mounted 178.59 mm behind the sample position. A rectangular-shape beamstop was attached to the detector to attenuate the primary beam (PB), the specular peaks (SP) and the 1st Bragg peaks (BP). Each exposure was recorded for 10 s using a 200 μm thick Mo attenuator. PEG-400 aqueous solutions of various PEG mass fractions was successively added into the fluid chamber where the multibilayer sat. Preceding exposures, the whole system was let stand for a few minutes to reach equilibrium.

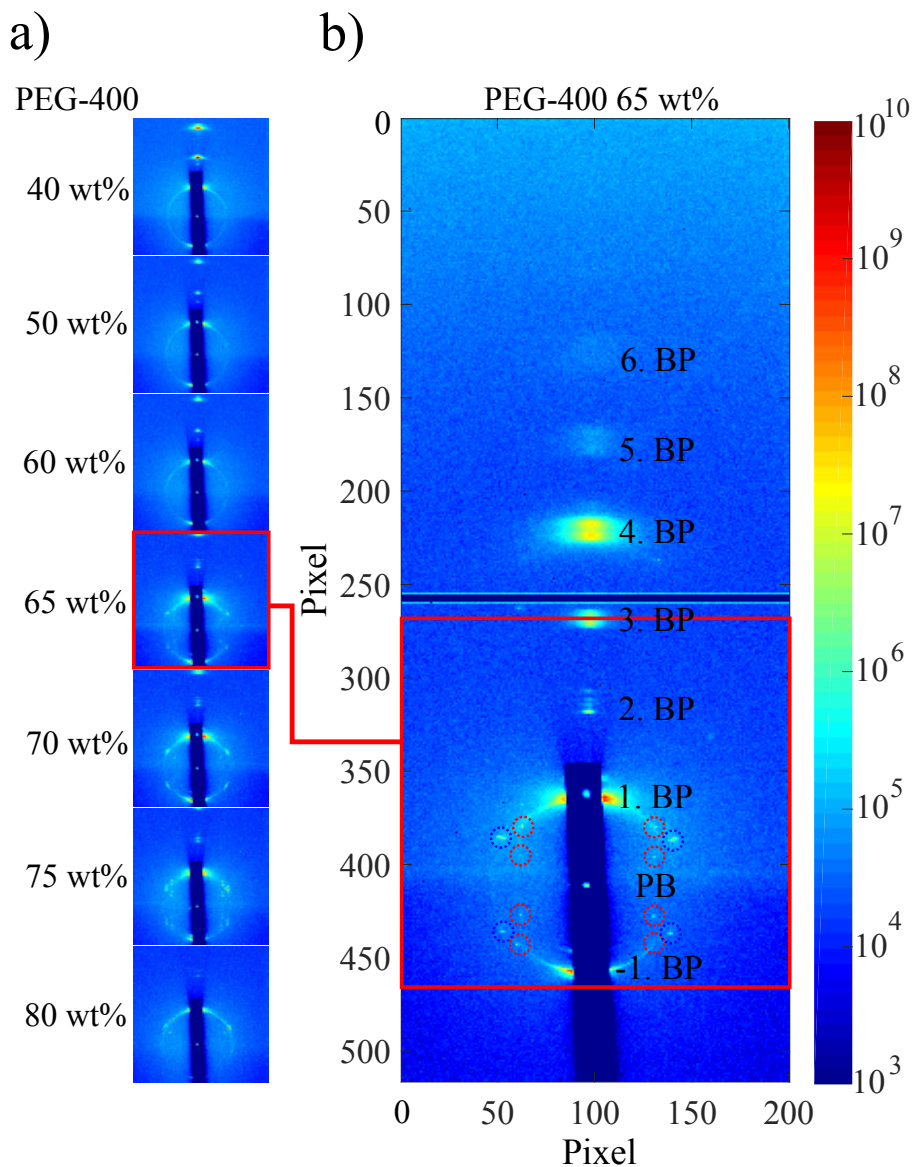


Figure 1.24: (a) GISAXS patterns of PC-PE-Chol 45:45:10 immersed in PEG-400 solutions of various mass fractions, with only ROI being displayed. The shadow results from the beamstop which attenuates the primary beam (PB), specular peaks (SP) and the 1st Bragg peaks (BP). Intensity is plotted in logarithmic scale. (b) Zoom of the GISAXS pattern at PEG 65 wt%. R- H_{11} phase coexistence is observed. The in-plane Bragg peaks are denoted in black while the off-plane peaks are denoted by red (R) and blue (H_{11}) dashed circles.

Fig. 1.24a shows the GISAXS patterns of PC-PE-Chol 45:45:10 immersed in 40-80 wt% PEG-400 aqueous solutions. At lower PEG concentrations (40-60 wt%), only a single L phase shows up. At PEG concentrations higher than 65 wt%, phase coexistence of the R and H_{II} phase can be observed, which is more clearly shown by Fig. 1.24b. The in-plane Bragg peaks (denoted in black) split into two, and meanwhile the characteristic out-plane peaks of both phases appear on both sides of the mid-plane. At even higher PEG concentrations (70-80 wt%) the R - H_{II} phase coexistence persists, while the Bragg peaks become blurry and less visible probably due to radiation damage. Changing the sample after every exposure can eliminate this possibility, but certainly will take more preparation time.

First of all, it is exciting to see the appearance of the R phase in PEG solution, which is the result we have perused in this whole chapter. It opens up a new window for the x-ray characterization of model lipid bilayers. But in the meantime, an unexpected H_{II} phase also appears. Such a phase separation has occurred in the last section, but at 20% Chol rather than at 10%. This is also the reason why we chose PC-PE-Chol 45:45:10 over 40:40:20. This issue of unexpected phase separation is possibly PEG-related, but more investigations have to be performed before we come to a conclusion. Lastly, 65 wt% PEG is in line with our anticipation that the R phase starts to appear at 58 wt% based on the PEG- Π dependence determined in the beginning of this section.

1.4 Summary and outlook

The beginning of this chapter introduces the search of candidate “magic lipid mixtures”. After systematic investigations of various binary, ternary and quaternary lipid mixtures, PC-PE-Chol 45:45:10 mixture was determined to require the lowest osmotic pressure ($RH^* = 85\%$), among mixtures that exhibit clean single-phase at all applied hydration conditions. In the last section of this chapter this candidate mixture was preliminarily investigated in PEG-400 solutions by GISAXS. Excitingly, the desired R phase appears in solutions of PEG concentrations higher than 65 wt%. This finding validates the new model system where stalk structures can form in aqueous solutions in the absence of fusion proteins, and enables upcoming characterization of the influence of physiological conditions such as pH level and ion strength on stalk formation. However, prior to the introduction of these conditions, we first have to optimize the model system by solving the problem of R - H phase coexistence.

2 X-ray studies of transmembrane β -peptides

Part of this chapter is based on the published manuscript: U. Rost¹, Y. Xu¹, T. Salditt and U. Diederichsen. Heavy-Atom Labeled Transmembrane β -Peptides: Synthesis, CD-Spectroscopy, and X-ray Diffraction Studies in Model Lipid Multi-layer. ChemPhysChem (2016). [88].

Integral membrane proteins anchor themselves into the membrane via transmembrane domains (TMDs) [89], which play a critical role in many membrane functions [90, 91] including membrane fusion [92–94]. Most transmembrane proteins are large and complex, and interact strongly with their surrounding lipids in multiple ways [95]. Many model transmembrane peptides [96, 97] have been developed in order to separately investigate the TMDs. For this purpose, β -peptides are well-suited candidates as they are conformationally stable [98], exhibit significant helical propensities in short sequences [99], and offer the possibilities to customize the dipole moment and helical width [100].

This chapter first presents the design and synthesis of heavy-atom labeled 14-helical transmembrane β -peptides, and the preparation of β -peptide/DOPC bilayers. Following previous characterizations of model transmembrane α -peptides [101–103], the resulting β -peptide/DOPC bilayers were investigated by CD spectroscopy, x-ray reflectivity and grazing-incidence small-angle x-ray scattering (GISAXS). Results reveal a successful incorporation of model β -peptides into DOPC bilayers in a slightly tilted transmembrane fashion. Starting from such a success, our collaborators [104] introduced recognition units (β -glutamine) into the current peptide sequence, enabling helix-helix assembly in a sequence-controlled manner. In the future, these results can be further utilized to design and synthesize the TMDs of SNARE analogs, in association with various fusion recognition motifs [105–107] and linkers [108, 109].

¹ These authors contributed equally.

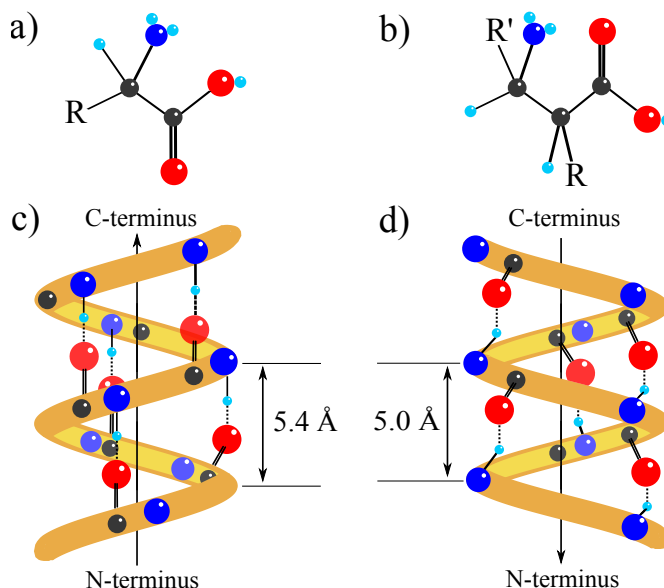


Figure 2.1: 3d illustration of (a) L- α -amino acids, (b) L- β -amino acids, (c) the L- α -helical structure, and (d) the L- β -helical structure. O, N, C and H atoms are denoted by red, blue, gray and cyan spheres, respectively. R and R' denote the side chains. In (c) and (d) side chains, C α , C β and some H are not drawn for clarity. Arrows of the axes point to dipole directions. Structures adapted from [110, 111].

2.1 Fundamentals of β -peptides

α - and β -peptides

Two decades ago, SEEBACH *et al.* [99] and GELLMAN *et al.* [112] showed that synthetic β -peptides which consist of β -amino acids (Fig. 2.1b) were also able to form stable helical structures. Compared with α -amino acids, the additional C β atoms and side chains result in profound differences in the helical architecture [111], as shown by Fig. 2.1c and 2.1d. One turn of α -helices consists of ~ 3.6 residues with its pitch $p \approx 5.4$ Å. In contrast one turn of β -helices consists of ~ 3 residues with its pitch $p \approx 5$ Å [110].

Advantages of using β -peptides as TMDs

The helical structures of β -peptides result in several advantages over α -

peptides in TMD design, synthesis and characterization [88]: (i) β -peptides are more stable against both solvents [113] and enzymes [114]. Thus their helical structures are presumably well preserved in most experimental conditions. (ii) Less amino acids are required for stable β -helices. CD results show that at least 14-15 amino acids are needed to facilitate significant α -helix propensity, whereas as few as 6 residues can already form stable β -peptides [99, 110]. Shorter TMDs can thus be synthesized to better evaluate how TMD length affects TMD behaviors. (iii) The helical width and the helical dipole moment of β -peptides can be varied [97, 99]. In other words, β -peptides can be tailored with higher degree of freedom compared to α -peptides, allowing for a larger variety of resulting TMD structures.

Different types of β -peptides

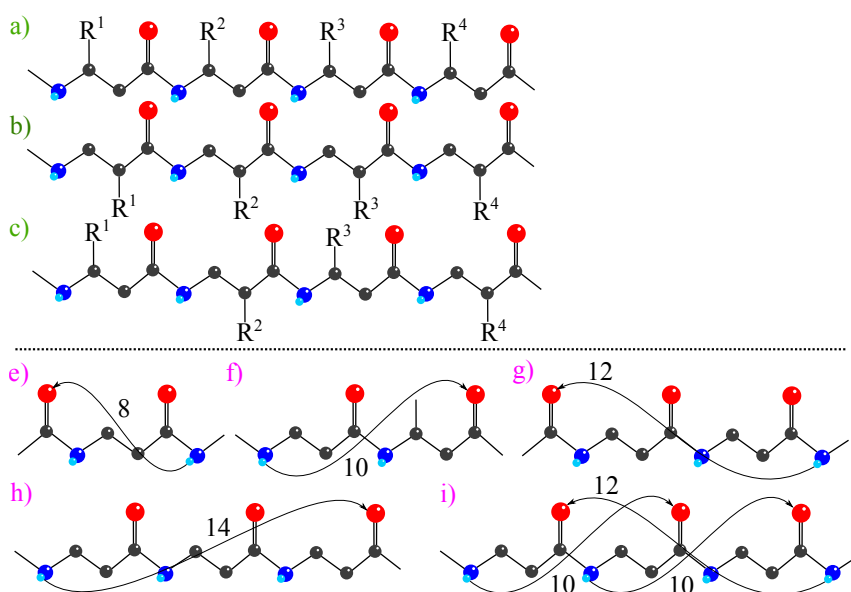


Figure 2.2: Upper: Major $C\alpha/C\beta$ substitution patterns of β -peptides, including (a) β^2 , (b) β^3 and (c) β^2/β^3 [110]. O, N, C and H atoms are denoted by red, blue and gray spheres respectively. R^n denotes the side chains.

Lower: Major hydrogen-bonding patterns of β -peptides, including (e) 8- (f) 10- (g) 12- (h) 14- and (i) 10/12-helices. Side chains are not shown for clarity. Adapted from [113].

One of the many approaches to classify β -peptides is by means of $C\alpha/C\beta$ substitution patterns of the amino acids, resulting in β^2 -peptides, β^3 -peptides, β^2/β^3 -peptides, *etc.* [110]. As shown in the upper part of Fig. 2.2, β^2 -peptides are ex-

clusively substituted at $C\alpha$, β^3 -peptides are exclusively substituted at $C\beta$, and β^2/β^3 -peptides are alternatingly substituted at $C\alpha$ and $C\beta$.

Another approach to classify β -peptides is based on the hydrogen-bonding patterns, i.e. the number of the atoms that form the hydrogen-bonded rings [111]. This is also one of the conventional nomenclature in literature [113]. Common hydrogen-bonding patterns of β -peptides include 8-, 10-, 12-, 14-, and 10/12-helices [112, 115, 116], which are illustrated in the lower part of Fig. 2.2. Among them, the 14-helix is the most common hydrogen-bonding pattern for β^2 - and β^3 -peptides [117]. Its side chain of every third amino acid (i and $i+3$) aligns on the same side of the helix [97], which enables stronger medium-range interactions (i and $i+3$ association), hence the helix is more stable [113].

2.2 Sample preparation

In this section, we first introduce the design and synthesis of two families of 3^{14} transmembrane β -peptides. Each peptide family consists of three β -peptides with different labeling conditions, i.e. non-labeled, I-labeled in the tail region and I-labeled in the center region (see Fig. 2.4 below). I-labels can give rise to stronger x-ray scattering intensity in labeled moieties and thus reveal peptide conformations in the membrane. The only difference between these two families is that the second contains additional h tryptophan (h Trp) anchors, which are known to locate at the polar/nonpolar interface of phosphatidylcholine bilayers [118], and thus enhance the anchoring effect. After synthesis they were integrated either into DOPC vesicles for CD spectroscopy, or into DOPC multibilayers for x-ray characterizations.

2.2.1 Synthesis of I-labeled β -amino acids

I-labeled β -peptides were obtained by modifying commercially available β -amino acids [119], following previously published protocol for α -peptides [101]. Only one of the two side chains was labeled, yielding building blocks compatible with the following Fmoc-based solid-phase peptide synthesis (SPPS) [120].

Fig. 2.3 shows the synthesis pathway of doubly iodinated Fmoc-protected D- β^3 -amino acid. The starting product Boc-D- β^3 -Asp-OBzl (**1**) was obtained from Boc-I-Asp(OBzl)-OH. **1** was converted to Weinreb amide (**5**) with N-ethylmorpholine, N,O-dimethylhydroxylamine hydrochloride and propylphos-

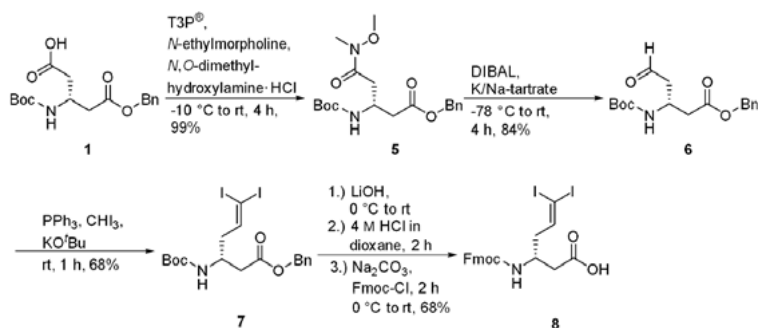


Figure 2.3: Synthesis pathway of Fmoc-D-β³-6,6-diiodoallylhomoglycine (**8**). Boc-D-β³-Asp-OBzl (**1**) was converted to Weinreb amide (**5**), and reduced with DIBAL to yield aldehyde (**6**). Finally deprotection/protection steps were performed under Wittig conditions, yielding tFmoc-D-β³-6,6-diiodoallylhomoglycine (**8**). Adapted from [88].

phonic anhydride [121]. Reducing **5** resulted in DIBAL Aldehyde (**6**) [122], while further treating **6** with triiodomethane under Wittig conditions yielded (*R*)-benzyl 3-*tert*-butoxycarbonylamino-6,6-diiodohex-5-enoate Aldehyde (**7**). Benzyl-deprotection with LiOH and Boc-deprotection with HCl in dioxane (4 M) resulted in readily labeled but unprotected amino acids. Finally with Fmoc-Cl in aqueous sodium carbonate/dioxane solution we obtained Fmoc-D-β³-6,6-diiodoallylhomoglycine (**8**), which was doubly iodinated and Fmoc protected.

2.2.2 Design of transmembrane β-peptides

This section presents the synthesis of the two families of I-labeled transmembrane β-peptides by means of manual microwave-assisted SPPS [119, 123]. Figure 2.4 shows their structural formulas.

These two families of β-peptide share a similar peptide sequence. 19 D-β³-valines (^{*h*}Val) were incorporated in the center of the peptide sequence to span the whole acyl-chain region of lipid bilayers, as ^{*h*}Val is hydrophobic and forms stable 3¹⁴-helical structures [124]. In addition, each side of the peptide was flanked by two D-β³-lysines (^{*h*}Lys) to effectively anchor both ends of transmembrane β-peptides at the water/headgroup interface of the bilayers [125]. We thus obtained the first peptide family (**9**, **10** and **11**) which consisted of only ^{*h*}Lys and ^{*h*}Val. Moreover, it is known that the aromatic indole moieties of D-β³-tryptophan (^{*h*}Trp) tend to reside at the polar/apolar interface of phosphocholine bilayers [126]. In order to further enhance their anchoring effect,

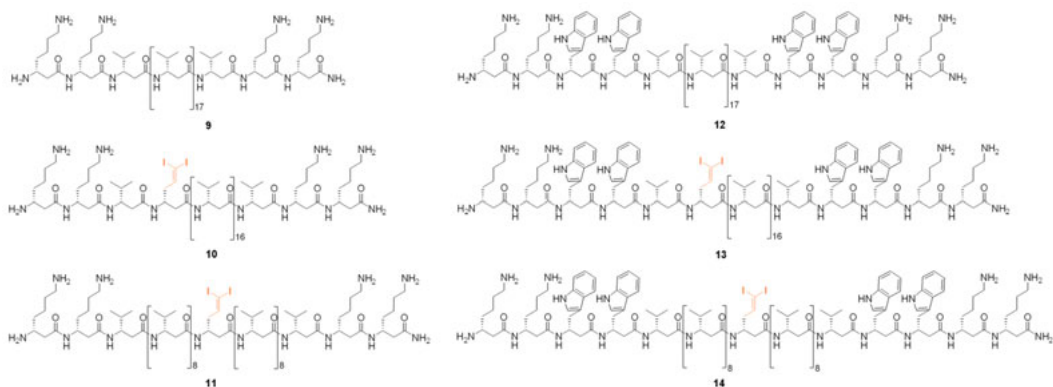


Figure 2.4: Structural formulas of synthesized transmembrane β -peptides. **9-11**: β -peptides do not contain ^hTrp , and **12-14**: β -peptides contain ^hTrp . **9** and **12** are non-labeled, **10** and **13** are labeled at the tail, while **11** and **14** are labeled in the center. I-labels are denoted in orange. Adapted from [88].

β^3 -tryptophans were inserted into the existing peptide sequences, yielding the second peptide family (**12**, **13** and **14**) which consisted of ^hLys , ^hTrp and ^hVal .

Within each peptide family, three labeling strategies were employed: **9** and **12** were not labeled to serve as control peptides. **10** and **13** were labeled in the tail region, whereas **11** and **14** were labeled in the center region. As a result, each peptide family consisted of 3 peptides with different I-labeling conditions. With x-ray reflectivity we will be able to reveal the positions of the labeled moieties in the z direction with respect to the bilayers, and thus determine peptide conformations [101].

2.2.3 Peptide incorporation into model bilayers

The resulting transmembrane β -peptides were incorporated into large unilamellar vesicles (LUVs) for CD-spectroscopy and into supported multibilayers for x-ray reflectivity and GISAXS characterizations. Pure DOPC was used as the lipid component for both model bilayers.

Peptide incorporation into LUVs

β -peptide/DOPC LUVs were prepared by combined vortex and extrusion [127]. First the synthesized transmembrane β -peptides were dissolved by MeOH,

whereas DOPC was dissolved by chloroform. Two solutions were mixed to yield a mixed solution of chloroform/MeOH (1:1, *vol/vol*) at peptide/lipid (P/L) molar ratio of 1:20 and β -peptide concentration of 38 mM. A mild nitrogen stream then slowly removed the organic solvents and resulted in dry β -peptide/lipid films, which was re-dissolved by pure tetrafluoroethylene (TFE) to form helical structures [128]. Afterwards, TFE was again removed by the nitrogen stream which resulted in β -peptide/lipid films containing desired helical structures. The films were stored in vacuum at 40 °C for overnight to thoroughly remove solvents. The resulting β -peptide/lipid films were incubated with ultrapure water for 2 h at 25 °C to gain multilamellar vesicles. Subsequently, the multilamellar vesicle suspensions were vortexed (30 s) and incubated (5 min) iteratively for 5 rounds in total. In the end, vesicle suspensions were extruded through a polycarbonate membrane with 100 nm nominal pore size 31 times using an extruder (Avestin Liposfast, Ottawa, Canada) to yield unilamellar vesicles in pure water for CD spectroscopy.

Peptide incorporation into supported multibilayers

Peptides were incorporated into supported DOPC multibilayers by the conventional sVS method [15,22] introduced in Chap. 1. In brief, DOPC and β -peptides were first separately dissolved by 1:1 (*vol/vol*) mixture of chloroform/TFE with lipid concentration of 10 mg/ml. The two solutions were then mixed at P/L ratios of 1:50, 1:20 and 1:10. 200 μ l of each stock solution was pipetted onto pre-cleaned, highly oriented Si wafers (10 \times 15 mm²), and kept still for 2 h so that the lipids self-assembled into bilayer stacks. Subsequently, the wafers carrying mixed multibilayers were transferred into vacuum and stayed for over night to thoroughly remove the organic solvents. In the end, annealing the samples in sealed vapor chamber yielded highly oriented bilayer stacks containing various transmembrane β -peptides. Samples were stored in 4 ° refrigerator prior to x-ray characterizations.

2.3 Sample characterization

In the last section, we prepared two families of transmembrane β -peptides, with the second family containing additional ^hTrp anchors. Each peptide family consists of three peptides with different labeling conditions, namely non-labeled, tail-labeled and center-labeled. The resulting β -peptides were then incorporated into DOPC LUVs and supported DOPC multibilayers, which were

characterized by CD-spectroscopy to inspect whether the β -helical structures can be preserved in the membrane environment, and by x-ray reflectivity and GISAXS to reveal peptide conformations with respect to the bilayers. In this section, experiments and results of these investigations will be presented and discussed.

2.3.1 CD spectroscopy

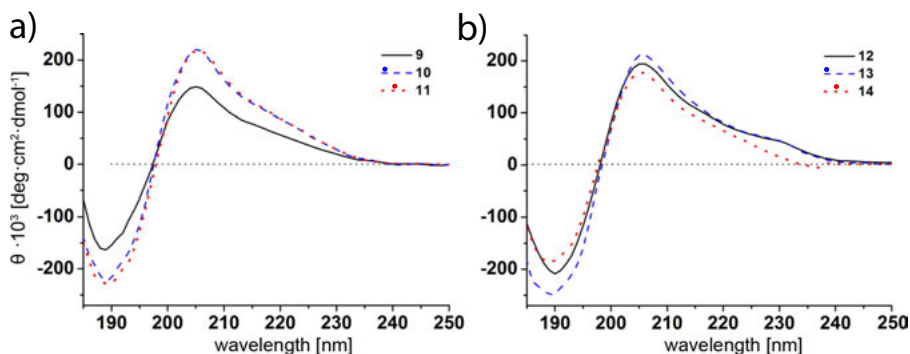


Figure 2.5: Circular dichroism (CD) spectra of (a) transmembrane β -peptides without (9-11) and (b) transmembrane β -peptides with additional h Trp anchors (12-14) in LUVs of 1:20 peptide/DOPC in pure water. I-labels are sketched in the legends. Adapted from [88].

Circular dichroism (CD) spectroscopy is a powerful tool to characterize the helical structures of peptides and proteins [129]. Fig. 2.5a and 2.5b show the CD spectra of transmembrane β -peptides without (9-11) and with (12-14) additional h Trp anchors in LUVs in pure water. The CD spectra of all 6 β -peptides show typical patterns of D-3¹⁴-helices, as indicated by a minimum at 189 nm, a zero crossing at 198 nm, and a maximum at 205 nm. These values are comparable to the literature [116] where a maximum at 200 nm, a zero crossing at 207 nm, and a minimum at 215 nm are found in the CD spectra. Therefore, the β -helical structures were well preserved in the membrane environment, for both the peptides with and without additional h Trp anchors. Moreover, the positions of these signals do not vary within the same peptide family, indicating that I-labels barely affect the helical structures of these transmembrane β -peptides. Lastly, when comparing the CD spectra of 9-11 (Fig. 2.5a) with the spectra of 12-14 (Fig. 2.5b), a weak maximum can be found at 230 nm in the spectra of 12-14. It might be attributed to the additional h Trp anchors in 12-14, as aromatic side chains of h Trp can result in a characteristic CD band at \sim 225 nm [130].

2.3.2 X-ray reflectivity

Instrumentation

X-ray reflectivity experiments of β -peptides/DOPC multibilayers at 0, 1:50, 1:20 and 1:10 P/L ratios were performed with the same self-built in-house x-ray diffractometer **Wendi** as introduced in Chap. 1. Briefly, a sealed x-ray tube (Dx-Cu 12×0.4-S GE-Seifert) operating at $U = 35kV$ and $I = 40mA$ generated a Cu K_{α} ($\lambda = 1.54$ nm, $E = 8.048$ keV) beam, which was monochromated and collimated by a series of x-ray optics, yielding a beam size of 1×5 mm² in the sample position. Samples were mounted in a seal humidity chamber on the 6-axis goniometer stage (Huber). The final specular scattering intensity was detected by a fast scintillation counter (Cyberstar, Oxford-Danfysik). Reflectivity scans were performed at coupled $\theta/2\theta$ with a resolution of $\Delta\theta = 0.01^{\circ}$ and 1 s counting time at each angle. The relative humidity (RH) inside the humidity chamber was kept at $\sim 95\%$. The intensity I was plotted against vertical momentum transfer $q_z = 4\pi \sin\theta/\lambda$, yielding one I - q_z plot for each sample.

X-ray reflectivity curves

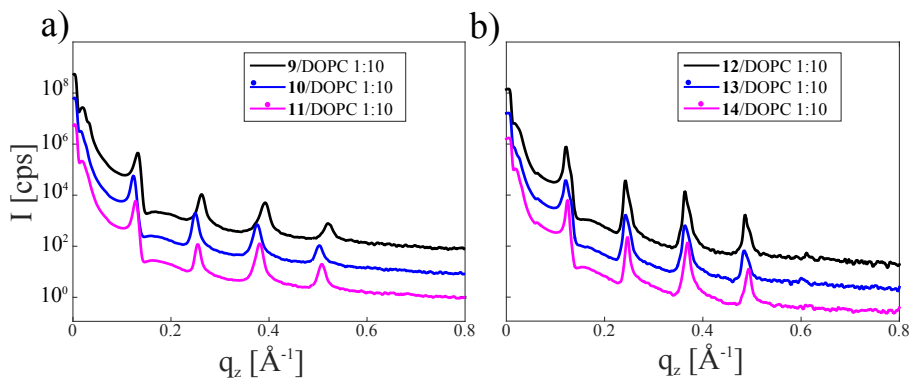


Figure 2.6: The reflectivity curves of β -peptide/DOPC mixed multibilayers (a) without ^hTrp anchors and (b) with ^hTrp anchors. The reflectivity curves are shifted downwards for clarity. The labeling conditions are sketched in the legends.

Fig. 2.6 shows the reflectivity curves of β -peptides/DOPC mixed multibilayers at 1:10 P/L ratio. 4 Bragg peaks occur in the reflectivity curves of multibilayers without additional ^hTrp anchors (Fig. 2.6a), and 5 can be detected from the ones

with h Trp (Fig. 2.6b), with the 5 th peak being hardly visible. This is in sharp contrast to more than eight orders observed for pure DOPC multibilayers (see Fig. 1.4), indicating a drastic decrease of lamellar ordering. This seems to be a common phenomenon for peptide/lipid mixed multibilayers, which has been observed for many other membrane peptides [131, 132]. Moreover, the lineshapes of multibilayers containing β -peptides differ dramatically from the one of pure DOPC multibilayer, indicating a possible change of the structure factor induced by peptide incorporation. The difference in reflectivity curves are thus likely to be associated with changes in the inter-bilayer interaction and possibly strain fields around defects rather than with changes within the bilayers. Otherwise a change of the form factor rather than the structure factor [133] should occur. In this respect, the transmembrane β -peptides in this work completely follow previously observed scenarios.

Reconstructed electron density profiles (EDPs)

EDPs of the β -peptide/lipid bilayers were reconstructed from the intensities in the Bragg positions I_n in a similar way as introduced in Section 1.2.2, except that the best phase combinations were not determined by the swelling method. The reason is that this method requires a series of reflectivity curves for one single sample, while for β -peptide/lipid multibilayers only one hydration condition (RH \approx 95%) was conducted. Thus the phases were manually set to $-1, +1, -1, +1$ for 4-peak curves and to $-1, +1, -1, +1, -1$ for 5-peak curves, on the basis of our previous experience that these phase combinations can result in reasonable EDPs [25, 65]. The electron density $\rho(z)$ was calculated by

$$\rho(z) = \sum_n v_n \sqrt{I_n} \cos(q_n \cdot z) \quad (2.1)$$

where n denotes the number of Bragg orders and v_n denotes the phase of the n^{th} Bragg order.

Figure 2.7 shows the EDPs of β -peptide/DOPC multibilayers at a P/L ratio of 1:10, reconstructed from the reflectivity curves in Fig. 2.6. All resulting EDPs exhibit the typical bilayer lineshape of pure DOPC (see Fig. 1.5), with the two maxima corresponding to lipid headgroups, the minima on both sides corresponding to the water layer and the minimum in the center corresponding to the methyl dip. First of all, it is rather surprising to see well-preserved bilayer structures even at such high peptide concentrations (P/L = 1:10). This indicates that the peptides do not alter the basic structural motif of the DOPC bilayer. However, the peptide insertion results in observable changes of the bilayer structure

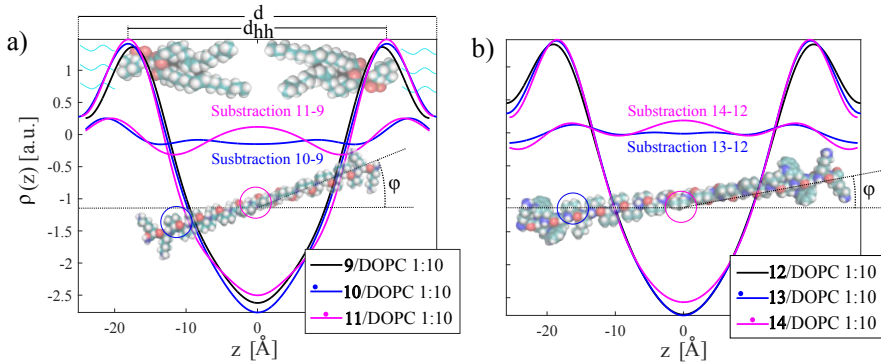


Figure 2.7: The EDPs of 1:10 β -peptide/DOPC multibilayers (a) without h Trp anchors and (b) with h Trp anchors, reconstructed from the reflectivity curves in Fig. 2.6. The electron density distribution is illustrated by drawing 3d sphere models of DOPC underneath (a). The electron contrasts between bilayers containing I-labeled and non-labeled peptides are plotted in the center. Possible peptide orientations are illustrated by placing the molecular drawing underneath both (a) and (b). The labeling conditions are sketched in the legends.

parameters in the electron density and the bilayer thickness, as we discuss further below. These changes might result from both the elastic response of the lipid bilayer to peptide insertion, as well as the direct contribution of the peptides to the electron density.

To disentangle these two effects, we subtract the EDPs of bilayers containing I-labeled peptides by the ones without I-labels. Subtraction curves are plotted in the center of Fig. 2.7. As shown in the legends, **10** and **13** are labeled in the center region, whereas **11** and **14** are labeled in the tail region. Unfortunately, in the absence of a full q -range fit of the reflectivity curve as in [133], the absolute electron densities are not available. Instead, we only obtain relative shape functions, as the Bragg peak intensities (i.e. the Fourier coefficients) are normalized by the intensity of the first Bragg peak, separately for each curve. Nonetheless it is still meaningful to compare the EDPs in arbitrary units, since all the samples were prepared and measured under the same conditions.

For center-labeled peptides (**11** and **14**), a strong contrast is clearly visible in the center region of the EDP. This confirms the full insertion of the TMD, which is not affected by peptide tilting in the bilayers. Hence, the peptides always center themselves in the bilayer mid-plane, as desired. The tail-labeled peptides, **10** and **13** do not exhibit a similar contrast: **10 - 9** provides a small peak at the hydrophobic/hydrophilic interface, which may be associated with the iodine

label in the tail region of **10**. while such a contribution is not visible for **13** - **12**, possibly because it is too widely distributed and hence 'shielded' by the headgroup density. Assuming that the mentioned small peak really represent the I-label, the peptides must adopt a strongly tilted conformation, as illustrated by the peptides models underneath Fig. 2.7. The I-labels exhibit a much clearer labeling effect in the center region than in the tail region, possibly because the original electron density of the headgroup region is much higher than the methyl dip, while I-labels bring the same absolute amount of extra density in both regions. Another reason is that the original electron density the I-labels in the tail region have to be distributed to both bilayer surfaces since only one of the two tails is labeled. In addition, an unexpectedly large contrast around the headgroup region occurs in all subtraction curves, which is closer to the water layer for **11** - **9** and **10** - **9** whereas closer to acyl chains for **14** - **12** and **13** - **12**. This could indicate either an unintended effect of iodine labeling on the host membrane surface, or a fraction of peptides oriented parallel to the bilayer (the S state) [134, 135].

Bilayer parameters derived from the EDPs

Fig. 2.8 presents the water layer thickness d_w and the bilayer thickness d_{hh} of the β -peptide/DOPC mixed multibilayers at P/L ratios of 0, 1:50, 1:20 and 1:10, derived from EDPs in Fig. 2.8. β -peptides, both with and without h Trp anchors show a decrease of d_{hh} with P/L ratios, also known as the membrane thinning effect which has been observed for many other membrane peptides [133, 136]. When the peptides adopt an inserted trans-membrane helical conformation (the I state [135]), this thinning could be induced by a hydrophobic mismatch, forcing both the lipids and peptides to adjust their hydrophobic moieties to achieve a match [137]. With the acyl chain length of DOPC ($d_c \approx 30$ Å, [87]) slightly shorter than the hydrophobic length of the peptides ($d_c \approx 31.17$ Å, 5.0 Å per pitch), a match can be achieved either by peptide tilting or by shrinking. In the latter case, a membrane thickening effect instead of a thinning effect is expected. Therefore it seems that the mismatch is relieved solely by a chain tilt, with an estimated tilt angle of 16°. In this case, one may expect that the tilted β -peptides also induces according acyl chains tilts in its neighborhood. The increase of chains tilts would then explain the thinning effect.

This thinning effect is obviously more significant for **9**, **10** and **11**, compared to **12**, **13** and **14**. In other words, additional h Trp anchors may reduce the ability to minimize mismatch by increased peptide tilting. This tentative explanation is also in line with the vanishing contrast of the tail-labeled peptides, since

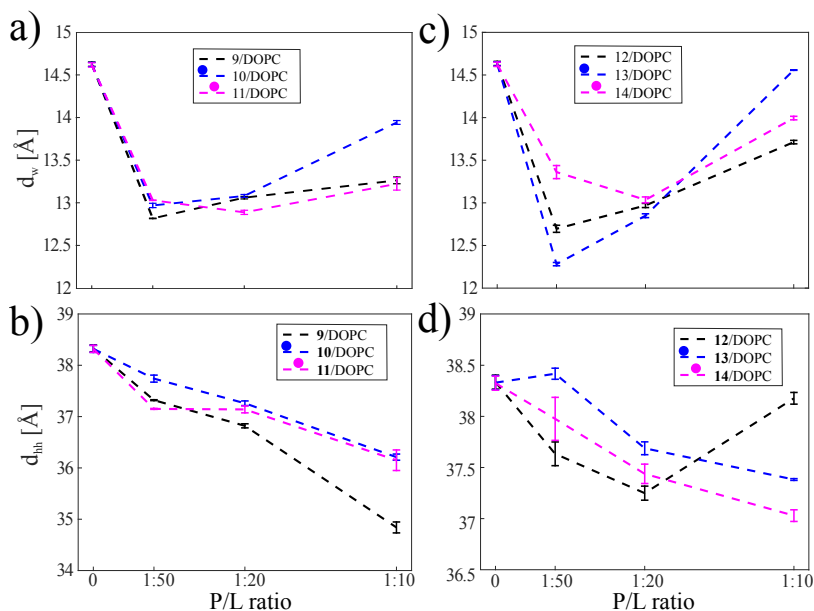


Figure 2.8: (a) the water layer thickness d_w and (b) the bilayer thickness d_{hh} of peptide/DOPC bilayers without ^hTrp anchors (9, 10 and 11) at various P/L ratios; (c) d_w and (d) d_{hh} of peptide/DOPC bilayers with ^hTrp anchors (12, 13 and 14) at various P/L ratios. The error bars denote the standard deviations. The labeling conditions are sketched in the legends.

the distribution function of tilted β -peptides tends to smear out the already small contribution to the total electron density. Eventually, contrast variation by changing the photon energy around the iodine edge (anomalous scattering) could be used in the future to separate this weak signal, following previous experiments on iodine labeled TMD of SARS protein E [138].

Moreover one may be concerned to which extent the labels may change the structural properties of the transmembrane β -peptides. Here we see by comparison of labeled and non-labeled peptides that their d_{hh} and d_w are fairly similar, indicating that the I-label does not cause significant structural changes in the bilayer, in line with the CD results above.

2.3.3 Grazing-incidence small-angle x-ray scattering

Having determined the bilayer structural changes of the β -peptide/DOPC mixed multibilayer with respect to P/L ratios, we now take advantage of grazing-

incidence small-angle x-ray scattering (GISAXS) technique to investigate their chain-chain correlations, as well as the β -helical structures which offer a direct insight of the peptide conformation within lipid bilayers. To this end, multibilayers containing the first peptide family, i.e. β -peptides without ^hTrp anchors were characterized.

Instrumentation and data reduction

Chain-correlation characterization was performed at ID01, ESRF with similar beamline settings as introduced in Chap. 1, except that the sample-detector distance and position of the detector arm were specially chosen to cover the q range of chain correlation peaks as well as helical peaks. Samples were placed in a similar humidity chamber as used in the reflectivity section where the RH was kept at $\sim 95\%$. Each image was recorded with 10 s exposure time. The data reduction followed previous work [64, 139]. The diffraction data was first converted from pixel units to scattering vector components q_z and q_{\parallel} , where

$$q_x = \frac{2\pi}{\lambda} (\cos \alpha_f \cos \psi - \cos \alpha_i) , \quad (2.2)$$

$$q_y = \frac{2\pi}{\lambda} (\cos \alpha_f \sin \psi) , \quad (2.3)$$

$$q_z = \frac{2\pi}{\lambda} (\sin \alpha_f + \sin \alpha_i) , \quad (2.4)$$

$$q_{\parallel} = \sqrt{q_x^2 + q_y^2} , \quad (2.5)$$

as shown in Fig. 2.9a. 1d intensity profiles at different ϕ angles were extracted from the 2d patterns, and then fitted with a Lorentzian above a linear background

$$f(q) = I_0 \frac{\omega^2}{(q - q_0)^2 + \omega^2} + mq + b , \quad (2.6)$$

where ω is the half width maximum, q_0 the peak center, I_0 the maximum of the Lorentzian, m the slope of the linear background, and b the constant offset. The average chain-chain distance a is then obtained from [139]

$$a \simeq \frac{9\pi}{4q_0} - \frac{3\omega}{2q_0^2} , \quad (2.7)$$

and the correlation length ξ of the acyl chains by

$$\xi = \frac{1}{\omega} . \quad (2.8)$$

The experimental and fitted I - q curves of pure DOPC multibilayer is plotted in Fig. 2.9b as an example of the fitting process. In Fig. 2.9c, the resulting parameters I_0 , the chain-chain distance a and chain correlation length ξ are plotted against ϕ , representing the parameters for the fraction of chain segments tilted at ϕ . For a detailed explanation please see [64].

Results and discussion

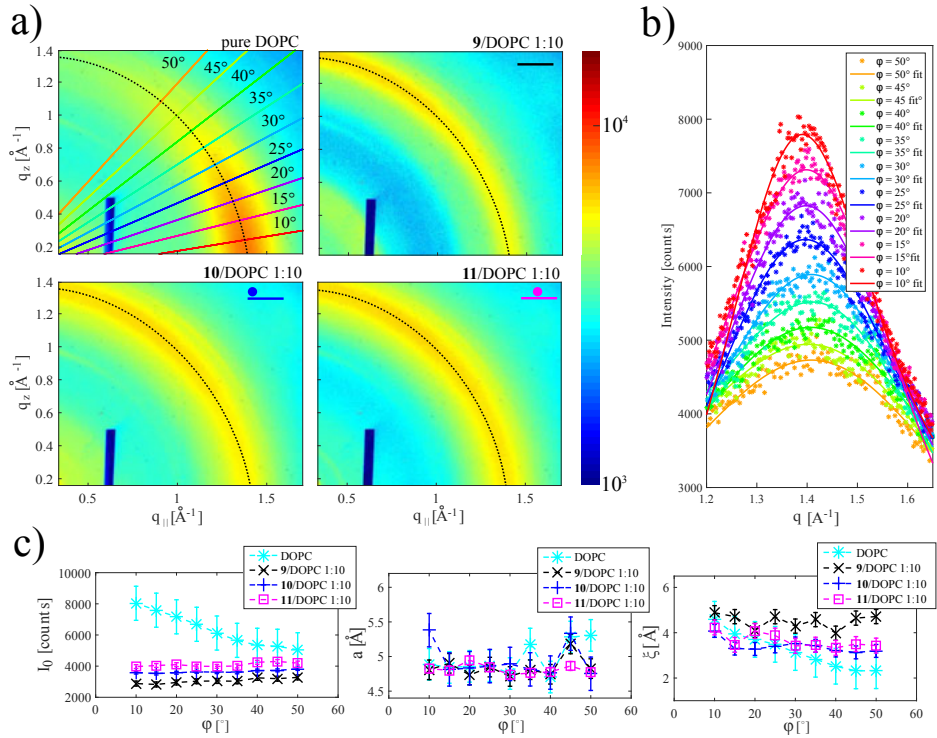


Figure 2.9: (a) GISAXS patterns of DOPC multibilayers containing 10% β -peptide without h Trp (9, 10 and 11) measured in the chain-correlation q regime. The dashed lines denote I_0 . Each colored line represents the intensity profile at the according ϕ angle. All images were recorded with 10 s exposure time. The false color scale corresponds to the logarithmic scattering intensity and the dark blue bar results from the beamstop.

(b) Experimental (stars) and fitted (solid lines) I - q plots of pure DOPC, shown as an example of the fitting process.

(c) Lateral ordering parameters of the multibilayers derived from the fitting. The maximum of the Lorentzian I_0 , chain-chain distance a , correlation length ξ and their standard deviations are plotted as a function of ϕ .

First of all, by visual inspection alone, the 2d patterns suggest that the intensity of chain correlation peaks is dramatically decreased by β -peptide incorporation, indicating a lower lateral ordering which is expected for transmembrane peptides [140] and can thus be considered a further evidence for the transmembrane orientation. Secondly, the intensity decreases with ϕ for DOPC but not in the presence of β -peptides, indicating a broader distribution function for the chain tilt probability due to β -peptide incorporation. This is exactly in line with the interpretation of the observed membrane thinning above. As a word of caution to the previous argument based exclusively on the lipid chain signal, however, we must also consider the fact that the structural peak of the β -helix itself gives rise to a maximum centered around $q_z \sim 1.35 \text{ \AA}^{-1}$, resulting in a helical pitch of $p = 4.7 \text{ \AA}$, which is in the same order of the literature value $p = 5.0 \text{ \AA}$ [110]. For further analysis of helical peaks please see previous work on helical form factors of α -helices [140]. For tilted peptides, however, this signal may also be smeared out on an arc and merge into the chain correlation peak without clear separation. Therefore, the ring-shaped signal at high q_z may be a superposition of the chain-tilting signal and helical signal. Of course, this would then also confirm successful incorporation of the β -peptides into DOPC host bilayers, as already deduced from reflectivity.

Fig. 2.9c shows the parameters (I_0 , a and ξ) deduced from the least-square fits as a function of ϕ . Again, the analysis is based on a decomposition of chain populations as a function of ϕ [64, 140]. (i) The maximum intensity I_0 of DOPC decays rapidly with ϕ , with main chain-tilting angle $\leq 10^\circ$, similar as observed before for DOPC [64]. This reflects that the dominating fraction of lipids in the pure DOPC multibilayer are untilted. Contrarily, I_0 - ϕ curves of peptide-containing samples increase slightly with ϕ , indicating a broader distribution of chain tilt induced by tilted TMDs as well as a transmembrane conformation of the incorporated peptides. (ii) The average chain-chain distance a remains approximately constant ($4.82 \sim 5.38 \text{ \AA}$), with respect to ϕ and also between peptide-free and peptide-containing membranes. The width of all 3 β -peptides appear to be similar to DOPC so that the average chain-chain distance is not affected by peptide incorporation. (iii) For the peptide-free multibilayer, the correlation length ξ decreases with ϕ , in agreement with the fact that untilted lipids have a stronger chain-chain correlation than tilted ones [64]. In contrast for peptide-containing multibilayers, ξ is almost ϕ independent. We thus assume that the helical signal should have largely attributed to ξ at high ϕ angles.

2.4 Summary and outlook

In this chapter, we designed and synthesized two families of D- $^3\text{I}^4$ - β -peptides, one with and one without additional ^hTrp anchors. In each peptide family, two of the three peptides were labeled with iodine to yield electron density contrast in either the tail region or the center region. These β -peptides were then incorporated into DOPC bilayers and characterized by CD spectroscopy, x-ray reflectivity and GISAXS. The CD spectra demonstrate the anticipated β -helical structures for all synthesized peptides including the ones with I-labels. X-ray reflectivity and GISAXS investigations together give rise to the following consistent picture: The β -peptides are successfully inserted into the model membrane stacks and form β -helical TMDs. The positive hydrophobic mismatch is relieved by a minor helical tilt, which also induces an increase in the number of chains with corresponding tilt angles. This in turn leads to membrane thinning and to a perturbation of the acyl chain packing. Additional ^hTrp anchors can effectively diminish the peptide tilt, hence less membrane thinning.

Having obtained the desired transmembrane $^3\text{I}^4$ - β -peptides in DOPC bilayers, in the future we can proceed with the design and synthesis of SNARE analogs containing β -helical TMDs, in association with various types of recognition motifs like DNA [108] and PNA [105], and linkers with different lengths [109].

3 Preparation of SNARE-reconstituted proteomicelles, proteoliposomes and multibilayers

Part of this chapter is based on the manuscript: Y. Xu, J. Kuhlmann, M. Brennich, K. Komorowski, R. Jahn, C. Steinem and T. Salditt. Reconstitution of SNARE proteins into solid-supported lipid bilayer stacks and x-ray structure analysis. BBA – Biomembranes (submitted)

Soluble *N*-ethylmaleimide-sensitive factor attachment protein receptors (SNAREs) are a family of proteins which promote vesicle fusion [7]. Reconstituting SNAREs into supported multibilayers can provide an ideal model system for high-resolution characterizations of SNARE-induced fusion *in vitro*. However, the use of organic solvent in the conventional multibilayer preparation [15,22] inhibits the reconstitution of membrane proteins. Therefore, in this work a novel vesicle-based protein-compatible protocol was developed, which was then employed to reconstitute SNAREs into supported multibilayers via the micelle-vesicle-multibilayer pathway. This chapter is composed of (i) a brief introduction of SNAREs, (ii) basics of supported multibilayers, (iii) protein expression and purification, and the most importantly (iv) the preparation of SNARE-reconstituted proteomicelles, proteoliposomes and multibilayers.

3.1 Fundamentals of SNAREs

After the discovery in the late 1980s [141], SNAREs immediately captured a lot of attention and were extensively studied due to their great significance for neuron transmission or more generally for membrane trafficking [142]. In the early stage it was believed that complementary assemble of SNAREs was a “universal mechanism” for imparting specificity to both regulated and constitutive vesicular membrane fusion (the SNARE hypothesis [143, 144]). In this hypothesis, the SNAREs couple with each other in an anti-parallel fashion whereas the energy needed for vesicle fusion is supplied by ATP hydrolysis from NSF [145]. However, later research has shown that SNAREs self-assemble into a 4-helix bundle from the N-terminal to the C-terminal in a zipper like fashion (Fig. 3.1 [142]).

It is now commonly believed that this self-assembly supplies enough energy to overcome the repulsion between opposing membranes, pulls them into close contact and thus facilitates fusion [142, 146].

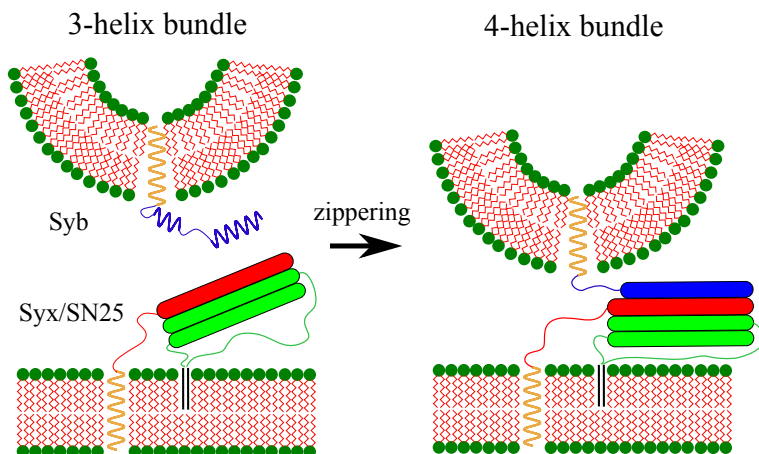


Figure 3.1: *Cartoon illustration of the zipper-like assembly of SNARE 4-helix bundle from the N-terminal to the C-terminal. Synaptobrevin (Syb) is colored in blue, syntaxin (Syx) in red and SNAP25 (SN25) in green, with all transmembrane domains (TMDs) colored in yellow. The black lines depict the palmitoyl anchors of SN25. The solid rounded rectangles present the SNARE motifs that are already assembled into the SNARE complex. The structure of Syb is drawn according to [147] and the length ratio between different SNAREs according to [148], with difference in the length of SNARE motifs between Syx and SN25 being ignored. The 1:1 complex of Syx and SN25 is readily formed before docking. The N-terminal residues are not drawn for simplicity.*

Various SNAREs are already found in *Saccharomyces cerevisiae*, in humans and in *Arabidopsis thaliana* [8]. They can be categorized into two groups, namely v-SNAREs (e.g. synaptobrevin and synaptotagmin) which anchor themselves in the synaptic vesicle membrane and t-SNAREs (e.g. syntaxin and SNAP25) which locate on the presynaptic plasma membrane. Despite the wide variety of SNAREs, they all contain SNARE motifs, which are recognized as “the minimal machinery” of membrane fusion [149]. The SNARE motifs are generally soft and flexible preceding the assembly of SNARE complexes [150]. Once formed, the coiled-coil structure is highly helical and stable, thanks to the ionic layer in the center of the coiled-coil (0 position in Fig. 3.2) and the 16 hydrophobic layers on both sides. Another important segment of SNAREs is the α -helical transmembrane domain (TMD) which can be found in both synaptobrevin and syntaxin, while SNAP25 anchors into the membrane via its palmitoyl side chain. Additionally, N-terminal domains can also be found at the distal end of many SNAREs.

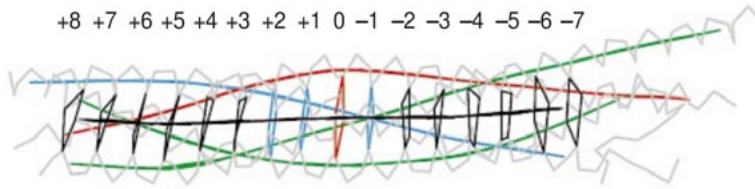


Figure 3.2: Sketch of the SNARE coiled-coil structure. α traces are painted in grey, local helical axes in blue for synaptobrevin 2, red for syntaxin-1A, green for SNAP-25B and the super-helical axis in black. The numbers above the coiled-coil structure denote the sequence of the layers, with the virtual squares indicating the central position of each layer. Adapted from [151], used with permission.

3.2 Advantages of supported lipid multibilayers

In order to simplify the study of complex biological membranes, many model lipid bilayer systems have been developed, including black lipid membranes (BLMs) [152], vesicles [153], nanodiscs [154], supported lipid bilayers [155,156], *etc.* These model bilayer systems are depicted in Fig. 3.3.

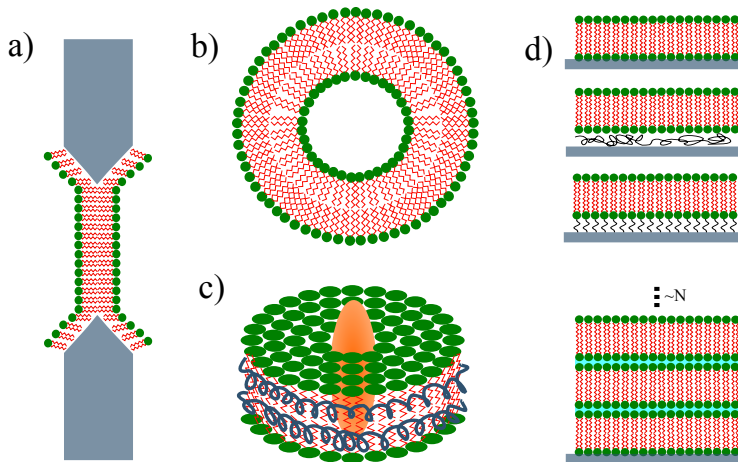


Figure 3.3: Cartoon illustration of some common model lipid bilayers: (a) black lipid membrane (BLM), (b) vesicle, (c) lipid/protein nanodisk and (d) from top to bottom: solid-supported, polymer-supported and tethered bilayer, and solid-supported multibilayer

All these model bilayers above are commonly used in membrane research and have their own advantage over others [157]. Supported lipid bilayers, either

solid-supported, polymer-supported or tethered (see Fig. 3.3d), offer a model bilayer system with remarkable membrane orientation and long-term stability, which enable high-resolution surface-sensitive characterizations such as Fourier transform infrared spectroscopy (FTIR), nuclear magnetic resonance spectroscopy (NMR), atomic-force microscopy (AFM), x-ray and neutron scattering, *etc.*, [158]. For x-ray and neutron scattering in particular, the supports used for supported bilayers not only greatly suppress thermal fluctuations of free-standing bilayers (e.g. BLMs and vesicles) which diminish the bilayer lamellar ordering [17]; They also overcome the "powder averaging" problem of some model bilayers (e.g. vesicles) and hence give rise to stronger signal for x-ray and neutron scattering [159], due to the fact the all lipid molecules align themselves along the membrane normal.

Supported lipid multibilayers are composed of tens of up to thousands of lipid bilayers on a certain support, with thin water layers isolating different bilayers. Such multibilayers have several advantages over supported single bilayers. First of all, the constraints from the solid-support are reduced. Adding a spacer layer such as polymer or tether (Fig. 3.3d) could also achieve it, [160], but at the cost of additional preparation steps and system complexity. Most bilayers within a multibilayer are distant from the substrates and thus barely affected by them [161]. Secondly, single bilayers especially the ones prepared by spreading vesicle suspensions suffer from low covering rate, while multibilayers could almost cover 100% of the substrate surfaces.

For x-ray characterization of SNAREs in model bilayers in particular, the multibilayer structure brings several advantages: (i) The multibilayers structure could tremendously amplify the diffraction signal thanks to the increased bilayer number N , especially regarding the weak signal of the incorporated proteins. In multibilayers, both the readily existing helices and the helical structure of the four-helix bundle of SNAREs [150] may be effectively detected by e.g. GISAXS, which have been performed on mixed multibilayers of lipid/peptide before [140]. (ii) The opposing bilayers within a multibilayer stack can be easily directed into close contact by means of e.g. partial dehydration, which is a prerequisite for the functioning of many membrane proteins including SNAREs [162]. (iii) Finally and most importantly, our long-term goal is to reconstruct the 3-dimensional structure of the stalk in the presence of SNAREs, based on our previous experience from pure lipid multibilayers [21].

3.3 Existing preparation methods of supported lipid multibilayers

Several preparation methods have been developed to prepare supported lipid multibilayers, including Langmuir-Blodgett monolayer transfer, spreading organic solution (sOS) and spreading vesicle suspensions (sVS) (see Fig. 3.4).

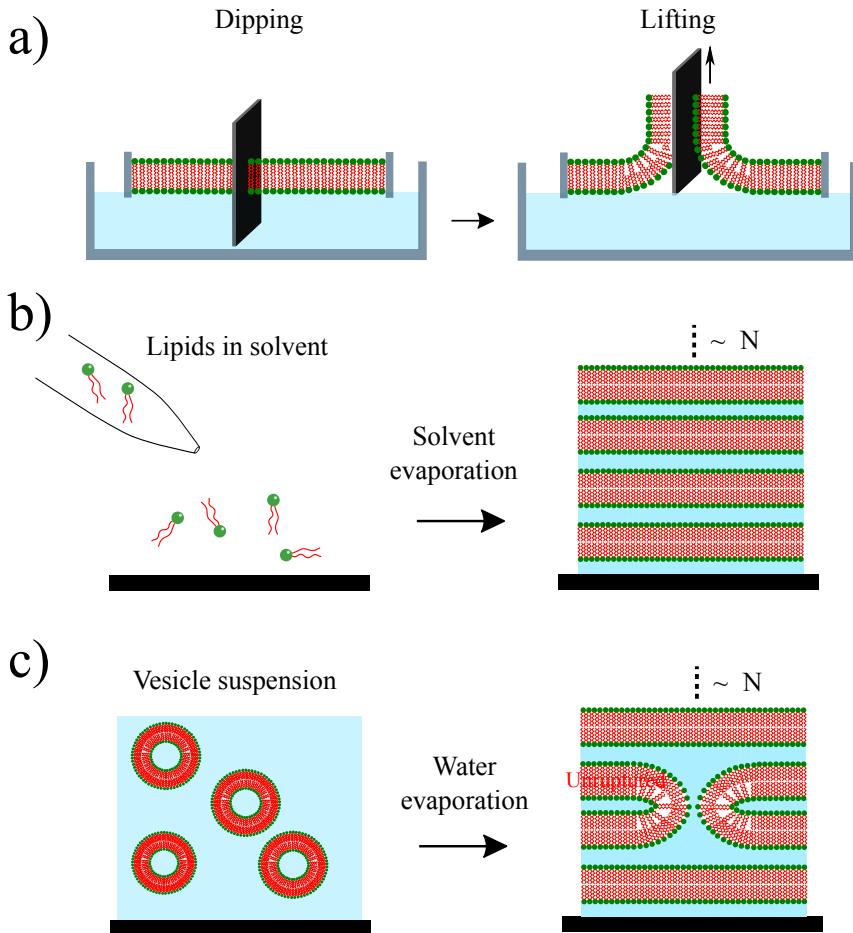


Figure 3.4: Cartoon illustration of three different preparation techniques for multibilayers: (a) Langmuir-Blodgett monolayer transfer, (b) spreading organic solution (sOS) and (c) spreading vesicle suspension (sVS). The defect in the sVS multibilayer is caused by incomplete rupture of vesicles. The lipid organic solution is painted in yellow and the aqueous suspension in blue.

3.3.1 Langmuir-Blodgett monolayer transfer

Langmuir-Blodgett (LB) monolayers can be formed by self-assembly of amphiphilic molecules (e.g. detergents and lipids) at the air-water interface, with hydrophilic headgroups immersed in water and hydrophobic acyl chains heading upwards in the air [163]. These monolayers can be transferred onto substrates by vertically dipping and lifting the substrates in and out of the fluid (Fig. 3.4a). A monolayer is then deposited onto the substrate at each withdraw. By varying the number of withdraws either a supported single monolayer, a supported single bilayer or a supported multibilayer can be fabricated [24].

One strong advantage of the LB monolayer transfer is the precise manipulation of each monolayer [158]. Moreover, transmembrane proteins could be incorporated into LB monolayers [164], and could potentially be further introduced into multibilayers with integrity. On the other hand, it takes a lot of time and efforts to prepare multibilayers with this technique, since the monolayers have to be deposited one after another. In addition, the multibilayers prepared by LB monolayer transfer can not be well reproduced because of a variety of accompanying uncertainties such as complex thermal-dynamic and kinetic behavior, monolayer compression and the transfer process itself [22]. Another shortcoming of the LB method is that the higher monolayers do not transfer so well as the lower ones. Thus one could achieve up to merely ~ 50 bilayers [165], which fails to provide sufficient sample volume to x-ray characterizations.

3.3.2 Spreading organic solution (sOS)

Spreading organic solution (sOS) (Fig. 3.4b) is the most commonly used method for supported lipid multibilayers thanks to its ease of use and high efficiency. This protocol was first systematically investigated by SEUL and SAMMON [22] over 20 years ago on dipalmitoylphosphatidylcholine (DPPC) films using x-ray diffraction and electron microscopy. They found out that a variety of membrane defects could be observed on sOS films, in contrast to the rather defect-free surfaces of LB films. Nevertheless, the sOS films are still highly oriented and able to yield up to 12 Bragg peaks for x-ray reflectivity experiment on dry films. The sOS method thus offers a rapid preparation of lipid multibilayers highly suitable for x-ray study, as long as the proper solvent mixture, lipid concentration and substrate are chosen. In this initial study, about only 50 bilayers could be fabricated. Later on, by optimizing preparation conditions, lipid multibilayers of up to several hundred or thousand bilayers could be achieved [15, 166],

yielding even higher effective sample volume for x-ray studies. It is considered as the most adequate preparation method for pure lipid [167] and lipid/peptide systems [132, 168]. However, the use of organic solvent inhibits the preparation of complex multibilayers containing membrane proteins by this method, as it may lead to protein denaturation.

3.3.3 Spreading vesicle suspension (sVS)

One of the less common preparation methods for lipid multibilayers is the spreading vesicle suspension (sVS) method (Fig. 3.4c), which can be performed both with and without proteins [169, 170]. The preparation process is composed of two main steps: (i) Lipid vesicles are first prepared, resized and refined with various techniques such as vortex, sonication, size-exclusion, extrusion, dialysis, *etc.*; (ii) Vesicle suspensions are then spread onto substrates so that vesicles rupture into planar bilayer upon evacuation. This approach is developed from the classic vesicle-based deposition of single lipid bilayers [155, 171]. The major difference between these two methods is that for single bilayer preparation only a single layer of vesicles adsorb onto the solid-supports and slowly rupture into single bilayers in the presence of buffer solutions; while for bilayer stacks bulk vesicle suspensions are forced to dry and deposit on the substrate surface to form multibilayers during water evaporation.

Results have shown that such vesicle-based multibilayers could be well characterized by x-ray reflectivity [169]. This method should be able to achieve the reconstitution of SNAREs into supported multibilayers which are suitable for x-ray characterizations. However, the orientation and lamellar ordering of such multibilayers are not yet determined and the reconstitution rate of the desired protein remains also unclear [24]. In order to properly take advantage of this method, special attention has to be paid to these two issues during the development of the novel protocol.

3.4 Expression and purification of SNAREs

3.4.1 Protein constructs

Both the SNARE expression and purification procedures follow the protocol described in detail elsewhere [172]. The SNAREs including syntaxin-1A

(Syx1A), SNAP-25B (SN25B) and synaptobrevin 2 (Syb2) from *Rattus norvegicus* were used in this study, with all expression constructs performed in *Escherichiacoli* cells with the pET28a vector. More specifically, the full length Syb2 (aa 1-116), one of the natural vesicular SNARE components, was directly used as the v-SNARE for this study, while the soluble C-terminal segment of Syb2 (aa 49-96) was assembled together with the C-terminally truncated Syx1A (aa 183-288, including its SNARE motif and TMD) and SN25B (aa 1-206, with all its cysteine replaced by serine) to form a the ΔN acceptor complex (hereinafter referred to in short as ΔN complex or simply ΔN), which was used as the t-SNARE complex for this study. The assembly process of ΔN was carried out at 4 °C for overnight with an excess of SN25B (1:1:1.5) in the presence of 1% CHAPS. All SNARE components used in this work are sketched in Fig. 3.5.

3.4.2 ΔN acceptor complex

Most of the fusion experiments of SNAREs are performed with Syb2 and the 2:1 complex of Syx1A/SN25, where the binding site of Syb2 is occupied by an extra syntaxin with its TMD being truncated (Fig. 3.5 [150, 173]). In this mechanism, the rate of full SNARE complex assembly is predominately determined by the competitive displacement between Syb2 and the extra Syx1A. Unfortunately, this rate is considerably slow (hour-scale) in contrast to the millisecond-scale fusion processes in *vi vo*. POBBATI *et al.* [148] thus developed a novel t-SNARE complex denoted as ΔN acceptor complex, which is composed of a 1:1 Syx1A/SN25 complex stabilized by the C-terminal soluble segment of Syb2 (Fig. 3.5). They found that Syb2 could bind to ΔN rapidly, similar to the unstabilized 1:1 complex of Syx1A/SN25. The reason is that the 4-helix assembly initiates from the N-termini which is not occupied in ΔN . Later research has confirmed that this novel complex does promote rapid fusion and thus enables more comprehensive monitoring of the whole fusion process [174, 175].

3.4.3 Protein purification

H-tags were first cleaved by thrombin digest overnight. A Ni²⁺-nitrilotriacetic acid affinity chromatography was then performed followed by an ion exchange chromatography. MonoQ ion-exchange column (GE Healthcare) was used for Syx1A and SN25B while MonoS (GE Healthcare) for both full length and the soluble segment Syb2. After assembly, the ΔN complex was further purified by ion

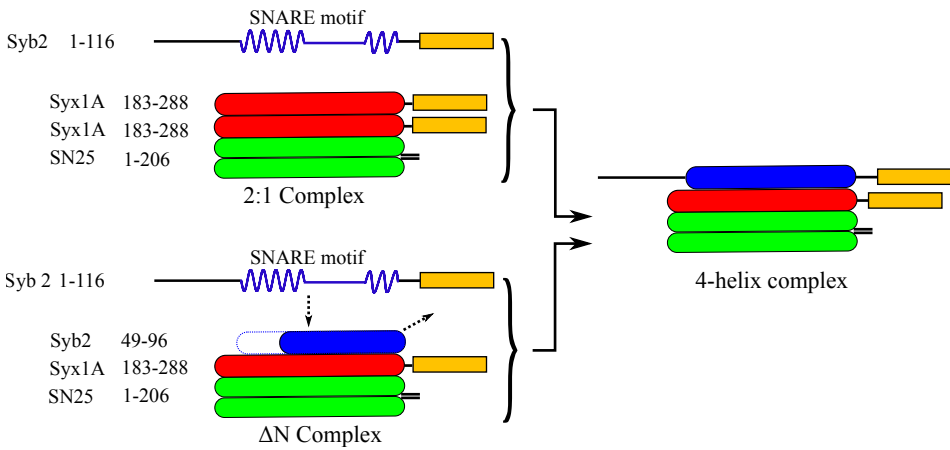


Figure 3.5: Schematic comparison of two SNARE assembly mechanisms commonly used *in vitro*. The 2:1 complex mechanism (upper) and ΔN mechanism (lower) are drawn in reference to [148, 150]. Synaptobrevin 2 (Syb2) is colored in blue, syntaxin-1A (Syx1A) in red and SNAP-25 (SN25) in green, with all transmembrane domains (TMDs) colored in yellow. The double black lines depict the palmitoyl anchors of SN25. The structure of Syb is drawn according to [147] and the length ratio between different SNAREs according to [148], with difference in the length of SNARE motifs between Syx1A and SN25 being ignored. The solid rounded rectangles present the SNARE motifs that are already assembled into SNARE complexes. The 1:1 complex of Syx1A and SN25 (3-helix bundle) is readily formed before N- to C-termini zippering.

exchange chromatography with MonoQ. The SNAREs with TMD were always handled in the presence of 1% CHAPS. Stocks containing SNAREs were snap-frozen with liquid nitrogen and stored at -80°C for further use.

3.5 SNARE reconstitution into supported multibilayers by sVS

The whole spreading vesicle suspension (sVS) protocol is illustrated by Fig. 3.6 where it is divided into three stages according to the morphology of the aggregates, namely the proteomicelle stage, the proteoliposome stage and the multibilayer stage.

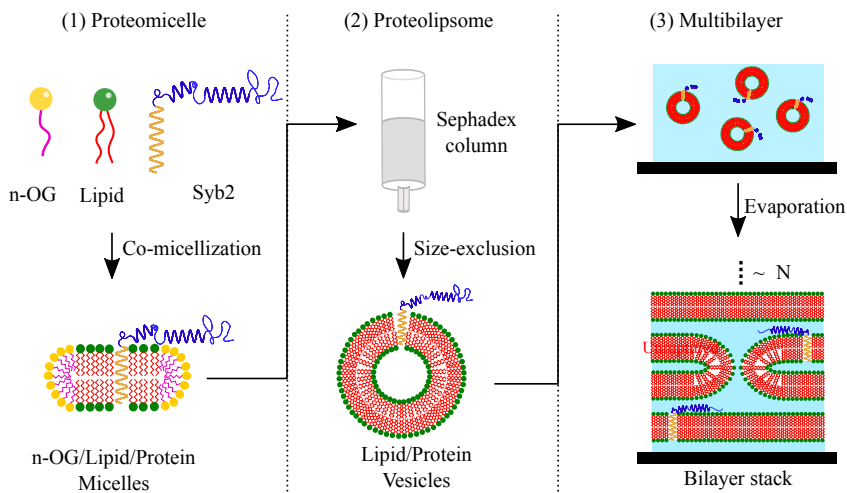


Figure 3.6: Cartoon illustration of the sVS protocol (i.e. the micelle-vesicle-multibilayer pathway). Stage 1: The SNAREs are incorporated into the detergent/lipid mixed micelles to form proteomicelles. Stage 2: After going through the Sephadex columns for 2 times, proteoliposomes transform into proteoliposomes since n-OG is removed by size-exclusion chromatography. Stage 3: Resulting proteoliposome suspension is spread onto the substrate so that supported multibilayers form upon water evaporation. Syb2 is used as an example of reconstituted SNAREs. A certain number of vesicles underwent incomplete ruptures, hence membrane defects.

3.5.1 Stage 1: proteomicelles

The proteomicelles containing SNARE were prepared by the co-micellization method following [148, 176]. All lipids were purchased from Avanti Polar Lipids (Alabaster, AL, USA) and used without further purification. Primarily two lipid mixtures were used for this thesis, the quaternary mixture of PC-PE-PS-Chol and the binary mixture of PC-PE. Among them, PC-PE-PS-Chol is close to the lipid composition of synaptic vesicle membrane (SM not included). It is thus considered highly suitable for the preparation of unilamellar vesicles and for SNARE fusion [177]. On the other hand, PC-PE mixture has been extensively reported to be able to form highly aligned supported multibilayers [21, 25, 78]. As a result, PC-PE acts as the main multibilayer-forming mixture in this study.

First of all, 1 mg of lipid mixtures with/without 0.67 wt% Texas Red (TR, Eugene, Oregon, USA) was separately dissolved by the mixed solvent of chloroform/TFE (1:1 *vol/vol*) and dried under mild nitrogen flow for 1 h. Especially, PS was dissolved by isopropanol due to its poor solubility in chloroform/TFE. The lipid

films were then dried in vacuum for 2 h to fully remove the organic solvents. 1.8 mg n-octyl- β -D-glucoside (n-OG) was added to 50 μ L buffer solution containing 20 mM 4-(2-hydroxyethyl)-1-piperazineethanesulfonic acid (HEPES), 100 mM KCl and 1 mM dithiothreitol(DTT). Due to the fact that the n-OG concentration (\sim 120 mM) was much higher than its CMC (25 mM), detergent/lipid mixed micelles formed spontaneously (Fig. 3.4a [178]). The dry lipid films were re-dissolved by the resulting n-OG micelle suspension. Subsequently, the n-OG/lipid mixed suspension was vortexed every 5 min for 3 times to homogeneously mix them. Δ N and Syb suspensions were taken out of the -80 °C freezer and thawed under room temperature. 2 aliquots (\sim 8 μ M) of either Δ N or Syb suspension containing 1% CHAPS were pipetted into the n-OG/lipid mixed micelle suspension at the protein/lipid ratio of 1:500 [176]. After incubation on ice for 30 min, SNAREs anchored into the readily formed n-OG/lipid mixed micelles, hence proteomicelles containing SNAREs. Resulting suspensions contained rather high amount of n-OG which was to be removed by the later size-exclusion chromatography.

3.5.2 Stage 2: proteoliposomes

The first Sephadex G-25 size-exclusion column (Illustra NAP-25, GE Healthcare) was equilibrated with buffer by eluting 5 ml reconstitution buffer through the column for 3 times. The proteoliposome suspensions then passed through the first column so that the n-OG could be removed. As the n-OG got washed away, proteoliposomes transformed into proteoliposomes (Fig. 3.4b) due to the decrease of the overall packing parameter. The second G-25 column was equilibrated with ultrapure water by eluting 5 ml MilliQ water through the column for 3 times as well. After eluting the vesicle suspension with the second column, the remaining salt from the buffer was also removed. After being concentrated to 10 mg/ml (Concentrator plus, Eppendorf), proteoliposome suspensions were stored in refrigerator at 4 °C for later deposition of supported multibilayers. In addition, two pure-lipid vesicle suspensions were prepared either by the same method only without SNAREs, or by sonicating 1 mg lipid film together with 2 ml ultrapure water.

3.5.3 Stage 3: supported multibilayers

Similar to the wafer processing in the last two chapters, silicon wafers (Silchem, Freiberg, Germany) were first polished, cut to 10 \times 15 mm² pieces and cleaned

by 15 m ultrasonic bath with ultrapure water and methanol iteratively for 5 times in total. Since the vesicle suspensions can not spread out so well as organic solutions on hydrophobic surfaces, here the Si wafers were especially plasma treated (PDC-002, Harrick) under constant O₂ flow for 10 m. A highly hydrophilic SiO₂ layer was then fabricated on top of each Si wafer so that the vesicle suspensions spread out once deposited. Note that the wafers should be directly used after plasma-cleaning, otherwise adsorption of dust from the air could re-hydrophobize the wafer surface.

In order to prepare multibilayers containing both ΔN and Syb, 50 μl ΔN and 50 μl Syb proteoliposome suspensions were first gently mixed and co-incubated at room temperature. Afterwards, the suspension containing both ΔN and Syb was spread onto a Si wafer which was then transported into a vacuum desiccator. Over-night evacuation was performed so that H₂O was thoroughly removed (Fig. 3.4c). As water evaporated, the vesicles began to rupture and formed planar bilayers on top of each other [179]. Noticeably, incomplete ruptures could lead to a large number of membrane defects whose effect should be carefully investigated by the x-ray characterizations below. A series of control multibilayers were prepared in parallel: (i) pure lipid multibilayer by sOS, (ii) pure lipid multibilayer by sVS, (iii) the multibilayer containing only ΔN and (iv) the multibilayer containing only Syb.

4 SAXS studies of SNARE-reconstituted proteomicelles and proteoliposomes

Part of this chapter is based on the manuscript: Y. Xu, J. Kuhlmann, M. Brennich, K. Komorowski, R. Jahn, C. Steinem and T. Salditt. Reconstitution of SNARE proteins into solid-supported lipid bilayer stacks and x-ray structure analysis. BBA-Biomembranes (submitted)

In the last chapter, I have presented the newly established sVS protocol for the reconstitution of SNAREs into supported multibilayers. This protocol is composed of three stages including the proteomicelle stage, and proteoliposome stage and the multibilayer stage. For both the proteomicelle and the proteoliposome stages, the SNARE containing aggregates exist in the suspension phase, which can be properly characterized by SAXS as well as dynamic light scattering (DLS). In this chapter, I first present the experimental setup and physical theory of solution SAXS, then seek to reveal the structural information of both micelles and vesicles with the help of appropriate fitting models, and finally evaluate the influence of preparation techniques, lipid compositions and SNARE reconstitution on micelle and vesicle structures.

4.1 Beamline BM29

The BM29 beamline (BioSAXS) is a newly upgraded beamline at ESRF particularly designed for SAXS experiments on biological macromolecules in solution [180]. It features tunable beam energy (7-15 keV, 12.5 keV by default), higher flux (up to 2×10^{13} photons/s) and smaller beamsize ($\leq 500 \times 500 \mu\text{m}$) compared to the previous ID14-3 beamline. These upgrades enable high-resolution SAXS detection in relatively short time scale.

The BM29 beamline (Fig. 4.1) is located on the bending-magnet dipole with a 0.85 T magnetic field and a 20.35 keV critical energy. After passing through the white beam slits and the water-cooled mask, the x-ray beam is monochromated by a water-cooled double multilayer monochromator, whose exit beam shifts slightly ($5 \mu\text{m}$) when the beam energy varies. A set of metal filters are installed right behind the monochromator. They are made of Fe, Cu and Pt re-

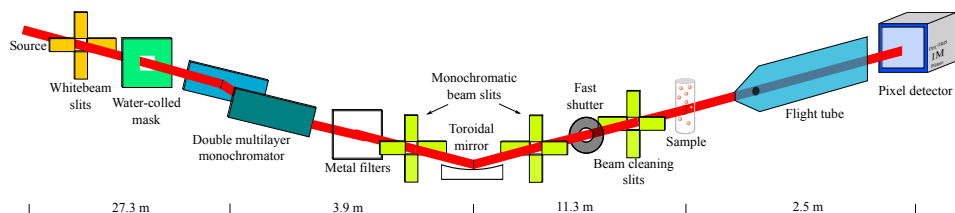


Figure 4.1: *BM29 beamline layout adapted from [180], re-drawn with permission. The distances between key components are noted under the layout. The toroidal mirror converts the divergent beam to convergent, which is not shown in the layout. The detector can be moved accordingly to provide the proper q range.*

spectively, whose adsorptions edges fall right in the energy range of the beam. Further downstream a 1.1 m Rh coated cylindrical toroidal mirror is installed to focus the monochromated beam. Finally the beam is defined by a set of beam cleaning slits, which deliver a $0.7 \times 0.7 \text{ mm}^2$ size beam on the sample with $130 \mu\text{rad}$ divergence. A flight tube, a beamstop (located in the flight tube), a diode (integrated into the beamstop) and a Pilatus 1M detector (DECTRIS) are placed downstream the sample position. Pilatus 1M is a pixel detector composed of 10 units and 981×1043 pixels in total ($172 \times 172 \mu\text{m}^2$ each pixel). The sample-detector distance can be adjusted accordingly with respect to the desired q range. The BM29 beamline is aimed at high throughput as well as the ease of use. To this end, the entire beamline is highly automated on both the hardware and software sides as shown below.

4.1.1 Automatic sample changer

The sample changer is equipped with a robot system of multiple functions: automatic sample loading and unloading, sample chamber cleaning and drying, which are controlled by a simple software installed right next to the sample changer (Fig. 4.2 [183]). Three types of sample plates can be used for sample storage: (i) metal plate with 4×8 sample positions for standard PCR tubes (0.2 ml, Eppendorf, Germany) and 4×8 buffer positions for microcentrifuge tubes (1.5 or 2.0 ml, Eppendorf, Germany), (ii) 96 well plate with shallow wells and (iii) 96 well plate with deep wells. The internal temperature can be set between 2-60 °C. More importantly, after the samples are loaded and the experimental hutch closed, all sample/buffer delivery as well as x-ray exposures are controlled by the beamline operating software BsxCuBE [183].

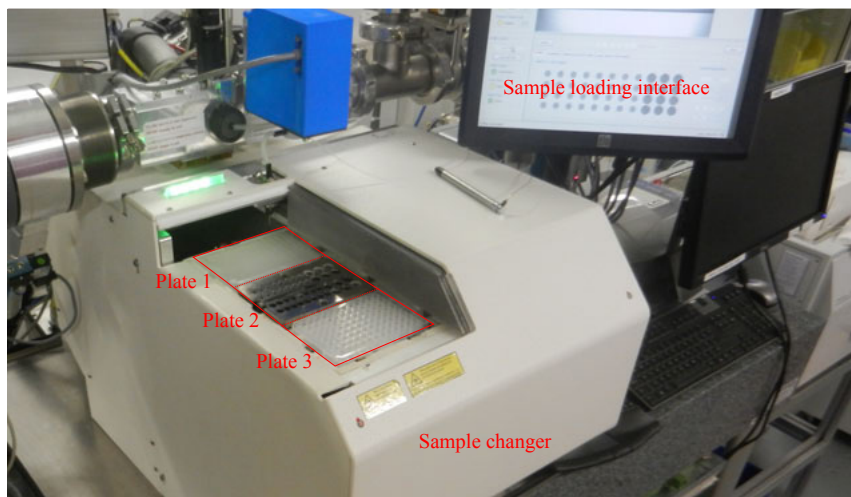


Figure 4.2: The automatic sample changer system of BM29 beamline [181, 182]. All three types of samples plates are mounted in the loading position of the sample changer in the photo. Functions like sample loading/unloading, chamber cleaning/drying and temperature control are achieved using the sample loading interface shown in the upper right corner.

4.1.2 BsxCuBE operating software, EDNA pipeline and ISPyB database

The BsxCuBE (Biosaxs Customized Beamline Environment) operating software is installed on the main computer in the control hut. After mounting the sample solutions into one or more of the three sample plates and loading them, users can edit the sample information and choose experimental parameters using the BsxCuBE software before starting a measurement. Sample information could be input by editing the excel-like interface as shown in Fig. 4.3 [182, 183]. Essential information that users have to constantly modify includes type (buffer or sample), row (A-D for the metal plate), concentration (mg/ml), well (1-11 for the metal plate), name of the macromolecule, name of the buffer and volume (20-120 μl , ideally 50 μl). Note that this table should be saved as a new file prior to exposures. Later a couple of other parameters shall be carefully chosen for the entire measurement. They include directory, prefix, run, frame (10 by default), time per frame (1 s by default) and radiation damage. With all these being set, the users can finally open the shutter (the “open” button) and start the measurement (the “collect” button). BsxCuBE will automatically run the measurement according to the given sample sequence. Immediately after

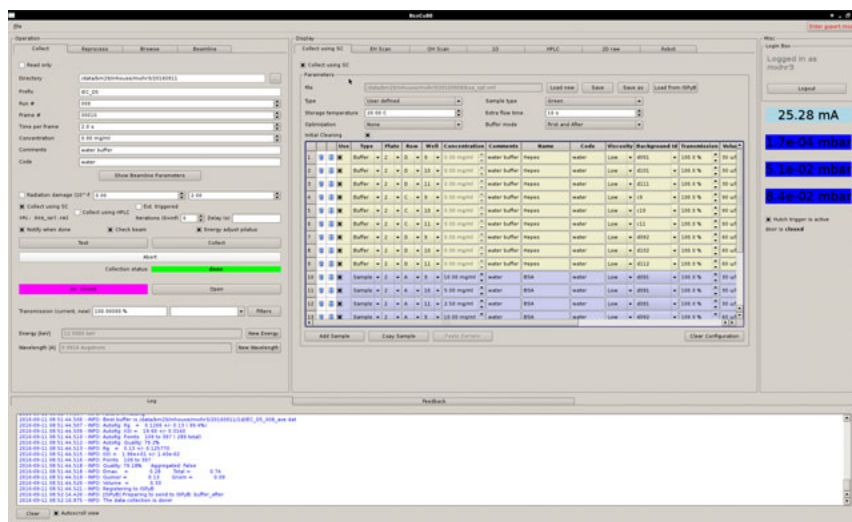


Figure 4.3: Snapshot of BsxCuBE interface [182, 183] to start a measurement. Sample information can be input into the excel-like table. After giving the experimental conditions, the software runs the measurement automatically and converts 2d exposures to 1d curves. [182]

recording, 2d exposures are azimuthally integrated to yield a series of 1d intensity profiles.

The EDNA-driven [184] online data-processing pipeline first disposes the exposures with radiation damage, averages the chosen 1d intensity profiles and subtracts the SAXS data of buffer solution from the SAXS curves of the suspensions. Later on, it also performs “routine” data analysis including Kratky analysis, Guinier approximation and Porod approximation [180]. In the end, the sample information table, data processing and routine data analysis are uploaded to the ISPyB (Information System for Protein crystallography Beamlines) database (Fig. 4.4 [185]). Users are able to view, edit and download them after logging in to the ISPyB website with their user account.

4.1.3 Experimental settings

All suspensions prepared in the last chapter were characterized at BM29 BioSAXS beamline with identical beamline settings. Briefly, the photon energy was set to 12.5 keV and the beam size was set to $700 \times 700 \mu\text{m}^2$ at the exposure capillary by the beam-cleaning slits. The Pilatus 1M detector was mounted

Name	Type	Macromolecules	Status	Download	Measurements	Averaged	Subactions	Time
plate19.vml	STATIC	DOPS_HMNCAGI	FINISHED	Download	3 of 3	3 of 3	3 of 3	09:09:22
plate19.vml	STATIC	DOPS_HMNCAGI	FINISHED	Download	32 of 32	32 of 32	33 of 33	08:14:07
plate19.vml	STATIC	Delhi_SybioB	FINISHED	Download	19 of 14	12 of 14	5 of 4	07:13:48
plate19.vml	STATIC	DOPS_MQ_100	FINISHED	Download	46 of 46	46 of 46	36 of 36	06:04:49
plate18.vml	STATIC	DOPCOPEDOP	FINISHED	Download	36 of 36	36 of 36	32 of 32	03:46:16
plate14.vml	STATIC	DOPCOPEDOP	FINISHED	Download	24 of 24	24 of 24	33 of 33	01:09:15
plate14.vml	STATIC	DOPC_DOPC_D	FINISHED	Download	3 of 3	3 of 3	1 of 1	00:12:27
plate14.vml	STATIC	DOPC_DOPC_S	FINISHED	Download	27 of 26	27 of 26	3 of 3	23:12:49
plate14.vml	STATIC	DOPC_DOPC_D	FINISHED	Download	12 of 12	12 of 12	5 of 5	22:35:40
plate13.vml	STATIC	POPEP_Sp_1	FINISHED	Download	24 of 24	24 of 24	3 of 3	19:02:39
plate12.vml	STATIC	POPEP_Sp_P	FINISHED	Download	30 of 30	30 of 30	33 of 33	17:35:14
plate12.vml	STATIC	POPEP_Sp_P	FINISHED	Download	2 of 32	2 of 32	9 of 31	17:06:39
plate10.vml	STATIC	DOPC_DOPS_D	FINISHED	Download	17 of 17	17 of 17	9 of 9	15:56:09
plate10.vml	STATIC	POPE_41_Delhi	FINISHED	Download	12 of 12	12 of 12	33 of 33	14:51:58
plate9.vml	STATIC	PC_PC_41_mon	FINISHED	Download	11 of 11	11 of 11	33 of 33	12:24:19
plate8.vml	STATIC	POPE_41_POPE	FINISHED	Download	3 of 3	3 of 3	4 of 4	10:22:36
plate5.vml	STATIC	Svb_1_2_ONES	FINISHED	Download	19 of 19	19 of 19	9 of 9	03:46:26
plate5.vml	STATIC	Delhi_SybioB	FINISHED	Download	7 of 7	7 of 7	3 of 3	00:56:52

Figure 4.4: Typical user interface of ISPyB (Information System for Protein crystallography Beamlines) online database. Users can view, edit and download the sample information, experimental parameters, 1d data processing and results of routine analysis online anytime with their user account.

2.867 m away from the capillary, resulting in a q range between 0.003 - 0.495 \AA^{-1} . Sample suspensions and pure buffer solutions (HEPES buffer for micelles and MillQ water for vesicles) were first pipetted into the automatic sample changer before measurements. For micelles, the original suspensions ($\sim 1 \text{ mg/ml}$) were used. For vesicles, both the original suspensions and concentrated suspensions (~ 5 - 10 mg/ml) were measured. After properly setting the sample information and measurement parameters, BsxCuBE then automatically delivered the sample suspensions and buffer solutions into the exposure capillary and recorded 10 frames of 1 s for each suspension/solution. The EDNA-driven pipeline automatically performed routine analysis, which failed to provide structural information of the micelles and vesicles as it is designed for solution SAXS of macromolecules. We thus performed specific structural analysis with proper models as shown below.

4.2 General SAXS theories

Small-angle x-ray scattering is a powerful technique to probe a wide variety of macromolecules and particles from the nm up to μm scale, which is relatively large compared to the short wavelength of x-ray (e.g. 1.54 \AA for $\text{Cu-K}\alpha$ emission) [186]. Therefore, the corresponding x-ray scattering signal of such macromolecules and particles fall into the small angle range, in contrast to the wide angle of atomic structures.

Fig. 4.5 sketches the typical data collection process of SAXS experiments. A monochromatic x-ray beam is first defined by a series of x-ray optics such as pinholes. Considering the fact that small-angle x-ray signal can be easily affected by misalignment of the beam or the scattering from the optics [187], special attention has to be paid to delivering clean beam onto the sample. The well-aligned x-ray beam then hits the sample and is scattered by the macromolecules inside the sample-holding capillary, with the scattering signal interfering with each other. The scattered wave projects onto a pixel detector to yield a 2-dimensional (2d) diffraction pattern. The pixel detector is usually mounted far away from the sample so that more information in the small-angle regime can be detected. Finally, the 2d diffraction pattern is azimuthally averaged, resulting in 1-dimensional (1d) intensity profiles against the incident angle θ or scattering vector modulus q , with $q = 4\pi \sin\theta / \lambda$ [188].

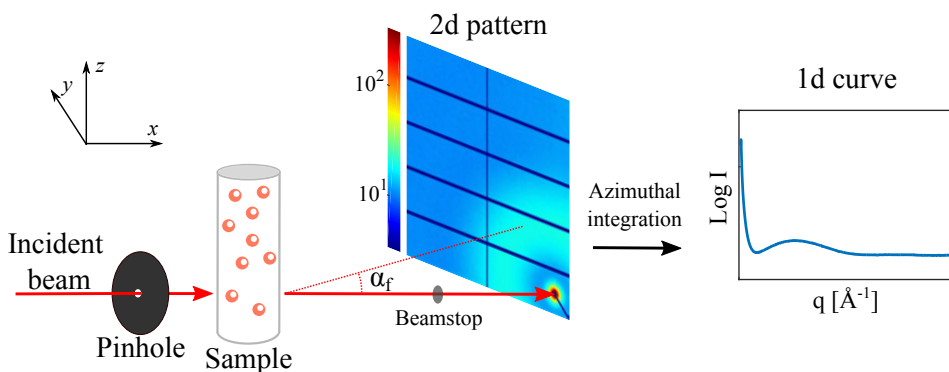


Figure 4.5: Schematic illustration of typical SAXS data collection. A monochromatic beam first passes through a set of pinholes, strikes the sample and scatters onto a 2d pixel detector. After being azimuthally integrated the intensity I is plotted against the scattering vector modulus q to yield 1d I - q plot. Both 2d and 1d results are plotted in logarithmic scale.

The scattering intensity of an ideal single particle I_{sp} in vacuum is proportional to the square of its form factor F_{sp} :

$$I_{sp} \sim |F_{sp}(\mathbf{q})|^2 = \left| \int_{V_{sp}} \rho_{sp}(\mathbf{r}) \cdot \exp(i\mathbf{q} \cdot \mathbf{r}) d\mathbf{r} \right|^2. \quad (4.1)$$

\mathbf{q} is the scattering vector in reciprocal space and \mathbf{r} is the position vector in real space. Since particles do not exist on their own, we should consider the scattering from the environment (e.g. aqueous solution for lipidic aggregates) so that

$$I_{sp} \sim |F_{sp}(\mathbf{q})|^2 = \left| \int_{V_{sp}} \Delta\rho(\mathbf{r}) \cdot \exp(i\mathbf{q} \cdot \mathbf{r}) d\mathbf{r} \right|^2. \quad (4.2)$$

Here $\Delta\rho$ is the electron density contrast between a particle and its environment. When bulk particles coexist in one environment and are distant from each other (i.e. weak inter-particle correlation), the total scattering intensity is simply a summary of intensities of all particles [188]. For anisotropic particles, an averaging over all directions has to be performed [189], yielding

$$I_{av} \sim \langle |F_{av}(\mathbf{q})|^2 \rangle = \int_0^{2\pi} d\Phi \int_0^\pi |F_{sp}(\mathbf{q})|^2 \sin\theta d\theta. \quad (4.3)$$

Here Φ_r and θ_r are the polar and azimuthal angles in the spherical coordinate system, respectively. For particles of different shapes, the form factors can be further derived with proper models. In particular, the modeling of micelles and vesicles will be presented below. Here the scattering intensity is denoted in kDa based on the molecular weight derived from the forward scattering intensity I_0 [183, 190, 191].

4.3 SAXS modeling and fitting of proteomicelles

Micelles are aggregates of surfactants mostly formed in aqueous solutions, with a hydrophilic headgroup shell separating the solution and inner hydrocarbon core [192]. Micelles can adopt several different shapes such as sphere, ellipsoid (globular shape) and cylinder [193]. For each of these shapes, a specific model can be applied to calculate its form factor F .

4.3.1 The form factor of cylindrical micelles

For a uniform (the electron density ρ is a constant) cylindrical particle with radius R and height $2H$, its form factor can be written as [194]:

$$F_c(q) = 2V_c \Delta\rho \frac{\sin(u_H)}{u_H} \times \frac{J_1(u_R)}{u_R}, \quad (4.4)$$

where $u_H = qH \cos\theta$, $u_R = qR \sin\theta$ and the cylinder volume $V_c = 2\pi HR^2$. J_1 is the first order spherical Bessel function. As we have introduced above, each surfactant micelle consists of a hydrophilic shell and a hydrophobic carbon core. Hence we can treat them as two-component cylinders with inner radius R_1 , inner electron density ρ_1 , outer radius R_2 and outer density ρ_2 . By adding up the form factor of the shell and the core, we obtain

$$F_c(q) = 2V_1(\rho_1 - \rho_2) \frac{\sin(u_H)}{u_H} \times \frac{J_1(u_{R1})}{u_{R1}} + 2V_2(\rho_2 - \rho_s) \frac{\sin(u_H)}{u_H} \times \frac{J_1(u_{R2})}{u_{R2}}. \quad (4.5)$$

With Eq. 4.3 we then perform the orientational averaging [189, 195], yielding

$$\begin{aligned} \langle F_c(q)^2 \rangle = \int_0^\pi & \left[2V_1(\rho_1 - \rho_2) \frac{\sin^2(u_H)}{u_H^2} \times \frac{J_1^2(u_{R1})}{u_{R1}^2} + \right. \\ & \left. 2V_2(\rho_2 - \rho_s) \frac{\sin^2(u_H)}{u_H^2} \times \frac{J_1^2(u_{R2})}{u_{R2}^2} \right]^2 \sin\theta d\theta. \end{aligned} \quad (4.6)$$

4.3.2 The form factor of spherical and ellipsoidal micelles

The form factor of a uniform sphere can be written as [196]

$$F_s(q) = 3V_s \Delta\rho \frac{\sin(qr) - qr \cos(qr)}{(qr)^3} = 3V_s(\rho - \rho_s) \frac{J_1(qr)}{qr}, \quad (4.7)$$

in which V_s is the volume of the sphere, and J_1 is the first order spherical Bessel function. For an ellipsoid with one axis of length a and two axes of length b (spheroid) as illustrate in Fig 4.6, the qr term can be replaced by $u = q(a^2 \cos^2\theta + b^2 \sin^2\theta)^{1/2}$. θ is again the polar angle in spherical coordinate system. The form factor of an ellipsoid F_e can be written as

$$F_e(q) = 3V_s(\rho - \rho_s) \frac{J_1(u)}{u}. \quad (4.8)$$

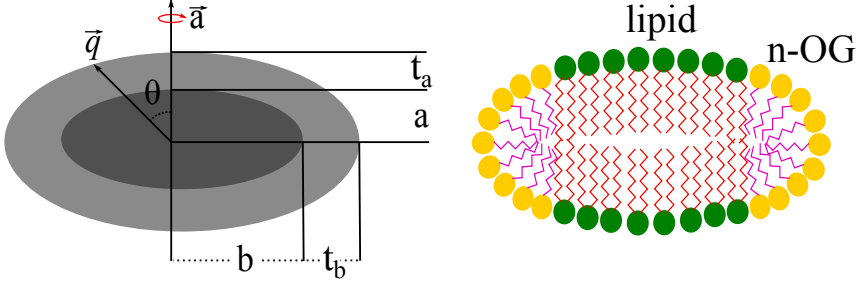


Figure 4.6: Left: Sketch of the 2-component ellipsoid model, which is composed of 1 semi-axis of length a and 2 semi-axis of length b , with t_a and t_b being the corresponding thickness of the outer shell. Right: Molecular illustration of possible arrangement of the detergents and lipids in our mixed micelles.

Similar to the two-component cylinders, here we introduce two-component ellipsoids with two discrete electron densities: ρ_1 for the core and ρ_2 for the shell. The total form factor is obtained by adding up the form factor of the inner core and outer shell, yielding

$$F_e(q) = (3V_1(\rho_1 - \rho_2) \frac{J_1(u_1)}{u_1} + 3(V_1 + V_2)(\rho_2 - \rho_s) \frac{J_1(u_2)}{u_2}), \quad (4.9)$$

in which ρ_s is the electron density of the solution, $u_1 = q(a^2 x^2 + b^2 \sin^2 \theta)^{1/2}$, $u_2 = q((a + t_a)^2 \cos^2 \theta + (b + t_b)^2 \sin^2 \theta)^{1/2}$, the inner volume $V_1 = 4/3\pi ab^2$, and the total volume $V_1 + V_2 = 4/3\pi(a + t_a)(b + t_b)^2$, with a and b being the axis length of the inner core and t_a and t_b being the thickness of the outer shell (see Fig. 4.6). Micelles are oblate if $a < b$, spherical if $a = b$ and prolate if $a > b$. Finally performing orientational averaging with Eq. 4.3 results in [195, 196]

$$\langle F_e(q)^2 \rangle = \int_0^\pi \left[(3V_1(\rho_1 - \rho_2) \frac{J_1(u_1)}{u_1} + 3(V_1 + V_2)(\rho_2 - \rho_s) \frac{J_1(u_2)}{u_2}) \right]^2 \sin \theta d\theta. \quad (4.10)$$

4.3.3 SAXS fitting of n-OG/PC-PE-PS-Chol micelles with the ellipsoid model

LIPFERT *et al.* have successfully fitted the n-OG micelles with the 2-component ellipsoid model [196, 197]. We apply this model to fit the SAXS data of our OG/lipid mixed micelles and n-OG/lipid/SNARE proteomicelles. Additionally, a scaling factor s and a constant background f are introduced to yield the final intensity, with

$$I_e = s \langle F_e(q)^2 \rangle + f. \quad (4.11)$$

The *lsqnonlin* function from the Optimization Toolbox in MATLAB (MathWorks Inc.) is used to perform the fitting. The goodness of fit is evaluated by the the reduced χ^2 [198, 199]:

$$\chi_{red}^2 = \frac{\sum_{n=1}^N \frac{(I_{exp_n} - I_{fit_n})^2}{\sigma_n^2}}{N - p - 1}. \quad (4.12)$$

I_{exp_n} and I_{fit_n} are the experimental and fitted intensities of the n^{th} data point, respectively. σ_n is the Poisson error of the n^{th} data point. p is the number of free model parameters to N data points. Appendix B.2 shows the MATLAB script to calculate the scattering intensity. In total 9 free parameters are fitted, including a , b , t_a , t_b , ρ_1 , ρ_2 , s and f .

First of all, we use n-OG/PC-PE-PS-Chol 5:2:2:1 mixed micelles as an example to figure out the proper fitting strategy for our micelle data. The SAXS curve of the n-OG/PC-PE-PS-Chol 5:2:2:1 micelle suspension is subtracted by the data of buffer. Both prolate and oblate fitting are performed within the q range of 0.050 - 0.495 \AA^{-1} . Fitting curves are compared with the experimental curves in Fig. 4.7, and the fitting results are summarized in Tab. 4.1.

Fig. 4.7 shows the experimental and fitting curves of the (a) oblate and (b) prolate ellipsoid model. Generally both models are able to roughly describe the SAXS data, with only minor residuals being observed. However, systematic discrepancies appear in both cases, indicative of an oversimplified model. In particular, the present mixed micelles cannot be fully characterized by a uniform headgroup, as they incorporate both lipids and detergents in the highly mixed regions. The two-component ellipsoid model may therefore fail to properly fit the data, accentuating the usual deficiencies of the model in the high q range [196, 200]. For the prolate shape, a more significant 1st minimum ($q = 0.09$ - 0.11 \AA^{-1}) can be observed on the experimental curve rather than on the fit. This is unlikely to happen in SAXS curve fitting as many experimental conditions tend to smear out low-intensity SAXS signal. Next we inspect the structural parameters obtained from fitting.

Tab. 4.1 tabulates the fitting results of Fig. 4.7. The geometrical parameters, namely a , b , t_a , t_b . Both shapes result in reasonable inner core thickness a and b , which are comparable to the literature values [49, 196]. The outer shell thickness t_a and t_b however, vary dramatically with the shapes. The oblate shape leads to unequal t_a and t_b , i.e. heterogeneous lipid and n-OG distribution. In contrast, t_a and t_b of the prolate model are almost equal, indicating homogeneously mixed micelles. As discussed above, such a homogeneous molecular

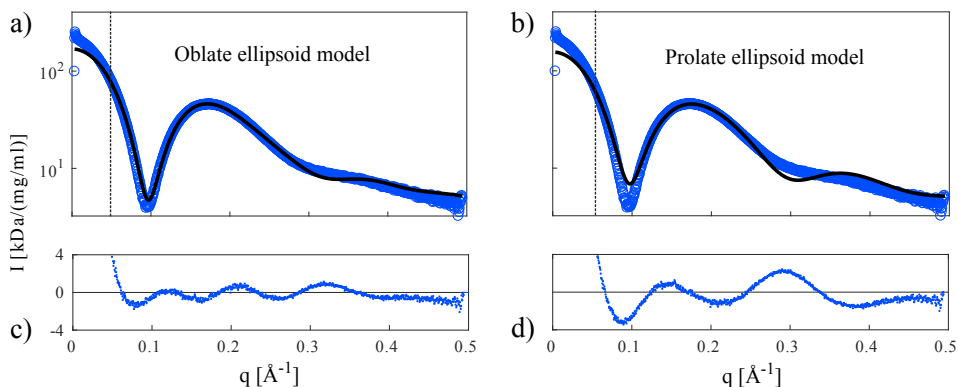


Figure 4.7: SAXS curves (blue) and fits (black) of *n*-OG/PC-PE-PS-Chol 5:2:2:1 mixed micelles using different fitting strategies: (a) oblate ellipsoid model and (b) prolate ellipsoid model. The corresponding fitting residuals are plotted underneath. Only data in the q range of 0.050 - 0.495 \AA^{-1} is fitted, as indicated by the vertical dashed lines.

Shape	$a[\text{\AA}]$	$b[\text{\AA}]$	$\rho_1[e/\text{\AA}^3]$	$\rho_2[e/\text{\AA}^3]$	$t_a[\text{\AA}]$	$t_b[\text{\AA}]$	s	f	χ^2_{red}
Oblate	11.66 ± 0.22	28.65 ± 0.34	0.24 ± 0.00	0.46 ± 0.01	11.09 ± 0.41	3.38 ± 0.17	1.44×10^{-5}	4.19	22.22
Prolate	27.55 ± 1.51	14.34 ± 0.32	0.20 ± 0.00	0.44 ± 0.01	9.01 ± 0.84	9.26 ± 0.77	1.24×10^{-5}	4.78	123.54

Table 4.1: Fitting results of *n*-OG/PC-PE-PS-Chol 5:2:2:1 mixed micelles using different fitting strategies, as shown in Fig. 4.7. Values after \pm denote the standard deviations.

distribution in the mixed micelles should not result in systematic discrepancies between SAXS curves and their fits. We then take a look at the electron densities ρ_1 and ρ_2 . Compared with literature values [76, 196], the oblate model provides reasonable results for both ρ_1 and ρ_2 , whereas the electron densities of the prolate model are significantly lower than the values therein. Lastly, the reduced χ^2 of the oblate model is profoundly lower, also indicating that the oblate shape is more suited to our micelle data. Based on reasons above, we deduce that the mixed micelles in this study adopt the oblate ellipsoid shape. This result is well in line with previous observations that *n*-OG/PC micelles are “flattened” [201, 202]. As all the mixed micelles in this study share the same main composition (*n*-OG/PC-PE-PS-Chol), the oblate ellipsoid model is hence also used to fit the SAXS data of proteomicelles below.

4.3.4 SAXS fitting of n-OG/PC-PE-PS-Chol/SNARE proteomicelles with the oblate ellipsoid model

Having determined the proper fitting model, we now use it to fit the SAXS data of SNARE-reconstituted proteomicelles. Three types of micelles exist in our preparation, namely (i) n-OG/PC-PE-PS-Chol 5:2:2:1 micelles, (ii) n-OG/PC-PE-PS-Chol/ Δ N proteomicelles and (iii) n-OG/PC-PE-PS-Chol/Syb proteomicelles. Their SAXS data are fitted with the 2-component oblate ellipsoid model introduced above.

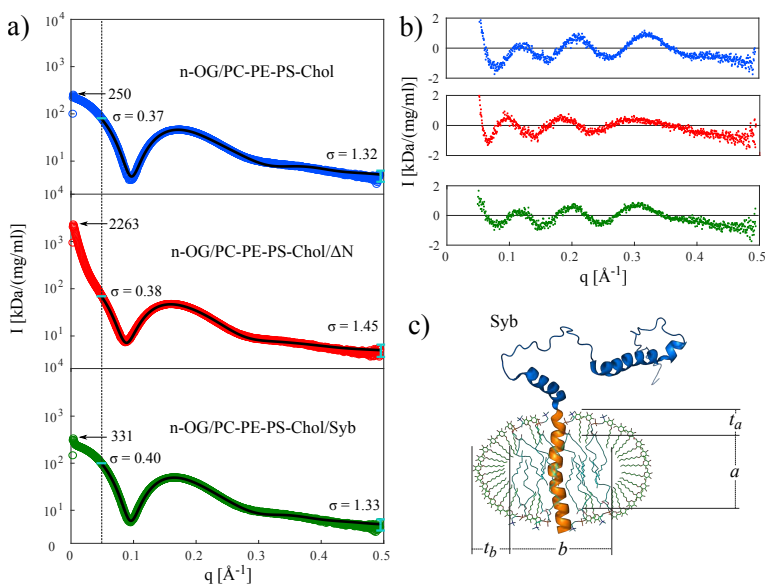


Figure 4.8: (a) SAXS curves (colored circles) and their fits (black lines) of (i) n-OG/PC-PE-PS-Chol, (ii) n-OG/PC-PE-PS-Chol/ Δ N, and (iii) n-OG/PC-PE-PS-Chol/Syb micelles, plotted on a logarithmic scale. The micelle mass concentration (total surfactant and lipid) is ~ 36 mg/ml. Data in the q range of 0.050 - 0.495 \AA^{-1} is fitted, as indicated by the vertical dashed line. The intensities at $q \rightarrow 0$ are marked by arrows. By virtue of the instrument's calibration in absolute units, the scattering intensity can be expressed in terms of (effective) molar mass of an equivalent protein solution. The experimental errors of the first and last fitted data points are plotted in cyan. (b) Residuals of the two-component ellipsoid fits corresponding to the fits shown in (a). (c) 2d sketch of the possible molecular arrangement of the n-OG/PC-PE-PS-Chol/Syb proteomicelle, using the micelle size determined by fitting (Tab. 4.2) and PDB molecular structures. The sketch is assembled "by hand" using PyMOL.

Fig. 4.8a shows the SAXS curves (colored circles) of (i) n-OG/PC-PE-PS-Chol, (ii) n-OG/PC-PE-PS-Chol/ Δ N, and (iii) n-OG/PC-PE-PS-Chol/Syb micelles. All

Samples	$a[\text{\AA}]$	$b[\text{\AA}]$	$\rho_1[e/\text{\AA}^3]$	$\rho_2[e/\text{\AA}^3]$	$t_a[\text{\AA}]$	$t_b[\text{\AA}]$	s	f	χ_{red}^2
n-OG/PC-PE-PS-Chol	11.66±0.22	28.65±0.34	0.24±0.00	0.46±0.01	11.09±0.41	3.38±0.17	1.44×10^{-5}	4.19	22.22
n-OG/PC-PE-PS-Chol/ Δ N	11.97±0.11	36.82±1.29	0.24±0.00	0.47±0.01	12.64±0.26	5.00±0.40	0.67×10^{-5}	4.44	8.56
n-OG/PC-PE-PS-Chol/Syb	11.87±0.13	31.40±0.43	0.25±0.00	0.47±0.01	12.59±0.27	2.71±0.22	1.10×10^{-5}	4.42	12.80

Table 4.2: *Fitting results of the SAXS data of n-OG/PC-PE-PS-Chol (5:2:2:1), n-OG/PC-PE-PS-Chol/ Δ N and n-OG/PC-PE-PS-Chol/Syb micelles. Only data in the q range of $0.050\text{-}0.495 \text{ \AA}^{-1}$ is fitted, using the two-component oblate ellipsoid model.*

curves exhibit the typical functional form of micelles [203], with only small systematic changes except for $I(q \rightarrow 0)$, where the curve corresponding to the Δ N-containing micelles exceeds the value of the Syb-containing micelles by a factor of about 7 and that of the protein-free micelles by a factor of 9. This change is indicative of a certain degree of protein aggregation, as we discuss further below. As a model-free parameter, the dominant head group to head group length L can be derived from the 2^{nd} peak positions without any model fit [197]. All mixed micelles showed similar L (36.61-40.02 \AA), with the SNARE-containing micelles being slightly larger (40.02 \AA for Δ N and 37.85 \AA for Syb) than the pure n-OG/lipid micelles (36.61 \AA). These parameters are verified by model fitting using the two-component oblate ellipsoid model that we have determined above, which introduces more micelle structural parameters. The fits are plotted in Fig. 4.8a (black lines) and the fitting parameters are summarized in Tab. 4.2. For all micelles, the model fits describe the experimental data sufficiently well in the fitted region ($q = 0.050\text{-}0.495 \text{ \AA}^{-1}$), as indicated by the low fitting residuals plotted in Fig. 4.8b.

Parameters in Tab. 4.2 show that the geometrical parameters, namely the core thickness a and b , the shell thickness t_a and t_b , increase only slightly for the SNARE-containing suspensions, in good agreement with the model-free parameter L above. In order to interpret these structural results, we must keep in mind that the SAXS corresponds to an ensemble, i.e. an average over SNARE-containing and SNARE-free micelles within the illuminated volume. According to the stoichiometric estimation in Appendix C.1 we expect only $\sim 9\%$ of the micelles to contain a SNARE protein. The SAXS signal is thus dominated by the protein-free micelles, which explains the observation that all curves give very similar micelle parameters. However, larger aggregations must be present in the Δ N-containing solution. To see this, we first compute an upper bound for the total mass of a SNARE-containing micelle. From the fitted geometrical form factors of the micelles and the known composition and stoichiometry of

surfactants and lipids, we obtain values in the range of 70-80 kDa. We add it to the molecular masses of the protein $M_{\Delta N} = 40.993$ kDa, or $M_{Syb} = 12.69$ kDa, respectively, and compare this sum to the molecular mass extracted from $I(q \rightarrow 0)$ of the calibrated scattering intensity. Note that the molecular masses of the instrument apply to protein solutions, assuming a protein mass density of $\rho_P = 1.35$ g/cm³ [191]. Therefore, $I(q \rightarrow 0) = 2263$ kDa/(mg/ml) of the ΔN curve must be scaled with the corresponding contrast ratio (micelle-to-water/protein-to-water). Taking this into account along with the concentration $c \simeq 36$ mg/ml, we get values well in excess of 120 kDa, which we consider evidence of aggregation. At the same time, we presume that not all ΔN -containing micelles aggregate based on the clarity of the solution. Finally, we note that in view of problems associated with aggregation and averaging over inhomogeneous scatterers, the systematic discrepancies are not surprising, but since the residuals are comparable for all curves, we still conclude that the main limitation of this model is the over-simplistic description of the micellar structure [196, 200]. Nonetheless, the small averaged expansion of the micelles does indicate a measurable response of the system to SNARE reconstitution into the n-OG/lipid micelles, so that the SNARE reconstitution into vesicles can be subsequently performed.

4.4 SAXS modeling and fitting of pure lipid vesicles and SNARE-reconstituted proteoliposomes

Several models can be used to calculate the vesicle form factor F . Among them, the two most common are the sphere model and the flat bilayer model. They are both able to properly model a large variety of vesicles [204]. In this section, the form factors of these two models are derived from literature [189, 204], while only the flat bilayer model is applied to actual vesicle fitting due to its simplicity. Fitting results of both pure lipid vesicles and SNARE-reconstituted proteoliposomes are presented. For pure lipid vesicles in particular, not only the commonly used vesicle-forming mixture PC-PE-PS-Chol [172] but also other lipid mixtures including PC-PE, PC-PE-Chol, PC-PE-PIP₂, *etc.* are investigated, in order to shed light on the effect of lipid composition on vesicle structures.

4.4.1 Gaussian electron density profiles

Unlike micelles, for which the 2-component model is used, vesicle bilayers are modeled by n Gaussian shells, with each of them representing a certain moiety of the bilayer [189, 205]. Hence the overall electron density profile is a summation of n Gaussian functions:

$$\rho(r) = \sum_{k=1}^n \rho_k \exp[-(r - \delta_k)^2 / (2\sigma_k^2)], \quad (4.13)$$

where δ_k is the distance between the Gaussian shell and the vesicle center, and σ_k is the width (standard deviation) of the Gaussian shell. With the EDP in hand, we now introduce the derivation of the form factor $F(q)$ for both the sphere model and flat bilayer model [204].

4.4.2 The form factor of spherical vesicles

The form factor of sphere structures can be derived from the radically-symmetric Fourier transform of Eq. 4.13 [204]:

$$F_s(q) = 2q^{-1} \sum_{k=i}^n \rho_k \sigma_k \exp(-q^2 \sigma_k^2 / 2) [\delta_k \sin(q\delta_k) + \sigma_k^2 q \cos(q\delta_k)]. \quad (4.14)$$

The term $\sigma_k^2 q \cos(q\delta_k)$ is relatively small and can thus be ignored. We then obtain

$$F_s(q) = 2q^{-1} \sum_{k=i}^n \rho_k \sigma_k \delta_k \exp(-q^2 \sigma_k^2 / 2) \sin(q\delta_k). \quad (4.15)$$

No orientational averaging is needed thanks to the spherical shape. Instead, we have to average $F_s(q)$ over vesicle radii R for a population of non-uniform vesicles. A Gaussian function with average radius R_0 and standard deviation σ_R can be introduced to describe the vesicle size distribution [204]. After a *normalized ensemble average* we finally obtain:

$$\langle F_s(q)^2 \rangle = q^{-2} \sum_{k,k'}^n (R_0 + \varepsilon_k)(R_0 + \varepsilon_{k'}) \rho_k \rho_{k'} \sigma_k \sigma_{k'} \exp[-q^2(\sigma_k^2 + \sigma_{k'}^2)/2] \times \cos[q(\varepsilon_k - \varepsilon_{k'})]. \quad (4.16)$$

Here δ is replaced by $R + \varepsilon$ where ε is the relative position of the Gaussian shell with respect to the bilayer center.

4.4.3 The form factor of bilayer-like vesicles

Vesicles that are large enough ($R > 25$ nm [206]) can be considered as flat bilayers when performing x-ray characterization. A simple 1d Fourier Transform of the EDP in Eq. 4.13 results in

$$F_f(q) = q^{-1} \sum_{k=i}^n \rho_k \sigma_k \exp(-q^2 \sigma_k^2 / 2) \exp(iq\delta_k). \quad (4.17)$$

No orientational averaging is needed if we assume that the vesicles are a “perfect powder”, i.e. bilayers have random orientation [204]. $\langle F_f(q)^2 \rangle$ can be directly calculated with $\langle F_f(q)^2 \rangle = F_f(q)F_f(q)^*$ and therefore,

$$\langle F_f(q)^2 \rangle = q^{-2} \sum_{k,k'}^n \rho_k \rho_{k'} \sigma_k \sigma_{k'} \exp[-q^2(\sigma_k^2 + \sigma_{k'}^2)/2] \times \cos[q(\varepsilon_k - \varepsilon_{k'})]. \quad (4.18)$$

Here δ is again replaced by ε , so that $d_{hh} = |\varepsilon_1 - \varepsilon_3|$.

From previous [172] and our own dynamic light scattering data (shown below in Fig. 4.17) we gain the knowledge that our vesicles are large enough ($R > 25$ nm [206]) so that the curvature effect can be ignored. As a result, both the sphere model and the flat bilayer model are well suited. As the sphere form factor F_s contains a lot more fitting parameters, we choose the simpler flat bilayer model to fit the scattering intensity I_f . A scaling factor s and a constant background f is added in the calculation, yielding

$$I_f = s \langle F_f(q)^2 \rangle + f. \quad (4.19)$$

Fitting is performed with the *lsqnonlin* function from the Optimization Toolbox in MATLAB (MathWorks Inc.). The goodness of fit is again evaluated by the the reduced χ^2 as introduced in Section 4.3.3. Appendix B.1 summarizes the preparation and fitting conditions of all vesicles investigated in this work, and Appendix B.3 shows the MATLAB script to calculate the scattering intensity.

4.4.4 SAXS fitting of pure lipid vesicles with the bilayer model

As we have discussed in great detail in Chap. 1, lipid compositions can largely influence bilayer properties. In this subsection, vesicles of various pure lipids are carefully investigated by SAXS. Some of them are lipid mixtures commonly used for vesicle preparation such as PC-PE-PS-Chol [172] and PC-PE-Chol-SM [79],

while the others are the “magic mixtures” candidates that we have characterized in Chap. 1. These include PC-PE, PC-PE-Chol and PC-PE-PIP₂, which are more suitable for multibilayer preparation. Although in this study only PC-PE 4:1 vesicles are utilized for multibilayer deposition, in the future others could also be potentially used to yield multibilayers with higher orientation and fusio-genicity.

PC-PE-Chol

Fig. 4.9 shows the SAXS curves of PC-PE-Chol vesicles prepared by (a) the column method, i.e. the co-micellization/size-exclusion routine and (b) the sonication method (See Chap. 3). The first impression we could obtain from the SAXS curves is that all vesicles possess a multibilayer structure, as indicated by the characteristic Bragg peaks [205]. This property might result from the lack of charged lipid in the current vesicle composition, such as PS, PG and PIP₂ [207]. Charged lipids are able to prevent bilayers from stacking onto each other due to the electrostatic effect.

Samples	d [Å] (column)	d [Å] (sonication)
PC-PE 1:1	54.87 ± 2.10	60.88 ± 1.90
PC-PE + 5% Chol	55.36 ± 1.11	61.18 ± 2.13
PC-PE + 10% Chol	57.96 ± 1.96	61.72 ± 1.44
PC-PE + 20% Chol	60.36 ± 2.30	63.21 ± 2.15
PC-PE-Chol-SM (Nat.'s Own)	-	66.03 ± 2.55

Table 4.3: *Bilayer periodicity d of PC-PE-Chol vesicles prepared by (left) column and (right) sonication. Additionally the d of the “nature’s own fusio-genic mixture” [79] vesicles prepared by sonication is also included. The standard deviations are show after \pm .*

We first compare the SAXS curves within each preparation. The SAXS curves appear similar to each other for vesicles prepared by the same method, despite the difference in Chol concentration. Chol might be able to incorporate themselves into the PC-PE 1:1 vesicles without leading to significant bilayer/vesicle modification. When we compare the SAXS curves between the two methods, distinct lineshapes can be observed. The PC-PE and PC-PE-Chol vesicles prepared by the column method seem to be highly multibilayer, with 2 Bragg orders appearing in the SAXS curves. In contrast, PC-PE and PC-PE-Chol vesicles prepared by the sonication method are close to unilamellar, with the Bragg peaks being considerably weak and hardly observable. The sonication process seems to supply external energy to destabilize the multibilayer structure [207].

The fitting of multibilayer vesicles involves rather complicated modeling and

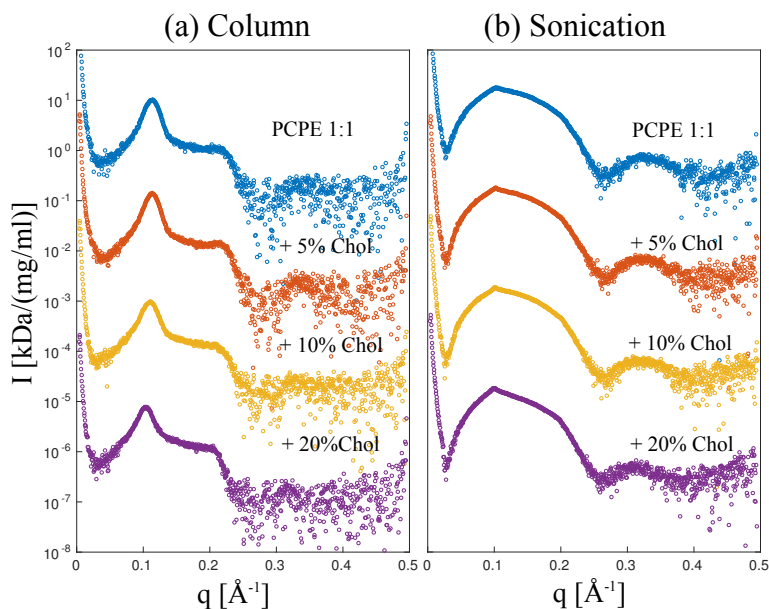


Figure 4.9: SAXS curves of PC-PE-Chol vesicle suspensions prepared by (a) the column method and (b) the sonication method. Curves are shifted for clarity and the lipid concentrations in the two series are ~ 4 and 5 mg/ml respectively. PC-PE molar ratio is kept at 1:1 with Chol concentration increasing from top to bottom. Pure H_2O is used for both samples (no buffer). Bragg peaks due to the multilamellar structure are observed for all vesicles suspensions.

requires relatively high data quality [205]. Therefore, we simply take a look at the bilayer periodicity d Tab. 4.3 instead, which can be easily calculated with the positions of the Bragg peaks without any model fitting. When Chol is added to PC-PE 1:1 vesicles, d increases continuously with Chol concentration, from 54.87 up to 60.34 Å for the column method, and from 60.88 up to 66.03 Å for the sonication method. Assuming that the bilayer thickness d_{hh} increases linearly with d under the same hydration condition [20], this result is well in line with the fact that Chol leads to an increase in d_{hh} [208]. Interestingly, PC-PE-Chol vesicles prepared by the sonication method have generally thicker bilayers compared by the column method. Since their lipid compositions and the sample environment (ultrapure H_2O) are the same, we assume that there is some n-OG remaining in the vesicles prepared by the column method. n-OG has a much short chain length and hence can largely reduce the bilayer thickness of long-chain lipids [209]. In our case the column method is capable of efficiently remove most n-OG during the fast preparation process, but fails to thoroughly remove it.

“Nature’s own fusigenic mixture” (PC-PE-Chol-SM)

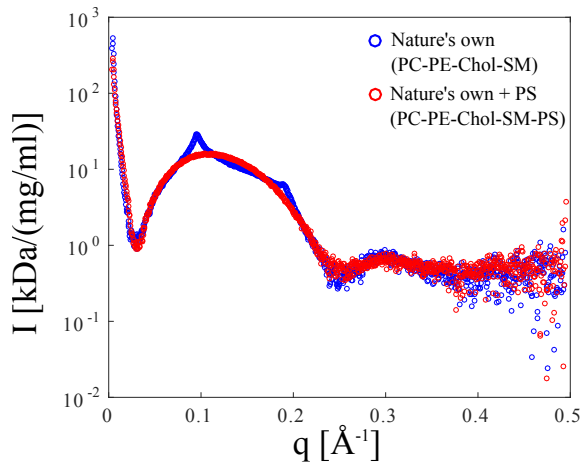


Figure 4.10: SAXS curves of “Nature’s own fusigenic mixture” (PC-PE-Chol-SM 35:30:15:20) and “Nature’s own fusigenic mixture” doped with 10% PS (PC-PE-Chol-SM-PS), prepared by sonication. For both samples only pure H₂O is used (no buffer). The lipid concentrations is 5 mg/ml and curves are vertically shifted for clarity.

As introduced in Chap. 1, the “nature’s own fusigenic mixture” (PC-PE-Chol-SM 35:30:15:20) has a lipid composition close to synaptic vesicle membrane and forms high fusigenic vesicles with low rupture rate [79]. In this section, firstly PC-PE-Chol-SM vesicles prepared by sonication were investigated by SAXS whose curve is shown in Fig. 4.10 (blue). The SAXS curve exhibits two clear Bragg peaks, in contrast to the only 1 Bragg order from PC-PE-Chol vesicles by sonication (Fig. 4.9b). We already know that Chol barely changes the vesicle structure of PC-PE 1:1, while it seems that SM largely strengthens the multibilayer structure possibly due to the coupling effect of SM and Chol. Tab. 4.3 shows that the d of PC-PE-Chol-SM is 66.03 Å, much larger than the PC-PE-Chol vesicles prepared by the same method (60.88-63.21 Å). This result is in good agreement with other experiments where SM strongly increased the bilayer thickness due to its high chain-ordering [210].

Along with PC, PE, Chol and SM, PS is also an essential lipid type in synaptic vesicles. Therefore, it would be meaningful to add PS into the “Nature’s own fusigenic mixture” to make it complete. In this study, 10% PS was thus mixed with PC-PE-Chol-SM to form vesicles with a lipid composition even closer to the synaptic vesicle membrane.

Fig. 4.10 shows the SAXS curve (red) of PC-PE-Chol-SM-PS vesicle suspension, which demonstrates a typical unilamellar SAXS lineshape. When comparing it with the SAXS curve of PC-PE-Chol-PS (blue), the most significant difference is the disappearance of the Bragg peaks. It is interesting to gain the knowledge that 10% PS could already effectively prevent multilayer formation in the sonication preparation. This finding is also in line with the fact that synaptic vesicles only exhibit unilamellar structures in nature. The two SAXS curves almost overlap with each other except for the Bragg peak region, indicating a similar bilayer structure despite different stacking geometries.

PC-PE-PIP₂ and its reaction to salt

PIP₂ is a negatively charged lipid with a massive headgroup, one saturated and one unsaturated acyl chain. During synaptic vesicle fusion, it can bind to synaptotagmin and accelerate its response to Ca²⁺ [43]. Here PIP₂ was incorporated into PC-PE 1:1 to facilitate unilamellar PC-PE-PIP₂ vesicles via sonication. Vesicles of pure PC-PE 1:1 were also prepared by sonication to serve as the control sample. Due to the fact that PC-PE 1:1 vesicles typically show multilamellar structures (see Fig. 4.9), subsequent extrusion [127] (50 nm pore size) was carried out to yield unilamellar PC-PE 1:1 vesicles for better comparison.

Their SAXS curves are plotted in Fig. 4.11 (colored). We first try to use the symmetric flat bilayer model to fit these curves. The fitting curves are shown by Fig. 4.11 (black), and the fitting results are summarized in Tab. 4.4. By comparing the SAXS and fitting curves, it is obvious that the symmetric flat bilayer model well fits the PC-PE 1:1 curve in the entire q range and the PC-PE-PIP₂ curves in the high q regime ($q > 0.09 \text{ \AA}^{-1}$), but not PC-PE-PIP₂ curves in the low q regime ($q < 0.09 \text{ \AA}^{-1}$). Moreover, the bilayer thickness d_{hh} , the most important fitting parameter, seems to stay constant despite the increase of the PIP₂ concentration. However, our previous study [20] reveals that the addition of PIP₂ increases the d_{hh} of DOPC bilayers continuously. Therefore, despite that all EDPs show the typical bilayer lineshape, the SAXS curves of PC-PE-PIP₂ can not be properly fitted by the symmetric flat bilayer model. We thus turn to the asymmetric flat bilayer model.

Fig. 4.12 shows the SAXS curves of PC-PE-PIP₂ (colored) and the fitting curves of the asymmetric flat bilayer model (black). Note that The PC-PE 1:1 curve is still fitted with the symmetric model because above we have already proven it to be suitable for this particular sample. The fitting parameters are summarized in Tab. 4.5. It is apparent that the asymmetric flat bilayer model fits the PC-PE-

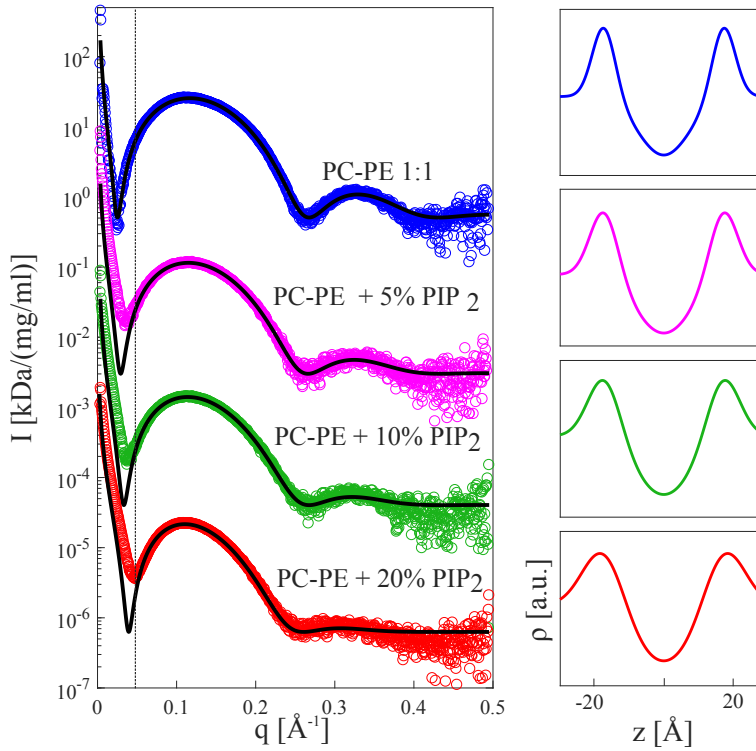


Figure 4.11: (left) SAXS curves (colored) and fitting curves (black) of PC-PE 1:1 vesicles doped with PIP₂ prepared by sonication. For all samples only pure H₂O is used (no buffer). The lipid concentration is 5 mg/ml and curves are vertically shifted for clarity. The symmetric flat bilayer model with a constant background f is used to fit all curves. Only the data in the q range of 0.050-0.495 \AA^{-1} is fitted, as indicated by the dashed line. (right) EDPs (arbitrary units) derived from the fitting results of the SAXS curves.

Samples	$\varepsilon_1[\text{\AA}]$	$\rho_1[\text{a.u.}]$	$\sigma_1[\text{\AA}]$	$\sigma_2[\text{\AA}]$	$d_{hh}[\text{\AA}]$	s	f	χ^2_{red}
PC-PE 1:1	-18.18±0.39	1.24±0.12	3.48±0.04	7.91±0.33	36.36	0.08	0.51	3.90
PC-PE + 5% PIP ₂	-18.10±0.39	1.17±0.11	4.27±0.05	8.88±0.35	36.20	0.05	0.42	0.95
PC-PE +10% PIP ₂	-18.00±0.38	1.09±0.11	4.95±0.06	9.21±0.36	36.00	0.05	0.48	1.31
PC-PE +20% PIP ₂	-18.11±0.39	1.20±0.12	6.38±0.09	12.41±0.39	36.22	0.05	0.62	1.90

Table 4.4: Fitting results of PC-PE 1:1 vesicles doped with PIP₂ prepared by sonication, using the symmetric flat bilayer model with a constant background f . The bilayer thickness d_{hh} is calculated with the positions of the first and last Gaussian shell ε_1 and ε_3 . The values after \pm are the standard deviations.

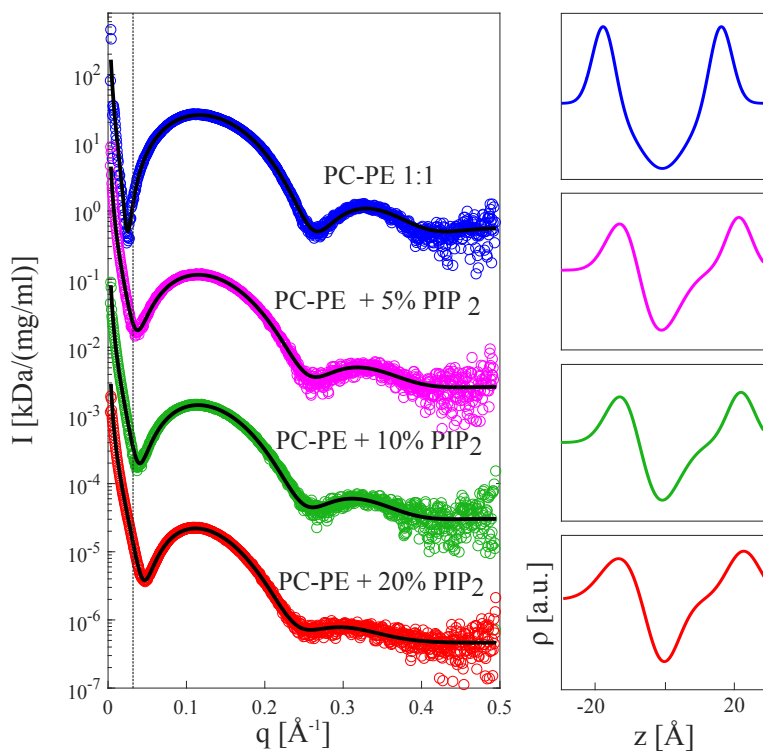


Figure 4.12: (left) SAXS curves (colored) and fitting curves (black) of PC-PE 1:1 vesicles doped with PIP_2 prepared by sonication. For all samples only pure H_2O is used (no buffer). The lipid concentration is 5 mg/ml and curves are vertically shifted for clarity. The symmetric flat bilayer model is used for PC-PE 1:1 and the asymmetric flat bilayer model is used for the others, both with a constant background f . Only the data in the q range of 0.030 - 0.495 \AA^{-1} is fitted, as indicated by the dashed line. (right) EDPs (arbitrary units) derived from the fitting results of the SAXS curves.

Samples	$\varepsilon_1[\text{\AA}]$	$\varepsilon_3[\text{\AA}]$	$\rho_1[\text{a.u.}]$	$\rho_3[\text{a.u.}]$	$\sigma_1[\text{\AA}]$	$\sigma_2[\text{\AA}]$	$\sigma_3[\text{\AA}]$	$d_{hh}[\text{\AA}]$	s	f	χ^2_{red}
PC-PE 1:1	-18.19 ± 0.39	18.19 ± 0.31	1.25 ± 0.07	1.25 ± 0.14	3.48 ± 0.04	7.91 ± 0.33	3.48 ± 0.04	36.37	0.08	0.50	3.75
PC-PE + 5% PIP_2	-10.06 ± 1.12	25.35 ± 0.45	1.00 ± 0.07	0.81 ± 0.02	4.91 ± 0.09	6.81 ± 0.52	4.01 ± 0.15	35.24	0.08	0.36	1.42
PC-PE + 10% PIP_2	-9.79 ± 2.68	26.26 ± 0.99	1.01 ± 0.14	0.77 ± 0.02	5.22 ± 0.34	6.85 ± 1.13	4.21 ± 0.26	35.63	0.10	0.36	2.62
PC-PE + 20% PIP_2	-12.59 ± 0.48	25.33 ± 0.14	0.64 ± 0.00	0.71 ± 0.01	6.48 ± 0.23	5.11 ± 0.14	5.19 ± 0.00	37.92	0.10	0.46	1.47

Table 4.5: Fitting results of PC-PE 1:1 vesicles doped with PIP_2 prepared by sonication. The symmetric flat bilayer model is used for PC-PE 1:1 and the asymmetric flat bilayer model is used for the others, both with a constant background f . The bilayer thickness d_{hh} is calculated with the positions of the first and last Gaussian shell ε_1 and ε_3 . The values after \pm are the standard deviations.

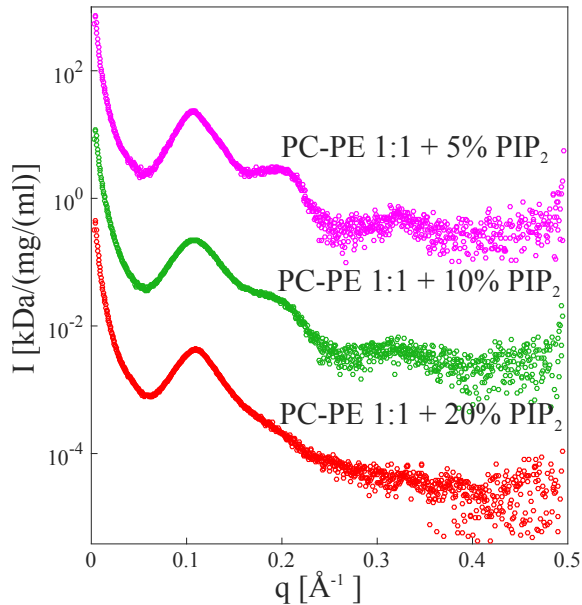


Figure 4.13: SAXS curves of PC-PE-PIP₂ vesicles in 2.5 mM CaCl₂ solution. The lipid concentration is 5 mg/ml. All curves show typical multilamellar lineshape with the bilayer periodicity $d \approx 59.28$ Å. Curves are vertically shifted for clarity.

PIP₂ curves much better than the symmetric model. Both in the low and high q regime, the fitting curves highly match the experimental curves. Moreover, d_{hh} exhibits a continuous increase with the PIP₂ concentration except for the PC-PE 1:1 vesicle, well in line with our previous observation [20]. We can therefore reasonably assume that the PC-PE-PIP₂ bilayers bear certain degrees of asymmetry. This assumption is confirmed by the weakening of the maxima and minima upon the addition of PIP₂, which has been reported to be possibly caused by membrane asymmetry [204]. Such an asymmetric distribution of PIP₂ also agrees with the fact that in *in vivo* PIP₂ largely exists in the cytoplasmic (inner) leaflet [211]. Such an asymmetry in *in vitro* in the absence of cations and proteins perhaps originate from its multivalence [212] (a net charge of -3 at neutral pH [213]).

For PC-PE-PIP₂ vesicles in ultrapure water, a unilamellar structure is always obtained due to the high number of charges in PIP₂. CaCl₂ was then added into the existing PC-PE-PIP₂ vesicle suspensions, arriving at a final CaCl₂ concentration of 2.5 mM. The suspensions were then immediately characterized by SAXS, whose results are shown in Fig. 4.13. For all PIP₂ concentrations, the unilamel-

lar structures transform into multilamellar as indicated by the characteristic Bragg peaks. It is indeed an interesting finding that the addition of CaCl_2 can eliminate PIP_2 's effect on the formation of unilamellar vesicles, which is in line with the fact that Ca^{2+} can bind to negatively charged lipids and screen their electrostatic effects [214]. When more PIP_2 is present, this screening effect is less significant and the multilamellar order is lower, as indicated by the diminishing of the 2^{nd} Bragg peak. In the future this phenomena could be further investigated, possibly with respect to salt concentration and salt penetration into vesicle interiors.

4.4.5 SAXS fitting of proteoliposomes with the bilayer model

More importantly for the establishment of the novel sVS protocol, proteoliposomes composed of PC-PE-PS-Chol 5:2:2:1 or PC-PE 4:1 prepared via the comicellization/size-exclusion routine (i.e. the column method) are also investigated by SAXS.

PC-PE 4:1

We have learned from the last section that PC-PE forms highly multilamellar vesicles in pure H_2O , especially when no sonication is performed. In this section, the PC-PE 4:1 vesicles were reconstituted with SNAREs and evaluated by SAXS.

Fig. 4.14 shows the SAXS curves of pure PC-PE 4:1 vesicle suspension (blue), (ii) PC-PE/ ΔN proteoliposome suspension (red), (iii) PC-PE/Syb proteoliposome suspension (green) and (iii) PC-PE/ ΔN +Syb proteoliposome suspension (purple), prepared by the column method. Bragg peaks are found in all SAXS curves indicating multibilayer structures, due to the lack of charged lipids. A noticeable feature of the SAXS curve of ΔN containing vesicles is the strong intensity in the low q region. This has occurred in the micelle SAXS section and can be attributed to the aggregation as we demonstrate below. Moreover, the SAXS curve of proteoliposome suspensions containing both ΔN and Syb appears to be a simple average of the SAXS curves of unmixed ΔN and Syb proteoliposome suspensions. This indicates that fusion events did not take place in large quantity during the short time (\sim a few minutes) after mixing.

The bilayer periodicity d of pure PC-PE (59.84 Å) is slightly smaller than the ones containing SNAREs, with $d = 63.53$ Å for ΔN , 60.00 Å for Syb and 60.64 Å

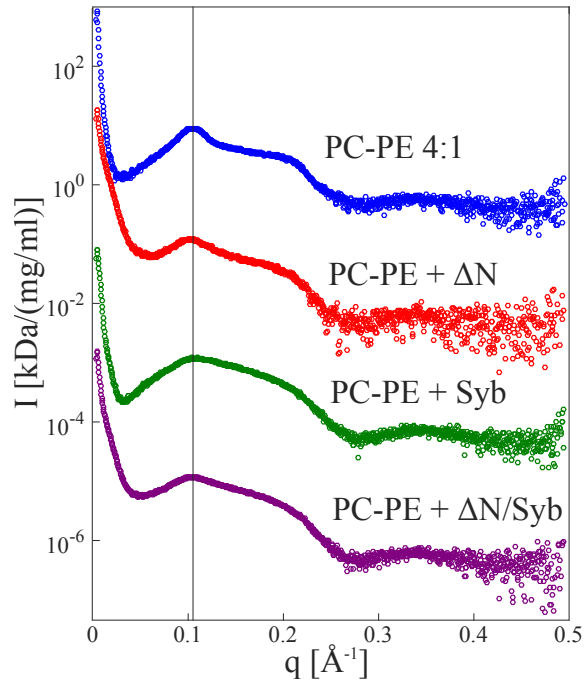


Figure 4.14: SAXS curves of SNARE-reconstituted PC-PE 4:1 vesicles prepared by the column method. Only pure H_2O is used (no buffer). The lipid concentration ≈ 7 mg/ml and the protein/lipid ratio $\approx 1:500$. Some curves are vertically shifted for clarity. All curves show the typical multilamellar lineshape with the bilayer periodicity $d \approx 59.84\text{-}63.53$ Å. The position of the first Bragg peak is marked by the vertical line across all curves.

for the mixture of ΔN and Syb. First of all, this result perfectly agrees with our observation in the micelle section that SNAREs slightly enlarge the micelles, with ΔN brings about more profound modification than Syb. The d of mixed suspensions falls in between the d of unmixed suspensions, again indicating a lack of fusion events. We then performed 30 min incubation at room temperature on the mixed suspensions to inspect whether sufficient fusion events could occur to introduce significant structural alteration.

Fig. 4.15 shows the SAXS curves on the mixed proteoliposome suspensions before (0 min) and after incubation (30 min). It is obvious that two SAXS curves largely overlap with each other. Although currently no fitting has been performed due to the complexity of multilamellar vesicle fitting, we could still deduce from the lineshapes that 30 min of incubation at room temperature did not bring them into fusion on a large scale. One possible reason for this is the

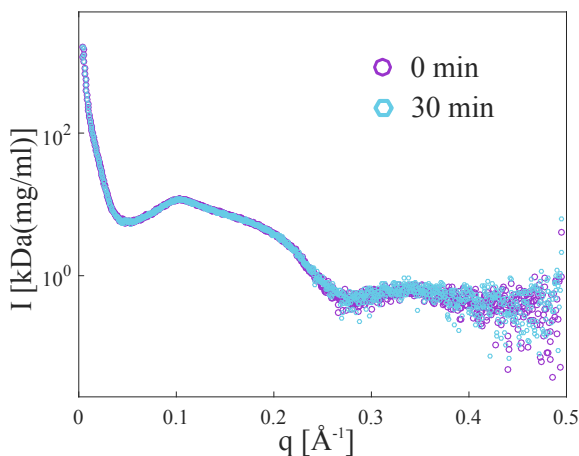


Figure 4.15: SAXS curves of PC-PE 4:1 vesicles containing both ΔN and Syb before and after incubation. The first curve was obtained right after mixing the two proteoliposome suspensions (0 min) while the second curve was obtained 30 min after mixing. The two curves highly overlap with each other.

Samples	$ \varepsilon_1 $ [Å]	σ_1 [Å]	σ_2 [Å]	ρ_1 [a.u.]	d_{hh} [Å]	s	f	χ^2_{red}
PC-PE-PS-Chol by Soni.	18.76 ± 0.27	6.52 ± 0.32	11.28 ± 1.05	1.03 ± 0.03	37.52 ± 0.54	0.0623	0.4843	1.51
PC-PE-PS-Chol	18.04 ± 0.25	5.22 ± 0.36	10.50 ± 0.94	1.09 ± 0.03	36.08 ± 0.50	0.0580	0.6675	1.46
PC-PE-PS-Chol/ ΔN	19.14 ± 0.18	4.21 ± 0.17	10.05 ± 0.94	1.09 ± 0.02	38.28 ± 0.36	0.0777	0.8452	1.50
PC-PE-PS-Chol/Syb	18.38 ± 0.19	5.51 ± 0.32	10.19 ± 0.66	1.05 ± 0.02	36.76 ± 0.38	0.0646	0.7429	1.41
PC-PE-PS-Chol/ ΔN +Syb	18.93 ± 0.12	4.60 ± 0.14	9.64 ± 0.75	1.08 ± 0.02	37.86 ± 0.24	0.0763	0.8131	1.21

Table 4.6: Fitting results of the SAXS data of (i) pure PC-PE-PS-Chol 5:2:2:1 suspension prepared by sonication (Soni.), (ii) pure PC-PE-PS-Chol, (iii) PC-PE-PS-Chol/ ΔN , (iv) PC-PE-PS-Chol/Syb and (v) PC-PE-PS-Chol/ ΔN +Syb vesicle suspensions prepared by the column method. The values after \pm are the standard deviations. The bilayer thickness d_{hh} is calculated with $d_{hh} = 2|\varepsilon_1|$.

lack of salt in ultrapure water. In fusion assays, vesicle suspensions usually contain “fusion buffer” in order to promote rapid fusion [215].

PC-PE-PS-Chol 5:2:2:1

A lipid composition more suitable for unilamellar vesicle preparation, PC-PE-PS-Chol 5:2:2:1 is applied to the SNARE proteoliposomes as well. Besides the PC-PE-PS-Chol 5:2:2:1 vesicles prepared via the column method, pure PC-PE-PS-Chol vesicles were also prepared by sonication to serve as a detergent-free control sample.

Fig. 4.16a shows the SAXS curves (colored circles) and the fits (black lines) of (i)

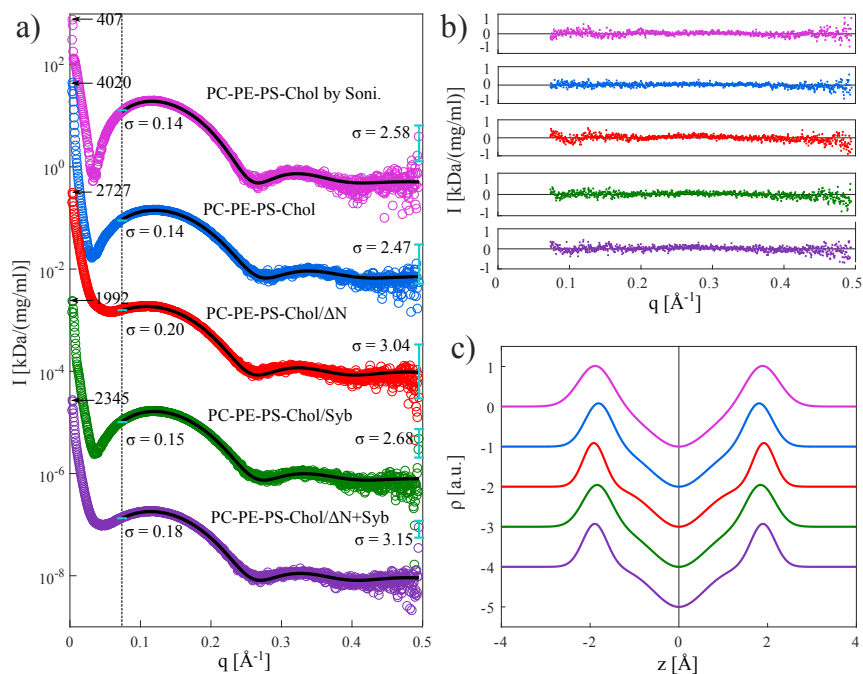


Figure 4.16: (a) SAXS curves (colored circles) and their fits (black lines) of (i) PC-PE-PS-Chol vesicles prepared by sonication, (ii) PC-PE-PS-Chol, (iii) PC-PE-PS-Chol/ Δ N, (iv) PC-PE-PS-Chol/Syb and (v) PC-PE-PS-Chol/ Δ N+Syb vesicles prepared by size-exclusion. Both are plotted on a logarithmic scale and shifted for clarity. The mass concentration of the lipid is ~ 7 mg/ml. Data in the q range of 0.075 - 0.495 \AA^{-1} is fitted, as indicated by the vertical dashed line. The intensities of $q \rightarrow 0$ are again marked by arrows. The experimental errors of the first and last fitted data points are plotted in cyan. (b) Corresponding residuals of the fits to the symmetric flat-bilayer model. (c) Electron density profiles reconstructed with the obtained fitting parameters in Tab. 1b.

PC-PE-PS-Chol vesicles prepared by sonication, (ii) PC-PE-PS-Chol, (iii) PC-PE-PS-Chol/ Δ N, (iv) PC-PE-PS-Chol/Syb and (v) PC-PE-PS-Chol/ Δ N+Syb vesicles prepared by size-exclusion. Firstly all SAXS curves displays the typical unilamellar lineshape. The third maxima appear in all SAXS curves due to the relatively high lipid concentration (5 mg/ml for (i) and 7 mg/ml for the others), while the previously measured 1 mg/ml vesicles suspensions of the same type provided only 2 maxima (data not shown). Unlike in Section 4.3.4, where the intensity of the Δ N-containing proteomicelles clearly indicates strong aggregation, here the scattering intensity of the Δ N-containing proteoliposomes does not stand out from the crowd. We will look further into this effect by dynamic light scattering in the coming section. Lastly, the SAXS curve of the mixed suspension of PC-PE-PS-Chol/ Δ N and PC-PE-PS-Chol/Syb is also an average of the curves of

the unmixed ones, the same as the PC-PE 4-1 proteoliposomes. No other dissimilarities are found between curves from visual comparison.

The fitting results are summarized in Tab. 4.6. They show that bilayer thicknesses d_{hh} of the investigated vesicles vary considerably with the preparation methods and the compositions. Firstly the bilayer of pure PC-PE-PS-Chol vesicle prepared by sonication ($d_{hh} = 37.52 \text{ \AA}$) is thicker than the one prepared by size-exclusion ($d_{hh} = 36.08 \text{ \AA}$). As they have the same lipid composition, the only appropriate explanation is that there was fairly abundant detergent (mainly n-OG) left in the bilayers, which inserted into the lipid bilayers in a wedge-like fashion [216] and lead to bilayer thinning [209]. Secondly for sVS vesicles of PC-PE-PS-Chol/ ΔN ($d_{hh} = 38.28 \text{ \AA}$) and PC-PE-PS-Chol/Syb ($d_{hh} = 36.76 \text{ \AA}$), d_{hh} is increased with respect to PC-PE-PS-Chol (protein-free control). This is somewhat similar to the observed swelling of micelles discussed above. In contrast to the micelles, however, the protein copy number of a vesicle is much larger than one, in fact for 100% reconstitution efficiency we expect 44 proteins for a $R = 30 \text{ nm}$ vesicle (see Appendix C.2). Given the still low protein-to-lipid ratio $P/L = 0.002$, we cannot expect however to see a large contribution of the “protein shell” around the bilayer. For this reason, it is plausible that the electron densities reflect mainly the small changes which the protein reconstitution brings to the lipid matrix, i.e. proteins are sensed only indirectly at this P/L . For comparison, Fig. 4.16c shows the electron density profiles (EDPs) of all 5 types of vesicle bilayers reconstructed with the fitting parameters in Tab. 4.6. They show that the bilayer structure is not significantly altered by SNARE reconstitution, apart from the minor membrane thickening. Lastly, almost all fitting parameters of the mixed vesicles (PC-PE-PS-Chol/ ΔN +Syb) are approximately the average of the non-mixed ones. It is likely that full fusion brings about no observable changes to the SAXS results, as long as the flat bilayer model is used to describe the data, i.e. as long as we are insensitive to the vesicle radius. However, we should be able to detect characteristic signals from docking and hemifusion. Since the SAXS curve of the mixed SNARE vesicles (purple) is roughly the average of the curves of single SNARE vesicles (red and green), we cannot identify any such effect.

4.4.6 Dynamic light scattering investigation of PC-PE-PS-Chol/SNARE proteoliposomes

From the micelle SAXS results we have deduced that the ΔN proteomicelles undergo strong aggregation. One could then reasonably suspect that the ΔN -

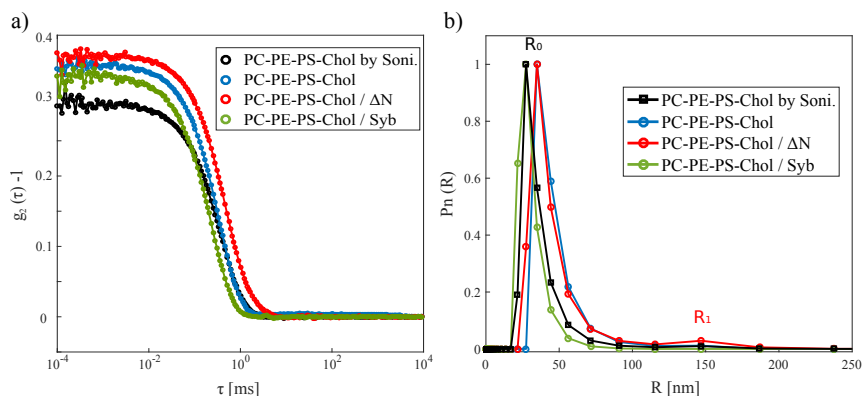


Figure 4.17: (a) DLS correlation curves and (b) size distributions of proteoliposomes of (i) pure PC-PE-PS-Chol prepared by sonication, (ii) pure PC-PE-PS-Chol, (iii) PC-PE-PS-Chol/ Δ N and (iv) PC-PE-PS-Chol/Syb prepared by the column method. Proteoliposome suspensions were diluted to 0.01 mg/ml and no buffer was added (pure H_2O only). Measurements were performed on ALV/CGS-3 laser light scattering goniometer system (ALG-GmbH, Langen, Germany), equipped with a 22 mW HeNe laser ($\lambda = 632.8$ nm) at 90° scattering angle. All vesicles share a radius $R_0 \approx 30$ nm, with Δ N showing a unique $R_1 \approx 150$ nm.

containing proteoliposomes might inherit this effect, which is not clearly shown by the vesicle SAXS data in Fig 4.16a. In this section, dynamic light scattering (DLS) is employed to further investigate the size distribution of these vesicles. Additionally, this technique can also quantitatively reveal vesicle populations when the proper weighting method is applied [217].

Fig. 4.17 shows the correlation curves and particle-size distributions of pure PC-PE-PS-Chol vesicles and PC-PE-PS-Chol/SNARE proteoliposomes, including (i) pure PC-PE-PS-Chol vesicles prepared by sonication, (ii) pure PC-PE-PS-Chol vesicles, (iii) PC-PE-PS-Chol/ Δ N proteoliposomes and (iv) PC-PE-PS-Chol/Syb proteoliposomes prepared by the column (size-exclusion) method. The experimental auto-correlation functions (Fig. 4.17a) are fitted by logarithmic number-weighted algorithm to yield the size distribution functions (Fig. 4.17b). All vesicles share a mean radius $R_0 \approx 30$ nm with small peak width. It is rather surprising to find that the vesicles prepared by column and sonication exhibit similar size distributions. The shared mean radius R_0 indicates comparable vesicle sizes, and the small peak width indicates considerable monodispersity resulting from both methods. In addition, proteoliposomes prepared by the column method generally exhibit size distributions similar to pure lipid vesicles by the same method, confirming that SNARE reconstitution barely al-

ters vesicle structures. The only difference is the unique mean radius $R_0 \approx 150$ nm found in the size-distribution function of PC-PE-PS-Chol/ Δ N. This result on the one hand verifies our suspect that the Δ N-containing proteoliposomes inherit the aggregation from the Δ N-containing proteomicelles on the other hand demonstrates that the majority of vesicles is however in an unaggregated fraction with radii in the expected size range around $R_0 \approx 30$ nm. In other words, despite a small degree of vesicle aggregation, most Δ N-containing proteomicelles remains mono-disperse. Therefore, we can nevertheless progress to Stage 3 of the sVS protocol (multibilayer) with the resulted proteoliposomes.

4.5 Summary and outlook

In this chapter, proteomicelles, pure lipid vesicles and proteoliposomes have been investigated by solution SAXS, with the data being fitted by appropriate models. We find out that (i) SNAREs are successfully reconstituted into both micelles and vesicles, leading to minor thickening effect without vastly changing their original structures; (ii) non-charged lipid mixtures exhibit multilamellar structures while charged ones formed unilamellar vesicles via co-micellization and size-exclusion; (iii) Chol, PIP₂ and SM (Nature's Own Lipid Mixture) are incorporated into PC-PE vesicles, resulting in an expected thickening effect on the bilayers; (iv) compared with the column method, sonication yields vesicles with lower multilamellar fraction, which could be further reduced by extrusion; (v) a small proportion of the Δ N-containing proteoliposomes aggregate, resulting in; while the majority of them remain mono-disperse; (vi) no coupling effect of Δ N and Syb can be detected even after 30 min of incubation.

SAXS results of SNARE-reconstituted micelles and vesicles together support a simple picture of protein reconstitution. The SNAREs anchor themselves into the host aggregates via the TMDs, leading to minor structural modifications in the detergent and lipid assembly. These findings provide adequate information both for the current protocol and for future refinement. More importantly, they validate the sVS preparation in Stage 1 and 2, which is a prerequisite for the following deposition of multibilayers (Stage 3).

5 X-ray characterizations of SNARE-reconstituted multibilayers

Part of this chapter is based on the manuscript: Y. Xu, J. Kuhlmann, M. Brennich, K. Komorowski, R. Jahn, C. Steinem and T. Salditt. Reconstitution of SNARE proteins into solid-supported lipid bilayer stacks and x-ray structure analysis. BBA-Biomembranes (submitted)

Having determined structures of the proteomicelles and proteoliposomes (Stage 1 and 2 of the sVS protocol, Fig. 3.6), we now proceed to the characterization of sVS multibilayers (Stage 3 of the sVS protocol), with the ultimate goal of 3d EDP reconstitution of the stalk structure in the presence of SNARE complexes ahead. In this chapter, multibilayers containing SNAREs are studied by x-ray reflectivity and grazing-incidence small-angle x-ray scattering (GISAXS). This chapter starts with the preliminary results of the GISAXS investigation on SNARE-containing multibilayers at ID01, ESRF. It is followed by the results of systematic in-house investigation of x-ray reflectivity and GISAXS. PC-PE mixtures are selected as the main lipid composition for multibilayer preparation in this work based on our previous finding that it is able to form highly aligned bilayer stack with rhombohedral phases forming at relatively high RHs (low osmotic pressure) [21, 25].

5.1 GISAXS characterizations of SNARE-reconstituted multibilayers at ID01

In the early stage of the development of the sVS method, SNAREs were reconstituted into both PC-PE and PC-PE-PS-Chol multibilayers always in an mixed fashion, aiming at stalk formation in the presence of coupled SNARE complexes.

5.1.1 Beamline setup

The ID01 undulator beamline has already been introduced in Chap. 1 and 2. Briefly, multibilayers were mounted in the software-controlled humidity cham-

ber, positioned on the sample tower of the 6-axis goniometer. The 17.91 keV monochromatic beam was focused by a set of beamline optics to $160 \times 20 \mu\text{m}^2$ on the sample and detected by a Medipix TAA22PC pixel detector mounted 178.59 mm away from the sample. Each exposure was recorded for 10 s using a 200 μm thick Mo attenuator. The incident angle θ was carefully chosen so that the specular beam resided between the primary beam and the first Bragg peak. A rectangular beamstop was mounted right in front of the detector to further attenuate the primary beam and specular beam. For chain-correlation characterization, the detector was moved 12 mm and 6 mm in the y and z directions off the central position to capture the chain-correlation peaks. No Mo attenuator was used due to the low intensity of the chain-correlation peaks.

5.1.2 PC-PE-PS-Chol 5:2:2:1

Fig. 5.1 shows the GISAXS patterns of PC-PE-PS-Chol 5:2:2:1 multibilayers recorded at ID01 at RH 90% and 50%. (left) Pure PC-PE-PS-Chol prepared by sOS, (center) pure PC-PE-PS-Chol prepared by sVS, and (right) PC-PE-PS-Chol/ $\Delta\text{N}+\text{Syb}$ prepared by sVS. Images were recorded at a number of hydration conditions. Fig. 5.1 shows the ones recorded at RH 90% and 50%. At RH 90%, all multibilayers exhibit typical diffraction patterns of oriented lamellar phases, with more Bragg orders observed from the sOS multibilayer than from the sVS multibilayers (6 vs 4). First of all at higher hydration condition the multibilayers prepared by sVS also show high lamellar ordering, as indicated by the Bragg peaks. This property may yield high-resolution data for structural determination, phase identification, and eventually 2d or even 3d EDP reconstruction. Secondly, the sVS multibilayers show lower lamellar ordering compared with the sOS method at the same lipid composition. In the sOS preparation, lipid molecules move freely in organic solutions so that bilayers could find lower energy mesoscopic states more easily, hence higher lamellar ordering. Contrarily, in the sVS method lipid bilayers are deposited onto the wafers via vesicle adsorption and rupture. Inevitably, there can be a certain number of incomplete ruptures and more bilayer defects [179], hence lower lamellar ordering.

At RH 50%, the sOS multibilayer transformed to the rhombohedral (*R*) phase, which have been observed in many other sOS multibilayers [19, 25, 33]. Additionally, a new lamellar (*L*) phase appears perhaps due to the complex lipid composition. For sVS multibilayer however, the new *L* phase is found to be in coexistence with an inverted hexagonal (H_{II}) phase, instead of the expected *R* phase. It seems that under low hydration conditions, the sVS multibilayers

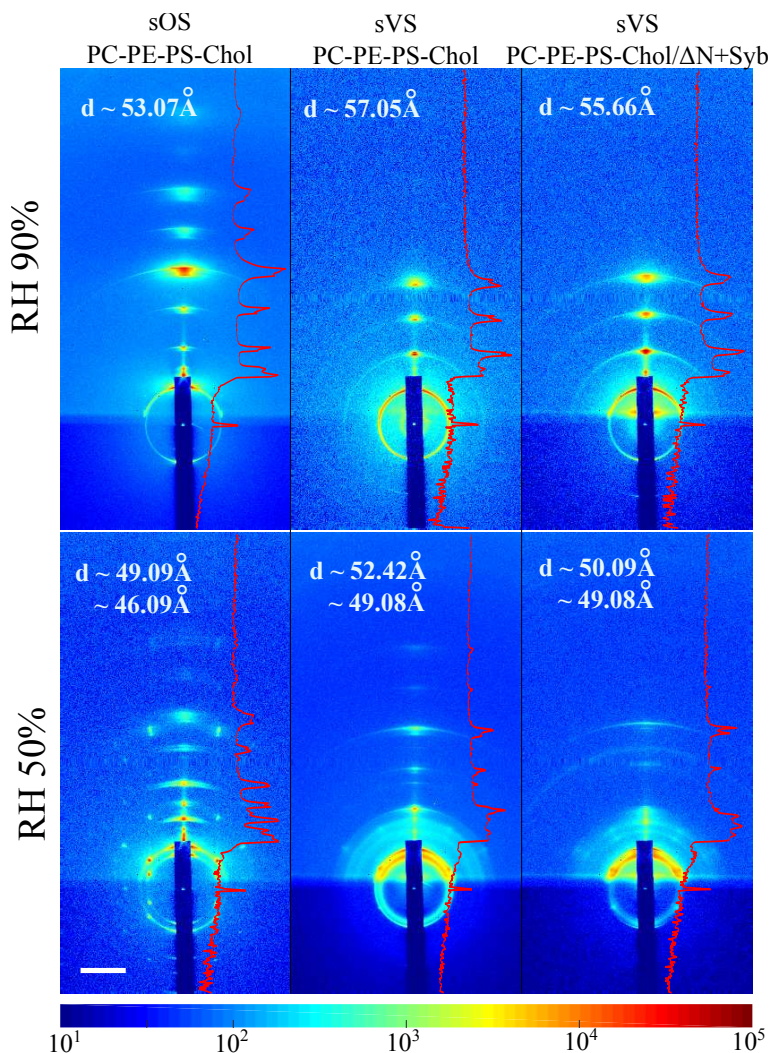


Figure 5.1: GISAXS patterns of multibilayers of (left) pure PC-PE-PS-Chol 5:2:2:1 prepared by sOS, (center) pure PC-PE-PS-Chol 5:2:2:1 prepared by sVS, and (right) PC-PE-PS-Chol 5:2:2:1 reconstituted with ΔN and Syb by sVS, measured at RH 90% and 50%. The dark blue bar is the shadow of the rectangular beamstop. All images were recorded with 10 s exposure time with the specular beam lying between the primary beam and 1st Bragg peak behind the beamstop. The intensity profiles along the $q_{\parallel} = 0$ direction are plotted in red. The d values in the images represent the bilayer periodicities, and the white scale bar in the lower left corner indicates 50 pixels on the detector. The false color scale corresponds to the logarithmic scattering intensity.

of PC-PE-PS-Chol do not form stalk structures. It is of course not a desired result, which shall be further verified on other lipid compositions such as PC-PE (see the next section). Concerning the sVS multibilayers with/without SNAREs, no significant differences can be seen. This result is in good agreement with our observations from proteomicelles and proteoliposomes in the last chapter that SNAREs only slightly modified the host aggregates. Another interestingly outcome is that the bilayer periodicity d of sVS is always larger than d of sOS, whereas SNARE reconstitution slightly reduces it. However, these d values may contain high experimental errors due to large peak width in GISAXS studies. For more precise d results reflectivity investigation with sharp specular peaks shall be performed.

Alkyl chain correlation (CC) measurement is a powerful tool to reveal the lateral order of lipids within membranes [18, 64, 139]. Fig. 5.2 shows the CC results and the fitting of the three PC-PE-PS-Chol multibilayers. Fig. 5.2a displays the diffraction patterns of the same PC-PE-PS-Chol multibilayers as above but measured in the q regime of CC peaks. A strong CC peak appears in the diffraction pattern of sOS multibilayer of pure PC-PE-PS-Chol, showing a typical peak shape of multibilayers with high chain-ordering [64, 139]. In contrast, the multibilayers of sVS with and without SNAREs both exhibit non-typical CC peaks, which are much weaker and almost angular independent compared to the peak of the sOS multibilayer. The intensity profiles at various angles ϕ (as shown in Fig. 5.2a, left) are extracted from the diffraction maps. These profiles are then fitted in the same way as in Chap. 2 by

$$f(q) = I_0 \frac{\omega^2}{(q - q_0)^2 + \omega^2} + mq + b, \quad (5.1)$$

where ω is the half width maximum, q_0 is the peak center, I_0 is the maximum of the Lorentzian which is normalized to 1 at $\phi = 10^\circ$, m the slope of the linear background, and b the constant offset [64, 139]. The average chain-chain distance a is then derived from $a \simeq \frac{9\pi}{4q_0} - \frac{3\omega}{2q_0^2}$ and the correlation length ξ of the acyl chains from $\xi = \frac{1}{\omega}$. The intensity profiles between 10° and 50° are available in this experiment. Every 5° an intensity profile is extracted and fitted by Eq. 5.1. Fig. 5.2b shows the intensity profiles and fitting curves of the sOS multibilayer to offer an example of the fitting process.

Fig. 5.2c plots resulting fitting parameters I_0 , a and ξ with respect to ϕ . Firstly the main chain-tilting angle can then be deduced from the maxima of I_0 [64, 139]. The maxima of all I_0 do not appear in the fitted ϕ range, meaning that all main chain-tilting angles are smaller than 10° . In other words the ma-

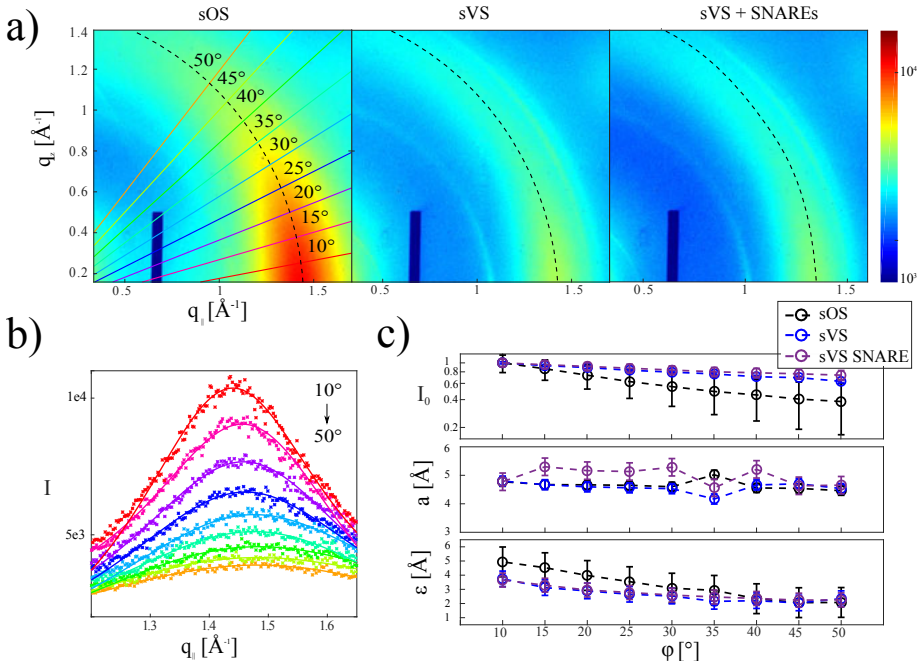


Figure 5.2: (a) GISAXS patterns of pure PC-PE-PS-Chol 5:2:2:1 multibilayers plotted measured in the chain-correlation q regime. (Left) pure PC-PE-PS-Chol prepared by sOS, (center) pure PC-PE-PS-Chol prepared by sVS and (right) PC-PE-PS-Chol reconstituted with ΔN and Syb by sVS. The dashed lines denote I_0 . In the left image, each colored line represents the intensity profile at each ϕ angle. All images were recorded with 10 s exposure time. The false color scale corresponds to the logarithmic scattering intensity and the dark blue bar results from the beamstop.

(b) Experimental data (stars) and fits (solid lines) of the pure PC-PE-PS-Chol by sVS, shown as an example of the fitting process.

(c) Lateral ordering parameters of the multibilayers derived from the fitting. The maximum of the Lorentzian I_0 (log scale), chain-chain distance a , correlation length ξ and their standard deviations are plotted as a function of ϕ .

majority of the lipids do not tilt strongly, indicating high membrane orientation for all three samples. However the sVS multibilayers have a more isotropic I_0 distribution, i.e. lower orientation, which decreases slightly further when ΔN and Syb are incorporated. These effects possibly result from incomplete vesicle rupture [179] and the coupling of ΔN and Syb. Secondly the average chain-chain distance a varies only slightly at different ϕ for all multibilayers. a of pure lipid multibilayers prepared by sOS and sVS are almost the same ($\sim 4.5 \text{ \AA}$), while a increases significantly in the presence of SNAREs ($\sim 5 \text{ \AA}$). It seems that the incorporation of SNAREs increases the area per lipid of the host bilayers. Lastly, chain-chain correlation length ξ of the sOS multibilayer is significantly higher than the sVS multibilayers, demonstrating that sVS method results in bilayers with lower lateral chain correlation. ξ of the two sVS multibilayers are nearly the same, indicating that SNARE reconstruction does not affect the lateral chain correlation of sVS bilayers. Moreover ξ decreases with ϕ for all samples, indicating that untilted lipids ($\phi < 10^\circ$) have stronger chain-chain correlation than tilted ones ($\phi > 10^\circ$) [64].

5.1.3 PC-PE 4:1

Fig. 5.3 shows the GISAXS patterns of sVS PC-PE-PS-Chol 4:1 multibilayers recorded at ID01 at RH 95% and 50%. (left) Pure PC-PE (center) PC-PE reconstituted with SNAREs via the normal sVS routine, and (right) PC-PE reconstituted with *premixed* SNAREs (mixed before preparation). Images were taken at a number of hydration conditions including RH 95% and 50%, as shown in Fig. 5.3. In line with the PC-PE-PS-Chol multibilayers, at RH 95% both the sVS PC-PE multibilayers with/without SNAREs exhibit clean single lamellar phase. Moreover, 5 Bragg orders can be observed for both samples, also indicating that the sVS preparation results in multibilayers with high lamellar ordering comparable with the sOS preparation. The *premixed* SNAREs however give rise to less Bragg orders and two coexisting L phases, evidencing clear phase separation. In this special preparation, we assume that the full SNARE complex has been formed from the beginning and then been reconstituted via the micelle-vesicle-multibilayer pathway. Hence, the four-helix bundle is likely to anchor into the same bilayer via the two TMDs. Since this presumably extends the inter-bilayer distance to an unfavorable value, the system seems to react by phase separation. Such “kinetically or thermodynamically improbable conformation” [162] is one of the central concerns in the reconstitution of surface-associated proteins.

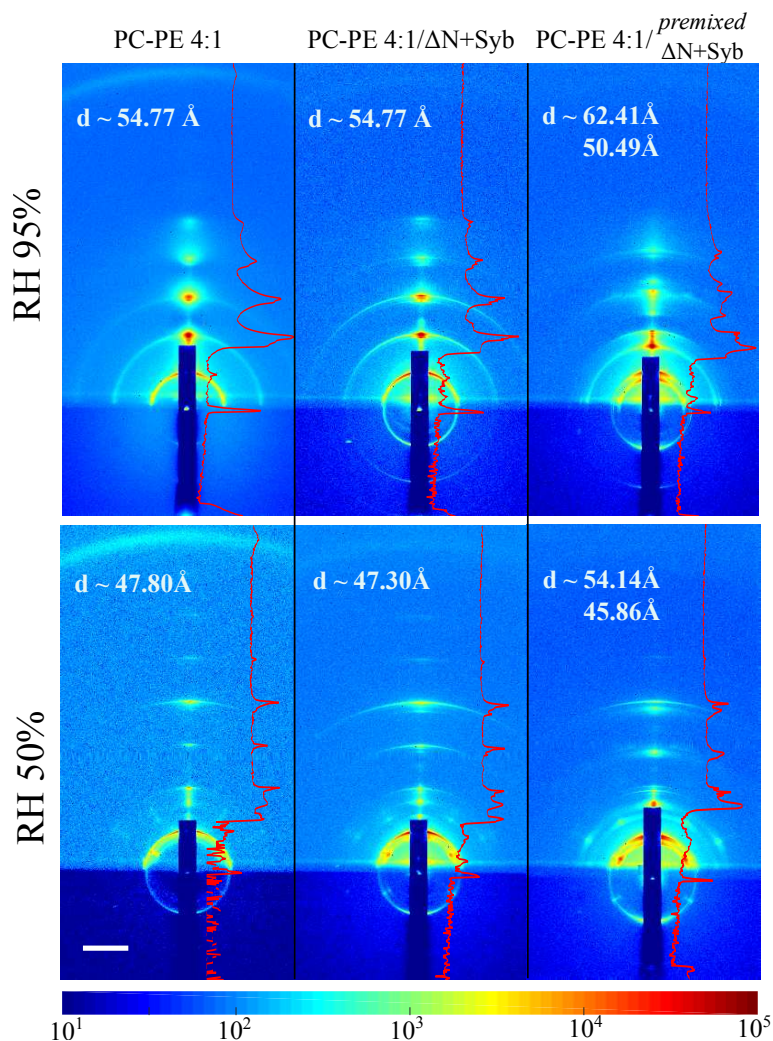


Figure 5.3: GISAXS patterns of *sVS* multibilayers of (left) pure PC-PE 4:1, (center) PC-PE 4:1 reconstituted with SNAREs via the normal *sVS* routine, and (right) PC-PE 4:1 reconstituted with premixed SNAREs (mixed before preparation), measured at RH 95% and 50%. The dark blue bar is the shadow of the rectangular beamstop. All images were recorded with 10 s exposure time with the specular beam lying between the primary beam and 1st Bragg peak behind the beamstop. The intensity profiles along the $q_{\parallel} = 0$ direction are plotted in red. The d values in the images denote the bilayer periodicities, and the white scale bar in the lowerleft corner indicates 50 pixels on the detector. The false color scale corresponds to the logarithmic scattering intensity.

At RH 50%, all measured PC-PE multibilayers show a phase coexistence of an H_{II} and an L phase. The same as PC-PE-PS-Chol multibilayers prepared by sVS, H_{II} phases appear instead of the expected R phase (i.e. stalk structures). Based on such observation on the two different lipid compositions at various hydration conditions, we now can conclude that the current sVS preparation yields multibilayers with different phase behaviors despite the same lipid composition. We assume that it mainly results from the unremoved n-OG, in agreement with the SAXS results of proteoliposomes in Section 4.4.5. It has been reported that n-OG is able to suppress the formation of non-lamellar phases [209]. However it is yet not clear whether n-OG alters multibilayers in the same way as in the literature. Due to the limitation in time of synchrotron measurements, we are unable to evaluate their phase behaviors in great detail.

5.2 In-house x-ray reflectivity studies of SNARE-reconstituted multibilayers

At ID01 we have already preliminarily investigated the sVS multibilayers of PC-PE-PS-Chol and PC-PE at several hydration conditions. Many aspects remain unclear due to the limited amount of time at synchrotron. Back home we systematically studied the PC-PE 4:1 sample family with more control samples and more hydration conditions, by making use of the in-house instrumentation. Pure PC-PE multibilayer prepared by sOS, pure PC-PE multibilayer, PC-PE/ Δ N multibilayer and PC-PE/ Δ N+Syb multibilayer prepared by sVS were investigated by both x-ray reflectivity and GISAXS.

5.2.1 Instrumentation

X-ray reflectivity experiments in this section were performed with the same home-built laboratory diffractometer **Wendi** as in Chap. 1 and 2. Briefly, the samples were mounted in the software-controlled humidity chamber, positioned in a $\theta/2\theta$ two-circle goniometer. A $1 \times 6 \text{ mm}^2$ Cu K_α beam ($\lambda = 1.54 \text{ nm}$, $E = 8.048 \text{ keV}$) hit the multibilayer at an incident angle θ . The intensity of the exit beam at exit angle 2θ was measured by a fast scintillation counter (Cyberstar, Oxford-Danfysik). Reflectivity curves at various hydration conditions were obtained by scanning θ from 0 to 10° for 2 s at each angle under controlled RH.

5.2.2 The effect of TR on PC-PE multibilayers

Before starting the systematic investigation of PC-PE multibilayers, a comparative assay was carried out to inspect the effect of Texas Red on multibilayer orientation. Texas Red (TR) is grafted onto dihexadecanoyl phosphoethanolamine (DHPE) and serves as a lipid dye in the sVS protocol to provide a better visual management of the elution process. However, it is worth noting that TR-DHPE may change the phase behavior of the host membranes [218]. To this end, we prepared two PC-PE multibilayers by sVS, one containing 0.67 wt% TR-DHPE and the other TR-DHPE free, which were both characterized by x-ray reflectivity at various hydration conditions.

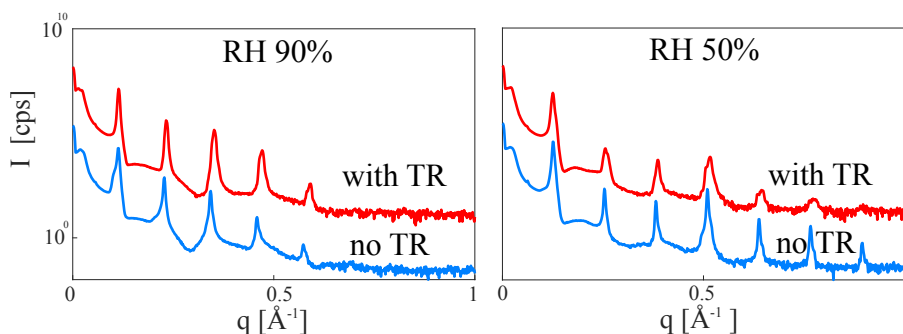


Figure 5.4: X-ray reflectivity curves of PC-PE 4:1 multibilayers with/without TR-DHPE prepared by sVS measured at RH 90% (left) and 50% (right). Scans were recorded at θ intervals of 0.01° and 2 s per step. The TR-free curves are shifted for clarity.

Fig. 5.4 shows reflectivity curves of both multibilayers at two hydration conditions, RH 90% for the lamellar phase and 50% for non-lamellar phases. At RH 90%, both curves exhibit single phase, with the Bragg peaks shifting to higher q in the presence of 0.67 wt% TR. On the one hand at higher hydration conditions, TR-DHPE does not affect the lamellar ordering at RH 90% so that the same number of Bragg orders appear. It seems that the TR groups or TR-DHPE as a whole can properly adapt themselves to the lamellar lattice, leading to undistorted bilayers. Furthermore, the bilayers become slightly thinner due to TR-DHPE. It has been reported by computational study that the hydrophobic TR groups tend to reside in the chain region [219], and thus increases the average area per lipid and reduces bilayer thickness. At RH 50%, significant difference between the two curves appear. In the presence of TR-DHPE, less Bragg orders can be observed and the Bragg peaks become broader. This result implies that under lower hydration conditions, TR drastically reduces the lamellar ordering

and the mosaic spread of the multibilayer [220]. The giant TR groups seem to be unable to properly adopt themselves to non-lamellar lattice in the way they have done in the lamellar phase above. Knowing that even small amount of TR might largely change the bilayer properties in our system, we hence completely abandoned the use of TR in the following sVS preparations, at the cost of more difficult elution management.

5.2.3 Systematic x-ray reflectivity studies of PC-PE 4:1 multibilayers

Rocking scan

Prior to the reflectivity scans, rocking scans were performed in the positions of the 1st Bragg peaks to achieve proper experimental alignments and to determine membrane mosaicity. The detector angle was fixed in the first Bragg position 2θ with $2\theta \equiv \alpha_i + \alpha_f$, where α_i and α_f denote the incident angle and exit angle. Rocking curves were obtained by scanning α_i around the equilibrium position θ at intervals of 0.002° with 2 s scanning time. Before fitting, all I_{max} are normalized to 1. Each rocking curve is then fitted by a single Gaussian:

$$I(\omega) = e^{-4\ln 2\omega^2/W^2}, \quad (5.2)$$

where $\omega = \alpha_i - \theta$ and W denotes the peak width (full width at half maximum, FWHM).

Fig. 5.5 shows both the rocking scans and the fits of different PC-PE 4:1 multibilayers at RH 90%, including pure PC-PE 4:1 multibilayer prepared by sOS, pure PC-PE 4:1, PC-PE 4:1/ Δ N and PC-PE 4:1/ Δ N+Syb multibilayers prepared by sVS. The peak width W obtained from fitting is listed in the legend: The W of the sOS multibilayer (0.043°) is smaller than all others, the W of sVS multibilayers of pure PC-PE 4:1 (0.050°) and PC-PE 4:1/ Δ N (0.049°) are slightly larger, and the W of the sVS multibilayer of PC-PE 4:1/ Δ N+Syb (0.070°) is the largest among all samples. These results suggest that (i) the sVS method leads to a lower membrane orientation compared with the sOS method, (ii) reconstruction of Δ N alone does not reduce membrane orientation and (iii) reconstruction of both Δ N and Syb significantly reduces the orientation. Despite the decrease of membrane orientation, all W here are comparable to literature values [15, 221]. Hence the sVS preparation yields sufficiently oriented multibilayers, even in the presence of both Δ N and Syb. All these findings are well in line with the GISAXS results above.

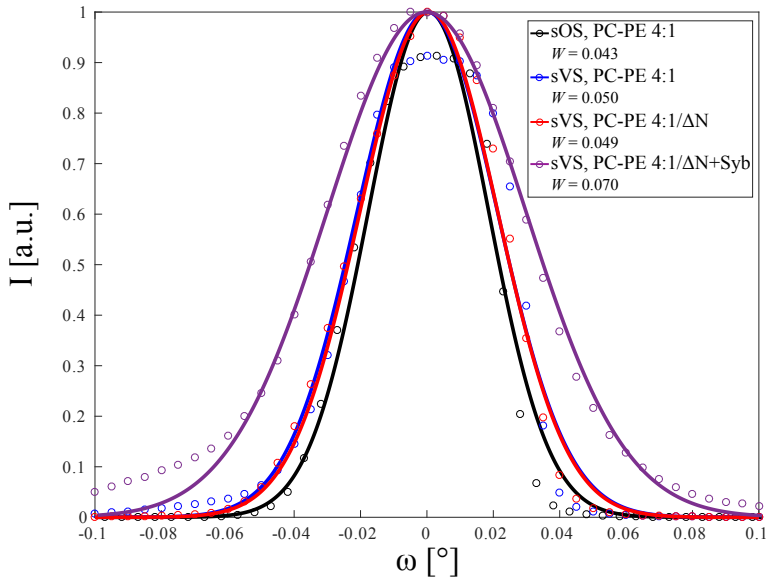


Figure 5.5: Rocking scans (circles) and fits (solid lines) of the PC-PE 4:1 multibilayers at RH 90%. Pure PC-PE 4:1 multibilayer prepared by sOS (black), pure PC-PE 4:1 multibilayer prepared by sVS (blue), PC-PE 4:1/ ΔN multibilayer prepared by sVS (red) and PC-PE 4:1/ ΔN +Syb multibilayer prepared by sVS (purple) are shown. The scans are fitted by Gaussian distributions with I_{max} being normalized to 1. The resulting peak width W (FWHM) is listed in the legend.

Raw reflectivity curves

Fig. 5.6 shows the reflectivity curves of PC-PE 4:1 multibilayers at various hydration conditions (RH 90-50% at 2 % intervals). (i) Pure PC-PE multibilayer prepared by sOS (black) results in typical reflectivity curves of sVS multibilayers in response to the RH: a series of sharp Bragg peaks appear at all measured RHs and shift to the high q region at lower RHs. (ii) PC-PE multibilayer prepared by sVS also give rise to a number of strong Bragg peaks, but less Bragg orders are visible especially at higher RHs. Such a decrease in Bragg orders has already been observed with GISAXS at ID01 beamline (Section 5.1.3), indicating a lower lamellar ordering and more static defects of the sVS method compared with the sOS method. Moreover, a new series of Bragg peaks show up at lower RHs (RH 60-70%, highlighted by the green arrows in Fig. 5.6), indicating a phase separation due to preparation method. On the positive side however, 5-8 Bragg orders is already a sign of high lamellar ordering. With them we can carry out EDP reconstitution by means of Fourier synthesis [222] (results shown in Fig. 5.7).

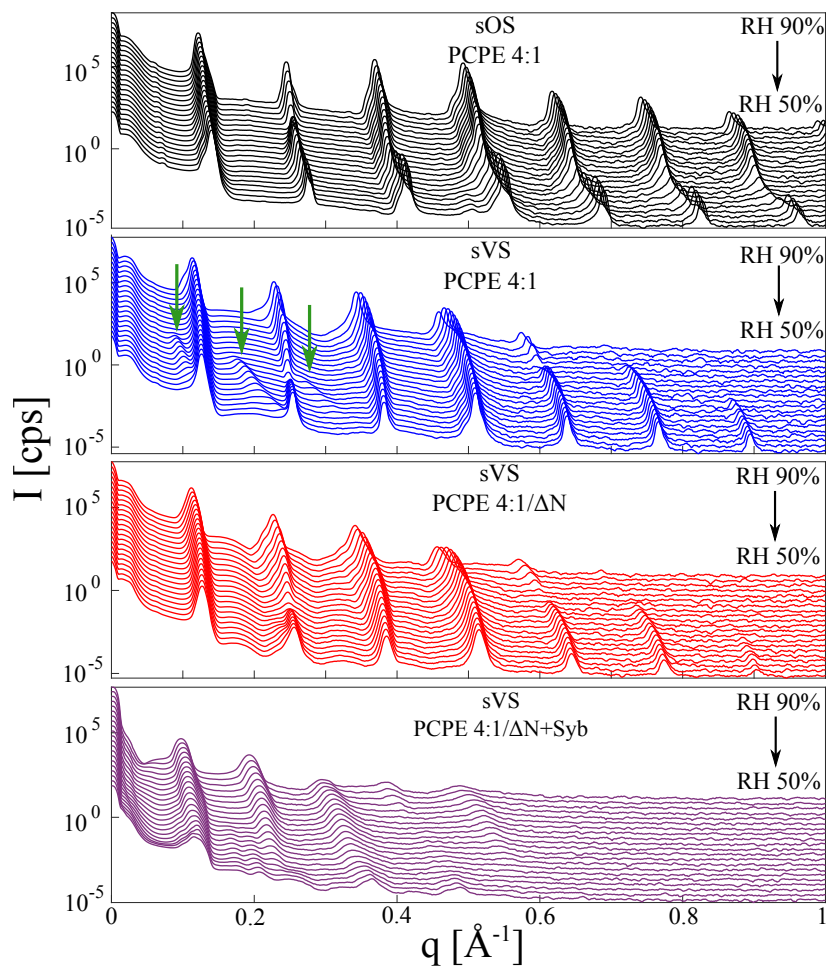


Figure 5.6: X-ray reflectivity curves of PC-PE 4:1 multibilayers measured at RHs 90-50% at 2% intervals. From top to bottom: (i) Pure PC-PE 4:1 multibilayer prepared by sOS, (ii) pure PC-PE 4:1 multibilayer prepared by sVS, (iii) PC-PE 4:1/ ΔN multibilayer prepared by sVS and (iv) PC-PE 4:1/ ΔN +Syb multibilayer prepared by sVS. Curves of lower RHs are shifted for clarity. The green arrows point to the new series of Bragg peaks.

Next we compare the reflectivity curves of the different samples prepared by the sVS method. The curves of sVS multibilayer with ΔN (red) are similar to the ones of the pure lipid sVS multibilayer, except that the secondary phase does not appear. Hence single SNARE, ΔN in this case does not largely modify the host structures either. The reflectivity curves of the multibilayer with mixed ΔN and Syb (purple) on the other hand shows a completely different lineshape with the other two sVS multibilayers, with Bragg peaks becoming weaker and less sharp, and shifting to smaller q_z . We have learned from the SAXS results that the incubation of ΔN and Syb vesicles does not alter the vesicle structure and size distribution. Thus such profound structural modification could only have taken place on the substrates where strong evacuation was applied to form a dry multibilayer. This way, bilayers were forced into close contact [162] and hence the fusion events were initiated. In the presence of both ΔN and Syb, the bilayer could dock, hemifuse or fuse, yielding a large variety of vesicle geometries and sizes [172]. As a result, PC-PE/ ΔN +Syb multibilayer exhibit lower lamellar ordering compared to the other sVS multibilayers.

EDP reconstruction

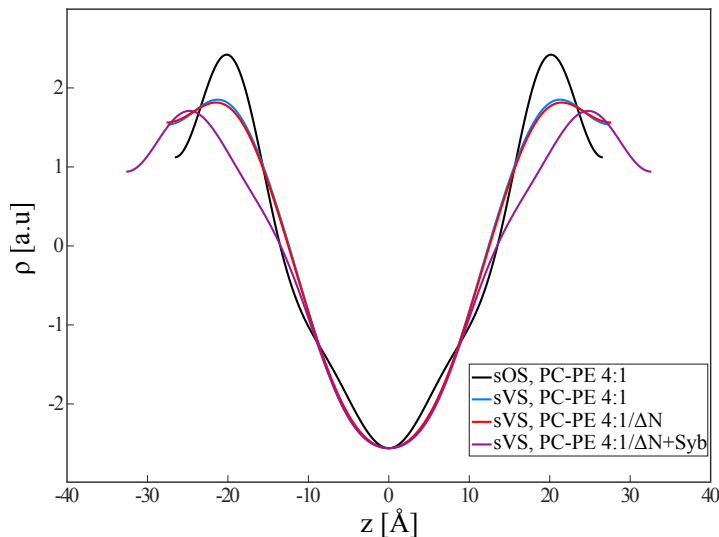


Figure 5.7: EDPs of the PC-PE 4:1 multibilayers at RH 90% reconstructed from the reflectivity curves in Fig. 5.6. The phase combination of $-1, -1, +1, -1, +1$ is used. The electron densities are in arbitrary units and are normalized by the electron density of the methyl dip.

As we can see in the reflectivity curves, although the sVS preparation and SNARE coupling reduces the lamellar ordering, there are still enough Bragg orders for EDP reconstitution analysis, at least at higher hydration conditions. Here the swelling method as introduced in Chap. 1 can not be performed due to the lack of experimental conditions. Instead, the phase combination $-1, -1, +1, -1, +1$ is directly used based on previous results [25,65], yielding reasonable EDPs at higher hydration conditions (e.g. RH 90%) by means of Fourier synthesis. However, it is rather difficult to perform the same reconstruction at lower RHs especially for the multibilayer with both ΔN and Syb due to the lack of Bragg orders and unclear separation between peaks.

Fig. 5.7 shows the EDPs of all 4 multibilayers at RH 90%. Assuming that the electron density of the methyl group at the end of the acyl chain stays constant, EDPs of different multibilayers are normalized by the intensities of the methyl dip. On the one hand, the EDP of the pure PC-PE multibilayer by sOS shows the typical bilayer EDP distribution of single lamellar multibilayers [223]: the headgroup separates clearly with the water region and the carbon chains. On the other hand, for the EDPs of the sVS multibilayers (blue, red and purple) the contrast between different lipid segments are no longer significant. This could be explained by the fact that there are more defects in the sVS multibilayers, resulting in lower lateral order (as shown by the chain-correlation results) and less distinguishable segment separation. The highly overlapping EDPs of PC-PE and PC-PE/ ΔN sVS multibilayers demonstrate that the reconstruction of single SNARE barely changes the membrane structure. However, the EDP becomes much wider when the two SNARE are mixed indicating higher level of swelling. It could possibly originate from the coupling effect between ΔN and Syb. In this case the fully assembled SNARE complex with the 4-helix bundle has to be accommodated into the multilamellar structure, leading to significant structural change in the host membrane. Nonetheless, at this point we cannot come to any 3d structures to properly address our observation. Interestingly, the EDPs of the sVS multibilayers overlap with each other in the acyl region. It seems that in multibilayers of PC-PE 4:1 their TMDs can match the lipid carbon chains well without drastic structural distortion.

Bilayer periodicity d

Due to the lack of Bragg orders and poor peak sharpness, we are unable to perform EDP reconstitution for all RHs. The bilayer periodicity d offers an estimation of the bilayer structures assuming that d_{hh} is proportional to d . Fig. 5.8 plots the bilayer periodicities d of PC-PE multibilayers with respect to RH. We

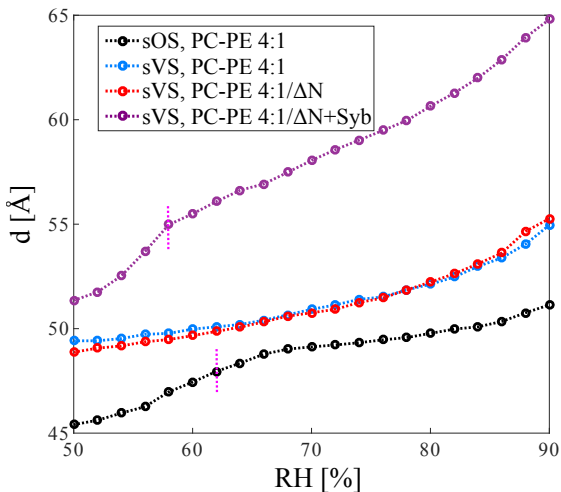


Figure 5.8: Plots of bilayer periodicity d of the PC-PE 4:1 multibilayers as a function of the RH, derived from the x-ray reflectivity curves in Fig. 5.6. Only the orders between the first and the last orders are used in the calculation. The standard deviations are smaller than the size of the markers and thus not plotted. Each circle marker represents a performed measurement. The two vertical pink lines denote possible phase transition at the RH*.

can find that (i) the d of pure PC-PE prepared by sVS is larger than pure PC-PE prepared by sOS, (ii) the d plots of pure PC-PE and PC-PE/ Δ N almost overlap, and (iii) d increases significantly in the presence of both Δ N and Syb. These results are in line with the observations in the EDP section that sVS preparation swells the bilayers, Δ N reconstitution causes no observable structural modification and Δ N and Syb coupling swells the bilayers even further. Secondly, we could deduce the phase transition from the changes in curve slopes [21], but only as an indirect evidence. As expected, the pure PC-PE multibilayer prepared by sOS transform into a non-lamellar phase at RH 68% as indicated by the sudden slope change of its d plot (black). In contrast, neither the reflection curve of pure PC-PE multibilayer prepared by sVS (blue) nor the reflection curve of PC-PE multibilayer containing Δ N (red) shows such a transition. Interestingly, when both Δ N and Syb are present (purple), a possible phase transition occurs at RH 58%. Notwithstanding we can not confidently determine phase transitions merely from d , unless more convincing proofs are found. In order to provide further support to the findings in this section, careful in-house GISAXS experiments were then performed on the same multibilayers and at the same RHs.

5.3 In-house GISAXS investigations of SNARE-reconstituted multibilayers

5.3.1 Instrumentation

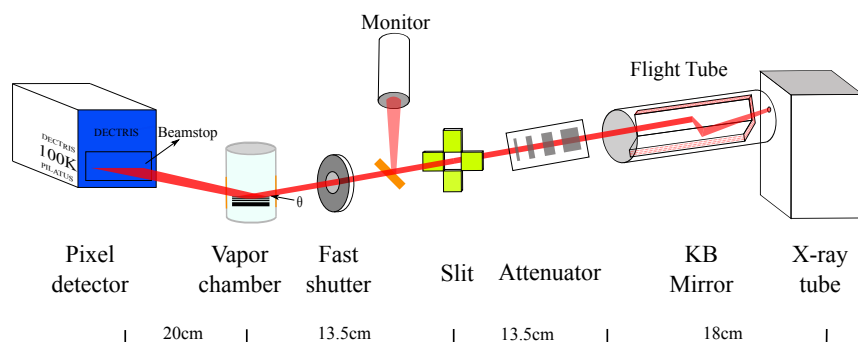


Figure 5.9: Layout of laboratory beamline **Rosi**. Distances between key components are noted under the layout.

The in-house GISAXS experiment was performed on the self-built laboratory diffractometer **Rosi**, which is sketched in Fig. 5.9. The $\text{Cu K}\alpha$ ($\lambda = 1.54 \text{ nm}$, $E = 8.048 \text{ keV}$) beam was produced by a rotating anode generator (MicroMax-007 HF, Rigaku) operating at $U = 40 \text{ kV}$ and $I = 30 \text{ mA}$. The effective size of the focal spot was a 0.07 mm circle at 6° take-off angle, yielding a total flux of $6.13 \times 10^8 \text{ cps}$. A pair of Kirkpatrick-Baez mirrors (Confocal Max-Flux Optics, Osmic) was used to collimate and monochromatize the divergent beam. Afterwards the beam was attenuated by combining 4 Cu foils with different thickness (see Appendix D.1), and then defined to $1 \times 1 \text{ mm}^2$ size by the entrance slits. A monitor (Siemens) and a fast shutter were mounted between the slits and the sample to inspect the intensity before the sample and to protect the detector. The samples were placed in the same vapor chamber as used for **Wendi**, which was mounted on a 6-axis goniometer stage (Huber). The beam entered the multibilayer at an incidence angle $\theta \approx 0.6^\circ$ and the exit beam was captured by a Pilatus 100K pixel detector (DECTRIS) with 487×195 pixels and $172 \times 172 \mu\text{m}^2$ pixel size, mounted 20 cm behind the sample. A square Si ($2.34 \times 2.34 \times 1.00 \text{ mm}^3$) beamstop was glued onto the Kapton window direct in front of the detector to attenuate the bright primary beam. Each image was recorded with 1000 s exposure time.

5.3.2 Systematic GISAXS characterizations of PC-PE 4:1 at various RHs

Fig. 5.10 shows the in-house GISAXS patterns of PC-PE 4:1 multibilayers measured at various hydration conditions (RH 88-50% at 2% intervals). (Row 1) pure PC-PE prepared by sOS, (Row 2) pure PC-PE prepared by sVS, (Row 3) PC-PE with ΔN prepared by sVS, and (Row 4) PC-PE with both ΔN and Syb prepared by sVS. The first row shows the familiar phase transition from the L phase to the rhombohedral (R) phase [21, 25]. The hallmark of the R phase is the two off-axis peaks on each side of the in-plane peaks, which are most clearly visible in the GISAXS pattern at RH 50%. For PC-PE 4:1, the phase transition happens around 60%, comparable to 68 % that Fig. 5.6 has predicted. With this information at hand, we turn to the sVS samples. In the ideal case, the measured phase diagram should be an intrinsic property of the lipid mixture, not of the preparation. However, this turns out not to be the case. In contrast to the sOS sample, where single phase behavior is always observed, we obtain a pronounced phase-coexistence regime at lower RHs from sVS multibilayers. Furthermore, neither of the two phases transform into the R phase when the RH further decreases, even in the presence of both ΔN and Syb. The first L phase persists while the second L phase transforms into the H_{II} . One may speculate whether the difference in the phase diagram, in particular the appearance of the H_{II} phase instead of the R phase, can be attributed to the higher defect level in the sVS preparation. While the influence of defects on the phase diagram in soft condensed matter [224] is not completely implausible, we rather believe that this unexpected and complex phase behavior originates from remaining detergent (mainly n-OG) introduced by the preparation. Comparison of pure vesicles prepared by sonication and size-exclusion above have already proved the existence of abundant n-OG in vesicles prepared by the new protocol. In the multibilayers it further inhibits the transitions to non-lamellar phase [209], and also gives rise to a new phase which could transform from L to H_{II} phase at lower RHs [225]. Moreover, the structure of the new phase appears to be rather irregular if we compare the three sVS samples, perhaps due to the random concentration of remaining n-OG.

5.3.3 The effect of extra purification on PC-PE 1:1

In the last few sections, it was found that large amount of n-OG remains after two runs of G-25 column dilution and affects the phase behaviors of resulting

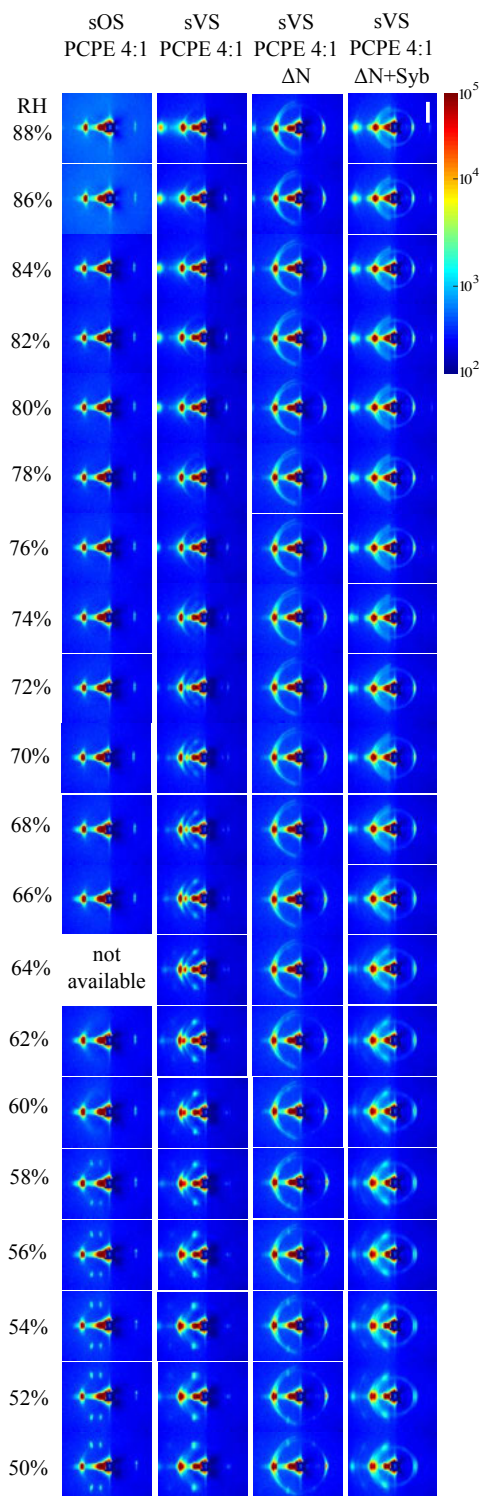


Figure 5.10: In-house GISAXS patterns of PC-PE 4:1 multibilayers recorded at various hydration conditions (RH 88-50% at 2% intervals). From left to right: (Row 1) Pure PC-PE multibilayer prepared by sOS, (Row 2) pure PC-PE multibilayer prepared by sVS, (Row 3) PC-PE/ ΔN multibilayer prepared by sVS and (Row 4) PC-PE/ $\Delta N + \text{Syb}$ multibilayer prepared by sVS. Each exposure was recorded for 1000 s. The dark shadow in the center of all images results from the beamstop which attenuates the primary beam. In the upper right corner, the false color scale corresponds to the logarithmic scattering intensity and the white scale bar denotes 20 pixels on the detector.

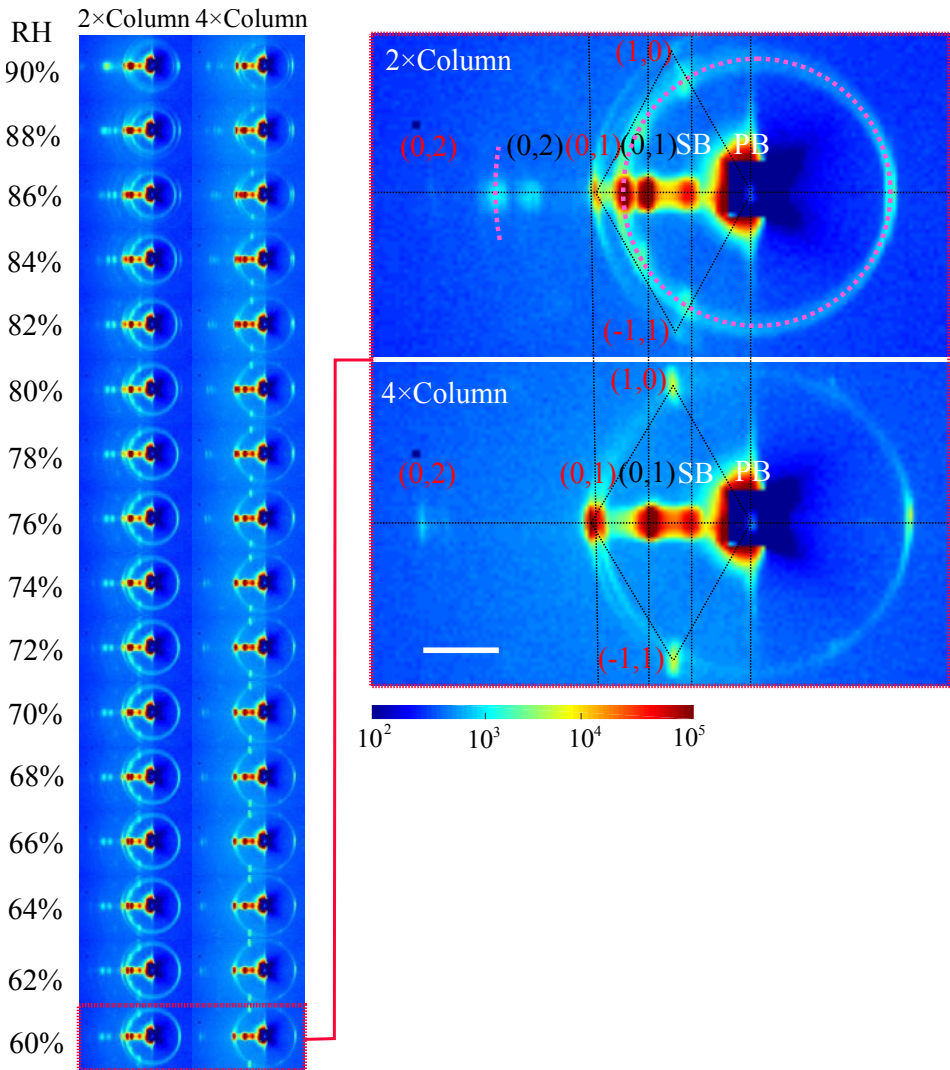


Figure 5.11: In-house GISAXS patterns of PC-PE 1:1 multibilayers prepared by sVS recorded at various hydration conditions (RH 90-60% at 2% intervals).

(a): (Left) normal purification routine, i.e. 2 times through the columns and (right) extra purification routine, i.e. 4 times through the columns. The dark shadow in the center of each exposure results from the beamstop which attenuates the primary beam.

(b): Zoom of the two diffraction patterns at RH 60%. For both samples, the primary beam (PB) and specular beam (SB) are denoted in white, the lamellar indices in black and hexagonal indices in red, with vertical dash lines connect common phases. The pink dash circle/arc in the upper image denotes the additional phase which does not appear in the lower one. The false color scale corresponds to the logarithmic scattering intensity and the white scale bar denotes 20 pixels on the detector.

multibilayers. Many approaches can be taken to fully remove n-OG, including extra column runs, dialysis and hydrophobic adsorption [226]. Here we preliminarily attempt to apply 2 extra column runs to the proteoliposome suspensions. The multibilayers via normal purification routine (2 column runs) and extra purification routine (4 column runs) were investigated with in-house GISAXS.

Fig. 5.11 shows the GISAXS patterns of PC-PE 1:1 multibilayers prepared via 2 and 4 column runs. Fig. 5.11a presents the two sets of exposures at various hydration conditions (RH 90-60% at 2% intervals). An extremely complicated phase behavior is observed on the first set for which only 2 column runs were performed. Generally up to 3 phases appear at all RHs. In contrast, the second set exhibits a much cleaner phase behavior with only 2 phases coexisting in the diffraction patterns. The extra purification runs seem to work by delivering cleaner diffraction patterns containing less phases. We then take a look at the diffraction patterns at RH 60% more carefully (Fig. 5.11b). The common phase in both samples is indexed as one L phase (black) and one H_{II} phase (red). The additional phase of the sample with standard purification is possibly 12-fold symmetric quasi-crystal [227, 228] or a gyroid cubic phase [229], which can not be undoubtedly indexed due to weak peak intensity. Either way, such a phase is rather uncommon for pure lipid systems in this hydration condition range. It is therefore assumed to be a result of n-OG partitioning into the lipid bilayers. This difference clearly demonstrates that the standard purification procedure does not sufficiently remove the detergents for meaningful phase diagram studies. To this end the purification procedures of the sVS preparation has to be improved, maybe at the expense of yield and efficiency. This preliminarily attempt with extra column runs only offers a possible approach of further purification, but is not necessarily more efficient compared with dialysis and hydrophobic adsorption.

5.4 Summary and outlook

In this chapter the effects of sVS preparation as well as SNARE reconstitution on multibilayer structures are evaluated by x-ray reflectivity and GISAXS. Results show: (i) the sVS preparation results in thicker bilayers compared to sOS, probably due to n-OG and incomplete vesicle rupture. (ii) ΔN alone does not dramatically alter the bilayer structures. (iii) the coupling of ΔN and Syb can bring about drastic membrane misorientation and swelling but no stalk structures, possibly due to the remaining n-OG in the multibilayers and (iv) extra

purification is able to reduce n-OG remaining, hence simpler phase behavior. In the future further efforts shall be made to thoroughly remove the remaining n-OG with more effective detergent removal techniques, in order to observe SNARE-mediated stalk formation in the multibilayer system, and eventually reconstruct 3d stalk structures in the presence of SNAREs.

6 Conclusion and outlook

The aim of this thesis is to extend previously established x-ray studies of stalk formation in pure lipid multibilayers to more complex systems closer to actual physiological conditions of fusion events in *vi vo*. To this end, efforts on three levels have been devoted, namely the lipid level, the peptide level and the protein level.

On the lipid level, we found a “magic lipid mixture” for which the minimal osmotic pressure is required to promote fusion, i.e. the highest RH*, so that pure lipid stalk formation can take place in the aqueous environment where merely mild osmotic pressure can be induced by solutes like PEG. After a series of attempts with binary, ternary and quaternary lipid mixtures, we found that the PC-PE-Chol 45:45:10 mixture forms a single stalk (*R*) phase at RH \leq 87%, which is already achievable by PEG aqueous solutions. First GISAXS results showed that indeed this mixture can form stalks in PEG-400 aqueous solutions which offer equivalent osmotic pressure (PEG mass fraction \geq 65%), but in the presence of an unexpected H_{II} phase which might disturb the structural characterizations in more complex lipid systems. Consequently, prior to the introduction of physiological conditions like pH level and ion strength, progress has to be made to eliminate the additional H_{II} phase.

On the peptide level, we investigated two families of transmembrane D- β -peptides, one with one without additional tryptophan anchors, aiming at structurally stable and tailorable β -helical TMDs. By introducing I-labels into either the tail region or the center region of the peptides, we were able to determine the relative positions of these moieties with respect to the lipid bilayers. CD spectra and x-ray scattering results demonstrate that β -peptides with desired helical structures are successfully integrated into DOPC bilayers in a transmembrane fashion. Moreover, β -peptides adopt a slightly tilted conformation to compensate for the peptide-lipid hydrophobic mismatch, which can be diminished by additional tryptophan anchors. Based on this approach, in the future we could design and synthesize complete SNARE analogs containing β -helical TMDs, in association with various fusion recognition motifs and linkers [230].

On the protein level, a novel vesicle-based protein-compatible preparation protocol for supported multibilayers has been developed, so that stalk formation can be studied in the presence of SNAREs in the multibilayer system. This new protocol consists of three stages as shown in Fig. 3.6: (i) SNAREs

are co-micellized together with n-OG and lipids, yielding n-OG/lipid/SNARE proteomicelles; (ii) n-OG is then removed by size-exclusion, resulting in lipid/SNARE proteoliposomes; (iii) SNARE-reconstituted multibilayers are obtained by spreading vesicle suspensions (the sVS method) onto the substrates. Both the proteomicelles and proteoliposomes have been characterized by SAXS with the data being fitted by parameterized models. Results show that SNAREs are successfully incorporated into micelles and vesicles via co-micellization and size-exclusion, and that SNARE reconstitution induces a minor bilayer thickening effect. Mixing the two proteoliposome suspensions yields multibilayers containing both SNAREs (ΔN as the t-SNARE and Syb as the V-SNARE). Subsequent x-ray reflectivity and GISAXS characterizations reveal that the coupling effect of the two SNAREs under partial dehydration significantly thickens the bilayers and reduces their lamellar ordering, and that an H_{II} phase instead of an anticipated R phase is observed probably due to incomplete removal of n-OG. At present we have successfully reconstituted SNAREs into supported multibilayers via the novel sVS protocol, but failed to observe stalk structures in sVS multibilayers containing SNAREs. To this end in the future we shall seek more effective purification procedures and preparation conditions to fabricate multibilayers with higher orientation and less impurity, and eventually achieve our long term goal: 3d EDP reconstruction of stalk structures in the presence of SNAREs.

Appendix

A.1 Major x-ray reflectivity measurements in Chap. 1

	Sample	Figure	Labbook	Date	Remarks
Binary mixtures	DOPC-DOPE	1.7	Wendi 15	29.03.15	
	DOPC-DOG	1.8	Wendi 13	13.01.13	
	DOPC-Chol	1.9	Wendi 12	01.01.12	by S. Aëffner [19]
	DOPC-SDPC	1.10	Wendi 14	27.11.14	
	DOPC-SDPE	1.11	Wendi 15	26.03.15	
	DOPC-PIP ₂	1.12	Wendi 11	18.03.09	by S. K. Ghosh [20]
Ternary mixtures	PC-PE-DOG	1.13	Wendi 13	06.02.13	
	DOPC-Chol	1.14	Wendi 13	12.03.13	
	DOPC-PIP ₂	1.15	Wendi 13	28.08.11	by Z. Khattari [25]
Quaternary mixtures	PC-PE-Chol-DOG	1.16	Wendi 15	11.04.13	
	PC-PE-Chol-PIP ₂	1.17	Wendi 14	04.06.13	
	PC-PE-Chol-SM	1.18	Wendi 13	18.07.11	by Z. Khattari [25]

A.2 Filter parameters of the in-house reflectometer Wendi

Index	Thickness [μm] ^a	Transmission (theoretical) ^b	Transmission (experimental)
1	0	1.00	1.00
2	150	0.14	0.12
3	300	2.15×10^{-2}	1.67×10^{-2}
4	450	3.16×10^{-3}	2.00×10^{-3}
5	600	4.65×10^{-4}	6.25×10^{-4}
6	750	6.84×10^{-5}	3.90×10^{-5}

^a Made of aluminum.

^b Taken from http://henke.lbl.gov/optical_constants/filter2.html.

A.3 Reflectivity curves of PC-PE-DOG 45:45:10

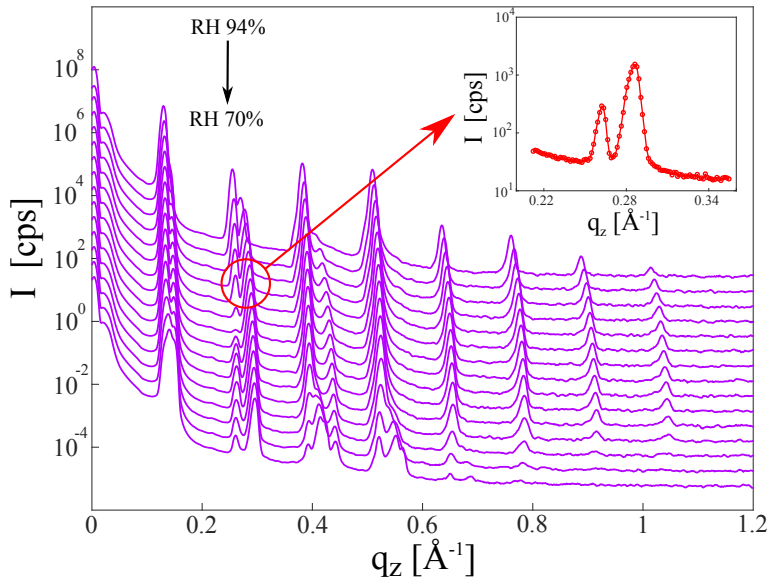


Figure A.1: Reflectivity curves of PC-PE-DOG 45:45:10 at RH 94-70%. Data plotted in logarithmic scale and scaled for clarity. Inset: Zoom of the 2nd Bragg peak at RH 90%.

A.4 Reflectivity curves of PC-PE-Chol 40:40:20

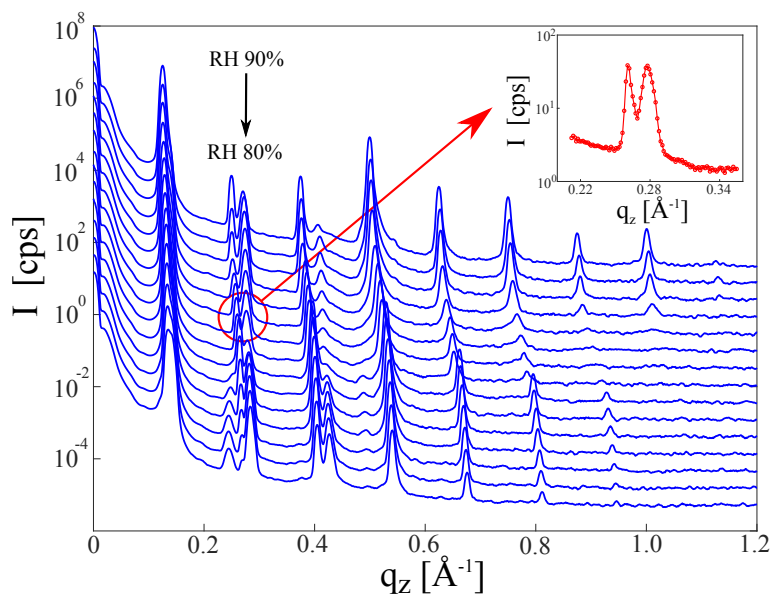


Figure A.2: Reflectivity curves of PC-PE-Chol 40:40:20 at RH 90-80%. Data plotted in logarithmic scale and scaled for clarity. Inset: Zoom of the 2nd Bragg peak at RH 86%.

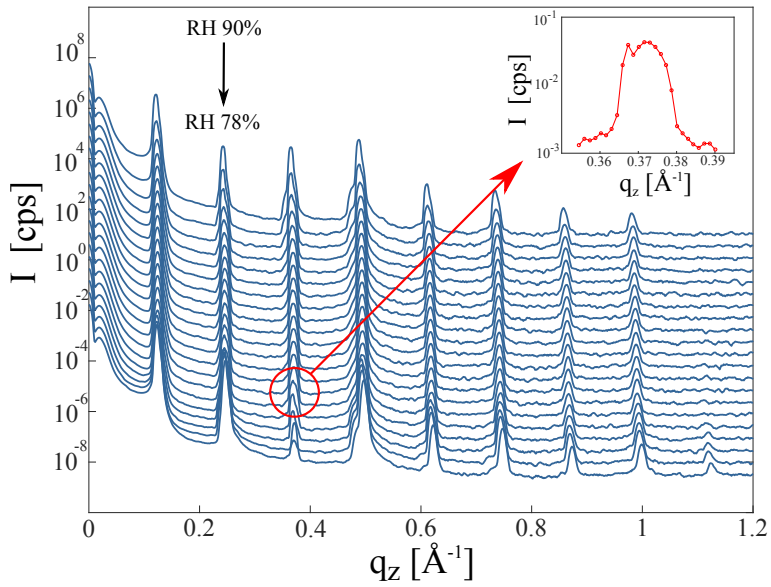
A.5 Reflectivity curves of PC-PE-PIP₂ 35:35:30

Figure A.3: Reflectivity curves of PC-PE-PIP₂ 35:35:30 at RH 90-78%. Data plotted in logarithmic scale and scaled for clarity. Inset: Zoom of the 3rd Bragg peak at RH 87%.

B.1 Preparation and fitting conditions of vesicles investigated in this work

Figure	Sample	Lipid composition (molar ratio)	Lipid concentration (mg/ml)	SNARE ^a	Preparation	Buffer	Vesicle structure	Fitting
4.3a	1	PC-PE 1:1	4	-	Column	H ₂ O	multilamellar	not fitted
	2	PC-PE-Chol 47.5:47.5:5						
	3	PC-PE-Chol 45:45:10						
	4	PC-PE-Chol 40:40:20						
4.3b	1	PC-PE 1:1	5	-	Sonication	H ₂ O	multilamellar	not fitted
	2	PC-PE-Chol 47.5:47.5:5						
	3	PC-PE-Chol 45:45:10						
	4	PC-PE-Chol 40:40:20						
4.10	1	PC-PE-Chol-SM 35:30:15:20	5	-	Sonication	H ₂ O	multilamellar	not fitted
	2	PC-PE-Chol-SM-PS 31:27:14:18:10					unilamellar	
4.11	1	PC-PE 1:1	5	-	Sonication+extrusion	H ₂ O	unilamellar	symmetric model
	2	PC-PE-PIP ₂ 47.5:47.5:5			Sonication			&
	3	PC-PE-PIP ₂ 45:45:10			Sonication			constant background
	4	PC-PE-PIP ₂ 40:40:20			Sonication			
4.12	1	PC-PE 1:1	5	-	Sonication+extrusion	H ₂ O	unilamellar	symmetric model
	2	PC-PE-PIP ₂ 47.5:47.5:5			Sonication			asymmetric model
	3	PC-PE-PIP ₂ 45:45:10			Sonication			&
	4	PC-PE-PIP ₂ 40:40:20			Sonication			constant background
4.13	1	PC-PE-PIP ₂ 47.5:47.5:5	5	-	Sonication	2.5 mM CaCl ₂	multilamellar	not fitted
	2	PC-PE-PIP ₂ 45:45:10			Sonication			
	3	PC-PE-PIP ₂ 40:40:20			Sonication			
4.14	1	PC-PE 4:1	7	-	Column	H ₂ O	multilamellar	not fitted
	2	ΔN						
	3	Syb						
	4	$\Delta N/Syb$						
4.15	1	PC-PE 4:1	7	$\Delta N/Syb$	Column	H ₂ O	multilamellar	not fitted
	2			$\Delta N/Syb$				
4.16	1	PC-PE-PS-Chol 5:2:2:1	5	-	Sonication	H ₂ O	unilamellar	symmetric model
	2		7		Column			&
	3			ΔN				constant background
	4			Syb				
	5			$\Delta N/Syb$				
4.17	1	PC-PE-PS-Chol 5:2:2:1	0.01	-	Sonication	H ₂ O	unilamellar	logarithmic number-weighting
	2				Column			
	3			ΔN				
	4			Syb				

^a Protein/lipid ratio 1:500

B.2 The MATLAB code to fit micelle SAXS curves

```

1  %%%%%%%%%%%%%%%%%%%%%%%%%%%%%%%%%%%%%%%%%%%%%%%%%%%%%%%%%%%%%%%%%%%%%%%%%%
2  %      function to calculate the theoretical intensity          %
3  %      model taken from J. Lipfert et al. J. Phys. Chem. B 2007  %
4  %      by Yihui Xu and Karlo Komorowski, Feb 2016             %
5  %%%%%%%%%%%%%%%%%%%%%%%%%%%%%%%%%%%%%%%%%%%%%%%%%%%%%%%%%%%%%%%%%%%%%%%%%%
6
7  % to be fitted:
8  % the minor semi-axis length a, the major semi-axis length b,
9  % the carbon chain ED rho1, the headgroup ED rho2
10 % the bilayer thickness Ta and Tb,
11 % the scaling factor s and offset f
12
13 function I = I_micelle(P,Scan_suspension,range)
14
15 q = Scan_suspension(range,1)*0.1; % scattering vector in Angstrom
16
17 % read all fitting parameters
18 a = P(1); % minor semi-axis length in Angstrom
19 b = P(2); % major semi-axis length in Angstrom
20 rho1 = P(3); % inner rho (carbon chain) in e/A^3
21 rho2 = P(4); % outer rho (headgroup) in e/A^3
22 ta = P(5); % bilayer thickness in a direction in Angstrom
23 tb = P(6); % bilayer thickness in b direction in Angstrom
24 s = P(7); % scaling factor
25 f = P(8); % offset
26
27 V1 = 4*pi*a*b^2/3; % core volume
28 Vt = 4*pi*(a+ta)*(b+tb)^2/3; % total volume
29
30 % replace qR with u
31 % replace cos(th) with x
32 u1 = @(x)q*sqrt(a^2*x.^2 + b^2*(1-x.^2));
33 u2 = @(x)q*sqrt((a+ta)^2*x.^2+(b+tb)^2*(1-x.^2));
34
35 % I as a function of x
36 % adapted bessel function: besselj(n+1/2,x)*sqrt(pi/(2*x))
37 I_x = @(x) ((3*V1*(rho1-rho2)* besselj(1+1/2,u1(x)).*sqrt(pi./(2*u1(x)
38         + 3*Vt*(rho2-0.334)* besselj(1+1/2,u2(x)).*sqrt(pi./(2*u2(x)))
39         ./u2(x)).^2;
40 % intergrate x from 0 to 1
41 I = integral(I_x,0,1,'ArrayValued',true);
42 % add s and f to match the calculated I with the experimental I
43 I = I*s + f;
44 end

```

B.3 The MATLAB code to fit vesicle SAXS curves

```

1 %%%%%%%%%%%%%%%%%%%%%%%%%%%%%%%%%%%%%%%%%%%%%%%%%%%%%%%%%%%%%%%%%%%%%%%%%%
2 %           symetric planar bilayer model                               %
3 %           model taken from P. Szekely et al., Langmuir, 2010         %
4 %           by Karlo Komorowski and Yihui Xu, Feb 2016                 %
5 %%%%%%%%%%%%%%%%%%%%%%%%%%%%%%%%%%%%%%%%%%%%%%%%%%%%%%%%%%%%%%%%%%%%%%%%%%
6
7 function I = I_Vesicle_Sym(P,Scan_vesicle,ran)
8
9 q           = Scan_vesicle(ran,1); % q-range (nm)
10
11 % Setup parameters for the symetric planar bilayer model
12 % Peak position z / Angstrom
13 z(1) = P(1); % headgroup 1 in Angstrom
14 z(2) = 0; % chain region in Angstrom
15 z(3) = -P(1); % headgroup 2 in Angstrom
16
17 % Amplitude of rho
18 r(1) = P(2); % headgroup 1 in a.u.
19 r(2) = -1; % chain region in a.u.
20 r(3) = P(2); % headgroup 2 in a.u.
21
22 % FWHM tau of the Gassian shells, sigma = tau/2.35
23 t(1) = P(3); % headgroup 1 in Angstrom
24 t(2) = P(4); % chain region in Angstrom
25 t(3) = P(3); % headgroup 2 in Angstrom
26
27 % Scaling factor and offset
28 s = P(5);
29 f = P(6);
30
31 % Form factor (FF) calculation
32 I = zeros(1,length(q))';
33 for i=1:3
34     for j=1:3
35         I = I +...
36             (2*pi^3./((q.^2)*log(2)))*...
37             r(i)*r(j)*t(i)*t(j).*...
38             exp(-(q.^2.*(t(i).^2 + t(j).^2))./(16.*log(2))).*...
39             cos(q.*(z(i)-z(j)));
40     end
41 end
42
43 % add s and f to match the calculated I with the experimental I
44 I = I*s + f;
45
46 end

```


C.1 Estimation of N_{SNARE} per Micelle

To better interpret the presence or absence of changes in the SAXS measurements with SNARE reconstitution, it is essential to first estimate the average SNARE number per micelle, since the SAXS measurements correspond to an ensemble average (see the discussion in the main text). Below we present the parameters used in the corresponding calculation, i.e. SAXS results in Tab. 1a for the micelle geometry, literature values for lipid and surfactants¹ and the stoichiometry parameters of our preparation. We conclude that only 9% of all micelles have a reconstituted SNARE protein.

List of constants²

V_{nOG} [\AA^3]	243	volume per nOG molecule
V_{lipid} [\AA^3]	1620	volume per lipid molecule
M_{nOG} [g/mol]	282	molecular mass of nOG
M_{lipid} [g/mol]	876	molecular mass of the lipid
CMC [mg/ml]	6.08	critical micelle concentration of nOG
m_{nOG} [g]	1.80	mass of nOG
m_{lipid} [g]	1.00	mass of the lipid
V_{solution} [μl]	0.07	volume of the micelle suspension
a [\AA]	11.87	fitted polar radius of Syb proteomicelles
b [\AA]	31.40	fitted equatorial radius of Syb proteomicelles
t_a [\AA]	12.59	fitted polar shell thickness
t_b [\AA]	2.71	fitted equatorial shell thickness
$R_{\text{protein/lipid}}$	1:500	protein/lipid molar ratio

Calculation

$$V_{\text{micelle}} = \frac{4}{3}\pi(a + t_a)(b + t_b)^2 \approx 119209^3 \quad (\text{C.1})$$

$$R_{\text{lipid/nOG}} = \frac{m_{\text{lipid}}/M_{\text{lipid}}}{(m_{\text{nOG}} - V_{\text{solution}} \cdot \text{CMC})/M_{\text{nOG}}} \approx 0.27 \quad (\text{C.2})$$

$$N_{\text{nOG}} = \frac{V_{\text{micelle}}}{V_{\text{nOG}} + V_{\text{lipid}}R_{\text{lipid/nOG}}} \approx 175 \quad (\text{C.3})$$

$$N_{\text{SNARE}} = N_{\text{nOG}}R_{\text{lipid/nOG}}R_{\text{protein/lipid}} \approx 0.09 \quad (\text{C.4})$$

¹ Almog *et al.* (1990) and Wenk *et al.* (1997).

² Parameters of DOPC rather than the lipid mixtures are used.

C.2 Estimation of N_{SNARE} per Vesicle

Similar to the estimation in Appendix A, we have performed a calculation of the copy number N_{SNARE} per vesicle. Below we present the calculation using parameters obtained from literature³, SAXS results in Tab. 1b and DLS results in Appendix B.

List of constants⁴

$V_{\text{lipid}} [\text{\AA}^3]$	1620	volume per lipid molecule
$R_0 [\text{\AA}]$	300	mean vesicle radius from DLS
$Db [\text{\AA}]$	36.76	bilayer thickness from SAXS fitting
$R_{\text{protein/lipid}}$	1:500	protein/lipid molar ratio

Calculation

$$V_{\text{out}} = \frac{4}{3}\pi R_0^3 \approx 1.13 \times 10^8 \text{\AA}^3 \quad (\text{C.5})$$

$$V_{\text{in}} = \frac{4}{3}\pi (R_0 - Db)^3 \approx 7.64 \times 10^7 \text{\AA}^3 \quad (\text{C.6})$$

$$N_{\text{SNARE}} = \frac{V_{\text{out}} - V_{\text{in}}}{V_{\text{lipid}}} R_{\text{protein/lipid}} \approx 43.61 \quad (\text{C.7})$$

³ Almog *et al.* (1990).

⁴ Parameters of DOPC rather than the lipid mixtures are used.

D.1 Attenuator parameters of the in-house diffractometer Rosi

Index	Attenuator status ^a	Thickness [μm]	Transmission (theoretical) ^b	Transmission (experimental)
0	0000	0	1.00	1.00
1	1000	24	0.34	0.36
2	0100	48	0.11	0.13
3	1100	24+48	3.74×10^{-2}	4.68×10^{-2}
4	0010	96	1.30×10^{-2}	1.53×10^{-2}
5	1010	24+96	4.42×10^{-3}	5.51×10^{-3}
6	0110	48+96	1.43×10^{-3}	1.99×10^{-3}
7	1110	24+48+96	5.92×10^{-4}	7.16×10^{-4}
8	0001	192	1.67×10^{-4}	2.54×10^{-4}
9	1001	24+192	5.68×10^{-5}	9.14×10^{-5}
10	0101	48+192	1.84×10^{-5}	3.30×10^{-5}
11	1101	24+48+192	6.40×10^{-6}	1.18×10^{-5}
12	0011	96+192	2.17×10^{-6}	3.91×10^{-6}
13	1011	24+96+192	7.38×10^{-7}	1.41×10^{-6}
14	0111	48+96+192	2.39×10^{-7}	5.08×10^{-7}
15	1111	24+48+96+192	8.12×10^{-8}	1.83×10^{-7}

^a 16 different transmission rates are achieved by combining 4 Cu foils with the thicknesses of 24, 48, 96 and 192 μm . 0 denotes the foil is out of position whereas 1 denotes the foil is in position.

^b Taken from http://henke.lbl.gov/optical_constants/filter2.html.

Bibliography

- [1] Leonid V. Chernomordik, Vadim A. Frolov, Eugenia Leikina, Peter Bronk, and Joshua Zimmerberg. The pathway of membrane fusion catalyzed by influenza hemagglutinin: restriction of lipids, hemifusion, and lipidic fusion pore formation. *J. Cell Biol.*, 140(6):1369–1382, 1998.
- [2] Paul M. Wassarman. Mammalian fertilization: Molecular aspects of gamete adhesion, exocytosis, and fusion. *Cell*, 96(2):175–183, 1999.
- [3] Reinhard Jahn and Thomas C. Südhof. Membrane fusion and exocytosis. *Annu. Rev. Biochem.*, 68(1):863–911, 1999.
- [4] J. M. White. Membrane fusion. *Science*, 258(5084):917–924, 1992.
- [5] Philip L. Yeagle. *The membranes of cells*. Academic Press, 2016.
- [6] Judith M. White. Viral and cellular membrane fusion proteins. *Annu. Rev. Physiol.*, 52(1):675–697, 1990.
- [7] Josep Rizo and Christian Rosenmund. Synaptic vesicle fusion. *Nat. Struct. Mol. Biol.*, 15:665–674, 2008.
- [8] Reinhard Jahn and Richard H. Scheller. SNAREs: engines for membrane fusion. *Nat. Rev. Mol. Cell Biol.*, 7(9):631–643, 2006.
- [9] Herre Jelger Risselada and Helmut Grubmüller. How SNARE molecules mediate membrane fusion: recent insights from molecular simulations. *Curr. Opin. Struct. Biol.*, 22(2):187–196, 2012.
- [10] Leonid V. Chernomordik and Michael M. Kozlov. Mechanics of membrane fusion. *Nat. Struct. Mol. Biol.*, 15(7):675–683, 2008.
- [11] M. M. Kozlov, S. L. Leikin, L. V. Chernomordik, V. S. Markin, and Y. A. Chizmadzhev. Stalk mechanism of vesicle fusion. *Eur. Biophys. J.*, 17(3):121–129, 1989.
- [12] Siewert J. Marrink and Alan E. Mark. The mechanism of vesicle fusion as revealed by molecular dynamics simulations. *J. Am. Chem. Soc.*, 125(37):11144–11145, 2003.
- [13] Lin Yang and Huey W. Huang. Observation of a membrane fusion intermediate structure. *Science*, 297(5588):1877–1879, 2002.
- [14] Barry R Lentz. Seeing is believing: the stalk intermediate. *Biophys. J.*, 91(8):2747–2748, 2006.
- [15] T. Salditt, C. Li, A. Spaar, and U. Mennicke. X-ray reflectivity of solid-supported multilamellar membranes. *Eur. Phys. J. E*, 7:105, 2002.
- [16] T. Salditt, M. Vogel, and W. Fenzl. Thermal fluctuations and positional correlations in

- oriented lipid membranes. *Phys. Rev. Lett.*, 90(17):178101–, 2003.
- [17] D. Constantin, U. Mennicke, C. Li, and T. Salditt. Solid-supported lipid multilayers: Structure factor and fluctuations. *Eur. Phys. J. E*, 12(2):283–290, 2003.
- [18] Jochen S. Hub, Tim Salditt, Maikel C. Rheinstädter, and Bert L. De Groot. Short-range order and collective dynamics of dmPC bilayers: a comparison between molecular dynamics simulations, x-ray, and neutron scattering experiments. *Biophys. J.*, 93(9):3156–3168, 2007.
- [19] S. Aeffner, T. Reusch, B. Weinhausen, , and T. Salditt. Membrane fusion intermediates and the effect of cholesterol: An in-house x-ray scattering study. *Eur. Phys. J. E*, 30:204–214, 2009.
- [20] Sajal Kumar Ghosh, Sebastian Aeffner, and Tim Salditt. Effect of PIP2 on bilayer structure and phase behavior of DOPC: An X-ray Scattering Study. *ChemPhysChem*, 12(14):2633–2640, 2011.
- [21] Sebastian Aeffner, Tobias Reusch, Britta Weinhausen, and Tim Salditt. Energetics of stalk intermediates in membrane fusion are controlled by lipid composition. *Proc. Natl. Acad. Sci. U.S.A.*, 109(25):E1609–E1618, 2012.
- [22] M. Seul and M.J. Sammon. Preparation of surfactant multilayer films on solid substrates by deposition from organic solution. *Thin Solid Films*, 185:287, 1990.
- [23] Walter Kauzmann. Some factors in the interpretation of protein denaturation. *Adv. Protein Chem.*, 14:1–63, 1959.
- [24] Lucas K. Tamm and SUREN A. Tatulian. Infrared spectroscopy of proteins and peptides in lipid bilayers. *Q. Rev. Biophys.*, 30:365–429, 11 1997.
- [25] Ziad Khattari, Sebastian Köhler, Yihui Xu, Sebastian Aeffner, and Tim Salditt. Stalk formation as a function of lipid composition studied by x-ray reflectivity. *BBA - Biomembranes*, 1848(1, Part A):41–50, 2015.
- [26] Burlyn E. Michel and Merrill R. Kaufmann. The osmotic potential of polyethylene glycol 6000. *Plant Physiol.*, 51(5):914–916, 1973.
- [27] JinKeun Lee and Barry R. Lentz. Evolution of lipidic structures during model membrane fusion and the relation of this process to cell membrane fusion. *Biochemistry*, 36(21):6251–6259, 1997.
- [28] Stephen W. Burgess, Thomas J. McIntosh, and Barry R. Lentz. Modulation of poly(ethylene glycol)-induced fusion by membrane hydration: importance of interbilayer separation. *Biochemistry*, 31(10):2653–2661, 1992.
- [29] Christopher B. Stanley and Helmut H. Strey. Measuring Osmotic Pressure of Poly(ethylene glycol) Solutions by Sedimentation Equilibrium Ultracentrifugation. *Macromolecules*, 36(18):6888–6893, 2003.
- [30] Matthew J. Wheeler, Silvia Russi, Michael G. Bowler, and Matthew W. Bowler. Measurement of the equilibrium relative humidity for common precipitant

- concentrations: facilitating controlled dehydration experiments. *Acta Crystallographica Section F*, 68(1):111–114, 2012.
- [31] Leonid Chernomordik. Non-bilayer lipids and biological fusion intermediates. *Chem. Phys. Lipids*, 81(2):203–213, 1996.
- [32] D. Papahadjopoulos, G. Poste, B.E. Schaeffer, and W.J. Vail. Membrane fusion and molecular segregation in phospholipid vesicles. *BBA - Biomembranes*, 352(1):10–28, 1974.
- [33] Lin Yang and Huey W. Huang. A rhombohedral phase of lipid containing a membrane fusion intermediate structure. *Biophys. J.*, 84(3):1808–1817, 2003.
- [34] U. Zimmermann. Electric field-mediated fusion and related electrical phenomena. *BBA - Reviews on Biomembranes*, 694(3):227–277, 1982.
- [35] P. R. Cullis and B. De Kruijff. Lipid polymorphism and the functional roles of lipids in biological membranes. *BBA - Reviews on Biomembranes*, 559(4):399–420, 1979.
- [36] D. Langevin. Micelles and microemulsions. *Annu. Rev. Phys. Chem.*, 43(1):341–369, 1992.
- [37] Sol M. Gruner. Intrinsic curvature hypothesis for biomembrane lipid composition: a role for nonbilayer lipids. *Proc. Natl. Acad. Sci. U.S.A.*, 82(11):3665–3669, 1985.
- [38] Derek Marsh. Intrinsic curvature in normal and inverted lipid structures and in membranes. *Biophys. J.*, 70(5):2248, 1996.
- [39] G. L. Kirk and S. M. Gruner. Lyotropic effects of alkanes and headgroup composition on the α -hii lipid liquid crystal phase transition: hydrocarbon packing versus intrinsic curvature. *Journal de Physique*, 46(5):761–769, 1985.
- [40] Z. Chen and R. P. Rand. The influence of cholesterol on phospholipid membrane curvature and bending elasticity. *Biophys. J.*, 73(1):267–276, 1997.
- [41] Chiho Hamai, Tinglu Yang, Sho Kataoka, Paul S. Cremer, and Siegfried M. Musser. Effect of average phospholipid curvature on supported bilayer formation on glass by vesicle fusion. *Biophys. J.*, 90(4):1241–1248, 2006.
- [42] Yonathan Kozlovsky and Michael M. Kozlov. Stalk model of membrane fusion: Solution of energy crisis. *Biophys. J.*, 82(2):882–895, 2002.
- [43] Jihong Bai, Ward C. Tucker, and Edwin R. Chapman. Pip2 increases the speed of response of synaptotagmin and steers its membrane-penetration activity toward the plasma membrane. *Nat. Struct. Mol. Biol.*, 11(1):36–44, 2004.
- [44] Guohua Lei and Robert C. MacDonald. Lipid bilayer vesicle fusion: Intermediates captured by high-speed microfluorescence spectroscopy. *Biophys. J.*, 85(3):1585–1599, 2003.
- [45] A. Portis, C. Newton, W. Pangborn, and D. Papahadjopoulos. Studies on the mechanism of membrane fusion: evidence for an intermembrane calcium (2+) ion-phospholipid complex, synergism with magnesium (2+) ion, and inhibition by spectrin. *Biochemistry*,

- 18(5):780–790, 1979.
- [46] Robert Fraley, Jan Wilschut, Nejat Duzgunes, Craig Smith, and Demetrios Papahadjopoulos. Studies on the mechanism of membrane fusion: role of phosphate in promoting calcium ion induced fusion of phospholipid vesicles. *Biochemistry*, 19(26):6021–6029, 1980.
- [47] M. Winterhalter and W. Helfrich. Bending elasticity of electrically charged bilayers: coupled monolayers, neutral surfaces, and balancing stresses. *J. Phys. Chem.*, 96(1):327–330, 1992.
- [48] Ken Jacobson, Ole G. Mouritsen, and Richard G. W. Anderson. Lipid rafts: at a crossroad between cell biology and physics. *Nat. Cell Biol.*, 9(1):7–14, 2007.
- [49] Norbert Kucerka, Stephanie Tristram-Nagle, and John Nagle. Structure of fully hydrated fluid phase lipid bilayers with monounsaturated chains. *J. Membr. Biol.*, 208(3):193–202, 2006.
- [50] W. Rawicz, K.C. Olbrich, T. McIntosh, D. Needham, and E. Evans. Effect of chain length and unsaturation on elasticity of lipid bilayers. *Biophys. J.*, 79(1):328–339, 2000.
- [51] Frederic Darios and Bazbek Davletov. Omega-3 and omega-6 fatty acids stimulate cell membrane expansion by acting on syntaxin 3. *Nature*, 440(7085):813–817, 2006.
- [52] Walter E. Teague, Nola L. Fuller, R. Peter Rand, and Klaus Gawrisch. Polyunsaturated lipids in membrane fusion events. *Cell. Mol. Biol. Lett.*, 7(2):262–264, 2002.
- [53] V. A. Parsegian, N. Fuller, and R. P. Rand. Measured work of deformation and repulsion of lecithin bilayers. *Proc. Natl. Acad. Sci. U.S.A.*, 76(6):2750–2754, 1979.
- [54] L. J. Lis, M. McAlister, N. Fuller, R. P. Rand, and V. A. Parsegian. Interactions between neutral phospholipid bilayer membranes. *Biophys. J.*, 37(3):657–665, 1982.
- [55] James Francis Young. Humidity control in the laboratory using salt solutions: a review. *Journal of Applied Chemistry*, 17(9):241–245, 1967.
- [56] S. Leikin, V. A. Parsegian, D. C. Rau, and R. P. Rand. Hydration forces. *Annu. Rev. Phys. Chem.*, 44(1):369–395, 1993.
- [57] Lewis Greenspan. Humidity fixed points of binary saturated aqueous solutions. *J. Res. Natl. Bur. Stand.*, 81(1):89–96, 1977.
- [58] V. Luzzati and F. Husson. The structure of the liquid-crystalline phases of lipid-water systems. *J. Cell Biol.*, 12(2):207–219, 1962.
- [59] Vittorio Luzzati, F. Reiss-Husson, E. Rivas, and T. Gulik-Krzywicki. Structure and polymorphism in lipid-water systems, and their possible biological implications. *Ann. N.Y. Acad. Sci.*, 137(2):409–413, 1966.
- [60] R. P. Rand, N. L. Fuller, S. M. Gruner, and V. A. Parsegian. Membrane curvature, lipid segregation, and structural transitions for phospholipids under dual-solvent stress. *Biochemistry*, 29(1):76–87, 1990.

- [61] Horia I. Petrache, Stephanie Tristram-Nagle, and John F. Nagle. Fluid phase structure of EPC and DMPC bilayers. *Chem. Phys. Lipids*, 95(1):83–94, 1998.
- [62] Barry R. Lentz. PEG as a tool to gain insight into membrane fusion. *EBJ*, 36(4-5):315–326, 2007.
- [63] Tobias Reusch. Nichtlamellare Strukturen in Lipidmembranstapeln in Abhängigkeit der Hydratisierung: Probenumgebung, Phasendiagramme und Bestimmung der Elektronendichte. Master's thesis, Institute for X-ray Physics, Georg-August University Göttingen, 2009.
- [64] Britta Weinhausen, Sebastian Aeffner, Tobias Reusch, and Tim Salditt. Acyl-chain correlation in membrane fusion intermediates: X-ray diffraction from the rhombohedral lipid phase. *Biophys. J.*, 102(9):2121–2129, 2012.
- [65] Sebastian Aeffner. *Stalk structures in lipid bilayer fusion studied by x-ray diffraction*. PhD thesis, Institute for X-ray Physics, Georg-August University Göttingen, 2011.
- [66] David Vaknin, Kristian Kjaer, Jens Als-Nielsen, and Mathias Lösche. Structural properties of phosphatidylcholine in a monolayer at the air/water interface: Neutron reflection study and reexamination of x-ray reflection measurements. *Biophys. J.*, 59(6):1325, 1991.
- [67] U. Mennicke, D. Constantin, and T. Salditt. Structure and interaction potentials in solid-supported lipid membranes studied by x-ray reflectivity at varied osmotic pressure. *Eur. Phys. J. E*, 20(2):221–230, 2006.
- [68] H. W. Huang, W. Liu, G. A. Olah, and Y. Wu. Physical techniques of membrane studies – study of membrane active peptides in bilayers. *Prog. Surf. Sci.*, 38(2):145–199, 1991.
- [69] C. R. Worthington, G. I. King, and T. J. McIntosh. Direct structure determination of multilayered membrane-type systems which contain fluid layers. *Biophys. J.*, 13(5):480, 1973.
- [70] C. R. Worthington. The determination of the first-order phase in membrane diffraction using electron density strip models. *J. Appl. Crystallogr.*, 14(6):387–391, 1981.
- [71] David C. Turner and Sol M. Gruner. X-ray diffraction reconstruction of the inverted hexagonal (hii) phase in lipid-water systems. *Biochemistry*, 31(5):1340–1355, 1992.
- [72] R.P. Rand and V.A. Parsegian. Hydration forces between phospholipid bilayers. *BBA - Biomembranes*, 988(3):351–376, 1989.
- [73] John F. Nagle and Stephanie Tristram-Nagle. Structure of lipid bilayers. *BBA - Reviews on Biomembranes*, 1469(3):159–195, 2000.
- [74] Klaus Gawrisch, V. Adrian Parsegian, Damian A. Hajduk, Mark W. Tate, Sol M. Gruner, Nola L. Fuller, and R. Peter Rand. Energetics of a hexagonal-lamellar-hexagonal-phase transition sequence in dioleoylphosphatidylethanolamine membranes. *Biochemistry*, 31(11):2856–2864, 1992.
- [75] M. M. Kozlov, S. Leikin, and R. P. Rand. Bending, hydration and interstitial energies quantitatively account for the hexagonal-lamellar-hexagonal reentrant phase transition

- in dioleoylphosphatidylethanolamine. *Biophys. J.*, 67(4):1603, 1994.
- [76] Mario Orsi and Jonathan W. Essex. Physical properties of mixed bilayers containing lamellar and nonlamellar lipids: insights from coarse-grain molecular dynamics simulations. *Faraday Discuss.*, 161:249–272, 2013.
- [77] Murray S. Webb, Sek Wen Hui, and Peter L. Steponkus. Dehydration-induced lamellar-to-hexagonal-ii phase transitions in DOPE/DOPC mixtures. *BBA - Biomembranes*, 1145(1):93–104, 1993.
- [78] Lin Yang, Lai Ding, and Huey W. Huang. New phases of phospholipids and implications to the membrane fusion problem. *Biochemistry*, 42(22):6631–6635, 2003.
- [79] Md. Emdadul Haque, Thomas J. McIntosh, and Barry R. Lentz. Influence of lipid composition on physical properties and PEG-mediated fusion of curved and uncurved model membrane vesicles, “nature’s own” fusogenic lipid bilayer. *Biochemistry*, 40(14):4340–4348, 2001.
- [80] Sergey M. Bezrukov. Functional consequences of lipid packing stress. *Curr. Opin. Colloid Interface Sci.*, 5(3-4):237–243, 2000.
- [81] Ignacio Tinoco, Kenneth Wang Sauer, and C. James. *Physical chemistry: principles and applications in biological sciences*. Number 544: 577 TIN. 1995.
- [82] Stefan Oelmeier, Florian Dismer, and Jurgen Hubbuch. Molecular dynamics simulations on aqueous two-phase systems - single peg-molecules in solution. *BMC Biophysics*, 5(1):14, 2012.
- [83] Masahito Yamazaki, Naoto Kashiwagi, Motoi Miyazu, and Tsutomu Asano. Effect of oligomers of ethylene glycol on thermotropic phase transition of dipalmitoylphosphatidylcholine multilamellar vesicles. *BBA - Biomembranes*, 1109(1):43–47, 1992.
- [84] Barry R. Lentz and Jinkeun Lee. Poly(ethylene glycol) (PEG)-mediated fusion between pure lipid bilayers: a mechanism in common with viral fusion and secretory vesicle release? (Review). *Mol. Membr. Biol.*, 16(4):279–296, 1999.
- [85] http://www.brocku.ca/researchers/peter_rand/osmotic/data/peg400temp.html.
- [86] E. Novakova, K. Giewekemeyer, and T. Salditt. Structure of two-component lipid membranes on solid support: An x-ray reflectivity study. *Phys. Rev. E*, 74:051911, 2006.
- [87] K. Hristova and S. H. White. Determination of the hydrocarbon core structure of fluid dioleoylphosphocholine (DOPC) bilayers by x-ray diffraction using specific bromination of the double-bonds: effect of hydration. *Biophys. J.*, 74(5):2419–2433, 1998.
- [88] Ulrike Rost, Yihui Xu, Tim Salditt, and Ulf Diederichsen. Heavy-atom labeled transmembrane β -peptides: Synthesis, cd-spectroscopy, and x-ray diffraction studies in model lipid multilayer. *ChemPhysChem*, 17:1–11, 2016.
- [89] Stephen H. White and William C. Wimley. Membrane protein folding and stability:

- Physical principles. *Annu. Rev. Biophys. Biomol. Struct.*, 28(1):319–365, 1999.
- [90] Kate L. Wegener and Iain D. Campbell. Transmembrane and cytoplasmic domains in integrin activation and protein-protein interactions (review). *Mol. Membr. Biol.*, 25(5):376–387, 2008.
- [91] Avner Fink, Neta Sal-Man, Doron Gerber, and Yechiel Shai. Transmembrane domains interactions within the membrane milieu: Principles, advances and challenges. *BBA - Biomembranes*, 1818(4):974–983, 2012.
- [92] R. Todd Armstrong, Anna S. Kushnir, and Judith M. White. The transmembrane domain of influenza hemagglutinin exhibits a stringent length requirement to support the hemifusion to fusion transition. *J. Cell Biol.*, 151(2):425–438, 2000.
- [93] Xue Han, Chih-Tien Wang, Jihong Bai, Edwin R. Chapman, and Meyer B. Jackson. Transmembrane Segments of Syntaxin Line the Fusion Pore of Ca²⁺-Triggered Exocytosis. *Science*, 304(5668):289–292, 2004.
- [94] D. Langosch, M. Hofmann, and C. Ungermann. The role of transmembrane domains in membrane fusion. *Cell. Mol. Life Sci.*, 64(7):850–, 2007.
- [95] Patrick Lagüe, Martin J Zuckermann, and Benoit Roux. Lipid-mediated interactions between intrinsic membrane proteins: dependence on protein size and lipid composition. *Biophys. J.*, 81(1):276–284, 2001.
- [96] Dahui Liu and William F DeGrado. De novo design, synthesis, and characterization of antimicrobial β -peptides. *J. Am. Chem. Soc.*, 123(31):7553–7559, 2001.
- [97] Pradip Chakraborty and Ulf Diederichsen. Three-dimensional organization of helices: Design principles for nucleobase-functionalized β -peptides. *Chem. Eur. J.*, 11(11):3207–3216, 2005.
- [98] Arndt M. Brückner, Margarita Garcia, Andrew Marsh, Samuel H. Gellman, and Ulf Diederichsen. Synthesis of Novel Nucleo- β -Amino Acids and Nucleobase-Functionalized β -Peptides. *Eur. J. Org. Chem.*, 2003(18):3555–3561, 2003.
- [99] Dieter Seebach, Mark Overhand, Florian N. M. Kühnle, Bruno Martinoni, Lukas Oberer, Ulrich Hommel, and Hans Widmer. β -Peptides: Synthesis by Arndt-Eistert homologation with concomitant peptide coupling. Structure determination by NMR and CD spectroscopy and by X-ray crystallography. Helical secondary structure of a β -hexapeptide in solution and its stability towards pepsin. *Helv. Chim. Acta*, 79(4):913–941, 1996.
- [100] Dieter Seebach and James Gardiner. β -peptidic peptidomimetics. *Acc. Chem. Res.*, 41(10):1366–1375, 2008.
- [101] Philipp E. Schneggenburger, Andre Beerlink, Brigitte Worbs, Tim Salditt, and Ulf Diederichsen. A novel heavy-atom label for side-specific peptide iodination: Synthesis, membrane incorporation and x-ray reflectivity. *ChemPhysChem*, 10(9-10):1567–1576, 2009.

- [102] Andrea Kuesel, Ziad Khattari, Philipp E Schneggenburger, Arnab Banerjee, Tim Salditt, and Ulf Diederichsen. Conformation and interaction of a d,l-alternating peptide with a bilayer membrane: X-ray reflectivity, cd, and ftir spectroscopy. *ChemPhysChem*, 8(16):2336–2343, 2007.
- [103] Philipp Schneggenburger, Andre Beerlink, Britta Weinhausen, Tim Salditt, and Ulf Diederichsen. Peptide model helices in lipid membranes: insertion, positioning, and lipid response on aggregation studied by x-ray scattering. *Eur. Biophys. J.*, 40(4):417–436, 2011.
- [104] U. Rost, C. Steinem, and U. Diederichsen. β -glutamine-mediated self-association of transmembrane β -peptides within lipid bilayers. *Chemical Science*, 2016.
- [105] Antonina S. Lygina, Karsten Meyenberg, Reinhard Jahn, and Ulf Diederichsen. Transmembrane domain peptide/peptide nucleic acid hybrid as a model of a SNARE protein in vesicle fusion. *Angew. Chem. Int. Ed.*, 50(37):8597–8601, 2011.
- [106] Ayumi Kashiwada, Iori Yamane, Mana Tsuboi, Shun Ando, and Kiyomi Matsuda. Design, construction, and characterization of high-performance membrane fusion devices with target-selectivity. *Langmuir*, 28(4):2299–2305, 2012.
- [107] Jan-Dirk Wehland, Antonina S. Lygina, Pawan Kumar, Samit Guha, Barbara E. Hubrich, Reinhard Jahn, and Ulf Diederichsen. Role of the transmembrane domain in SNARE protein mediated membrane fusion: peptide nucleic acid/peptide model systems. *Mol. BioSyst.*, 12:2770–2776, 2016.
- [108] Gudrun Stengel, Raphael Zahn, and Fredrik Höök. Dna-induced programmable fusion of phospholipid vesicles. *J. Am. Chem. Soc.*, 129(31):9584–9585, 2007.
- [109] Yee-Hung M. Chan, Bettina van Lengerich, and Steven G. Boxer. Effects of linker sequences on vesicle fusion mediated by lipid-anchored DNA oligonucleotides. *Proc. Natl. Acad. Sci. U.S.A.*, 106(4):979–984, 2009.
- [110] Dieter Seebach and Jennifer L Matthews. β -peptides: a surprise at every turn. *Chem. Commun.*, (21):2015–2022, 1997.
- [111] Ulrich Koert. β -peptides: Novel secondary structures take shape. *Angewandte Chemie International Edition in English*, 36(17):1836–1837, 1997.
- [112] Daniel H. Appella, Laurie A. Christianson, Isabella L. Karle, Douglas R. Powell, and Samuel H. Jen Gellman. β -peptide foldamers: robust helix formation in a new family of β -amino acid oligomers. *J. Am. Chem. Soc.*, 118(51):13071–13072, 1996.
- [113] Richard P. Cheng, Samuel H. Gellman, and William F. DeGrado. β -peptides: From structure to function. *Chem. Rev.*, 101(10):3219–3232, October 2001.
- [114] Jens Frackenkohl, Per I. Arvidsson, Jörg V. Schreiber, and Dieter Seebach. The outstanding biological stability of β - and γ -peptides toward proteolytic enzymes: an in vitro investigation with fifteen peptidases. *ChemBioChem*, 2(6):445–455, 2001.
- [115] Karl Gademann, Tobias Hintermann, and Jurg V. Schreiber. Beta-peptides: twisting and

- turning. *Curr. Med. Chem.*, 6(10):905–925, 1999.
- [116] Magnus Rueping, Yogesh R. Mahajan, Bernhard Jaun, and Dieter Seebach. Design, synthesis and structural investigations of a β -peptide forming a 314-helix stabilized by electrostatic interactions. *Chem. Eur. J.*, 10(7):1607–1615, 2004.
- [117] Kelly Helen Anderson. *The Synthesis and Surface Studies of β -Amino Acids & β -Peptides*. PhD thesis, University of Canterbury. Chemistry, 2007.
- [118] Maurits R. R. de Planque, John A. W. Kruijtzter, Rob M. J. Liskamp, Derek Marsh, Denise V. Greathouse, Roger E. Koeppe, Ben de Kruijff, and J. Antoinette Killian. Different membrane anchoring positions of tryptophan and lysine in synthetic transmembrane α -helical peptides. *J. Biol. Chem.*, 274(30):20839–20846, 1999.
- [119] Ulrike Rost. *ORGANISATION AND RECOGNITION OF ARTIFICIAL TRANSMEMBRANE PEPTIDES*. PhD thesis, Institute of Organic and Biomolecular Chemistry, Georg-August University Goettingen, 2016.
- [120] Gilles Guichard, Stefan Abele, and Dieter Seebach. Preparation of n-fmoc-protected β 2- and β 3-amino acids and their use as building blocks for the solid-phase synthesis of β -peptide. *Helv. Chim. Acta*, 81(2):187–206, 1998.
- [121] Dominik Wernic, John DiMaio, and Julian Adams. Enantiospecific synthesis of l.-alpha.-aminosuberic acid. synthetic applications in preparation of atrial natriuretic factor analogs. *J. Org. Chem.*, 54(17):4224–4228, 1989.
- [122] Caline Douat, Annie Heitz, Jean Martinez, and Jean-Alain Fehrentz. Stereoselective synthesis of allyl- and homoallylglycines. *Tetrahedron Lett.*, 42(19):3319–3321, 2001.
- [123] Giuseppina Sabatino and Anna M. Papini. Advances in automatic, manual and microwave-assisted solid-phase peptide synthesis. *Curr. Opin. Drug Discov. Devel.*, 11(6):762–770, 2008.
- [124] Jean-Christophe Meillon and Normand Voyer. A synthetic transmembrane channel active in lipid bilayers. *Angewandte Chemie International Edition in English*, 36(9):967–969, 1997.
- [125] J. Antoinette Killian and Gunnar von Heijne. How proteins adapt to a membrane/water interface. *Trends Biochem. Sci.*, 25(9):429–434, 2000.
- [126] Maurits R. R. de Planque, Boyan B. Bonev, Jeroen A. A. Demmers, Denise V. Greathouse, Roger E. Koeppe, Frances Separovic, Anthony Watts, and J. Antoinette Killian. Interfacial anchor properties of tryptophan residues in transmembrane peptides can dominate over hydrophobic matching effects in peptide-lipid interactions. *Biochemistry*, 42(18):5341–5348, 2003.
- [127] Robert C. MacDonald, Ruby I. MacDonald, Bert Ph. M. Menco, Keizo Takeshita, Nanda K. Subbarao, and Lan-rong Hu. Small-volume extrusion apparatus for preparation of large, unilamellar vesicles. *BBA - Biomembranes*, 1061(2):297–303, 1991.
- [128] F. D. Sonnichsen, J. E. Van Eyk, R. S. Hodges, and B. D. Sykes. Effect of trifluoroethanol on

- protein secondary structure: an NMR and CD study using a synthetic actin peptide. *Biochemistry*, 31(37):8790–8798, 1992.
- [129] John T. Pelton and Larry R. McLean. Spectroscopic methods for analysis of protein secondary structure. *Anal. Biochem.*, 277(2):167–176, 2000.
- [130] Henry E. Auer. Far-ultraviolet absorption and circular dichroism spectra of L-tryptophan and some derivatives. *J. Am. Chem. Soc.*, 95(9):3003–3011, 1973.
- [131] William T. Heller, Alan J. Waring, Robert I. Lehrer, Thad A. Harroun, Thomas M. Weiss, Lin Yang, and Huey W. Huang. Membrane thinning effect of the β -sheet antimicrobial protegrin. *Biochemistry*, 39(1):139–145, 1999.
- [132] D. Constantin, G. Brotons, A. Jarre, C. Li, and T. Salditt. Interaction of Alamethicin Pores in DMPC Bilayers. *Biophys. J.*, 92(11):3978–3987, 2007.
- [133] Tim Salditt, Chenghao Li, and Alexander Spaar. Structure of antimicrobial peptides and lipid membranes probed by interface-sensitive x-ray scattering. *BBA - Biomembranes*, 1758(9):1483–1498, 2006.
- [134] Y. Wu, K. He, S. J. Ludtke, and H. W. Huang. X-ray diffraction study of lipid bilayer membranes interacting with amphiphilic helical peptides: diphytanoyl phosphatidylcholine with alamethicin at low concentrations. *Biophys. J.*, 68:2361, 1995.
- [135] Huey W. Huang. Action of Antimicrobial Peptides: Two-State Model. *Biochemistry*, 39(29):8347–8352, 2000.
- [136] William T. Heller, Alan J. Waring, Robert I. Lehrer, and Huey W. Huang. Multiple states of β -sheet peptide protegrin in lipid bilayers. *Biochemistry*, 37(49):17331–17338, 1998.
- [137] J. Antoinette Killian. Hydrophobic mismatch between proteins and lipids in membranes. *BBA - Reviews on Biomembranes*, 1376(3):401–416, 1998.
- [138] Z. Khattari, G. Brotons, E. Arbely, I. T. Arkin, T. H. Metzger, and T. Salditt. SARS E protein in phospholipid bilayers: an anomalous X-ray reflectivity study. *Physica B: Condensed Matter*, 357:34–38, 2005.
- [139] Alexander Spaar and Tim Salditt. Short Range Order of Hydrocarbon Chains in Fluid Phospholipid Bilayers Studied by X-Ray Diffraction from Highly Oriented Membranes. *Biophys. J.*, 85(3):1576–1584, 2003.
- [140] Alexander Spaar, Christian Münster, and Tim Salditt. Conformation of peptides in lipid membranes studied by x-ray grazing incidence scattering. *Biophys. J.*, 87(1):396–407, 2004.
- [141] William S. Trimble, David M. Cowan, and Richard H. Scheller. VAMP-1: a synaptic vesicle-associated integral membrane protein. *Proc. Natl. Acad. Sci. U.S.A.*, 85(12):4538–4542, 1988.
- [142] Phyllis I. Hanson, John E. Heuser, and Reinhard Jahn. Neurotransmitter release - four years of SNARE complexes. *Curr. Opin. Neurobiol.*, 7(3):310–315, 1997.

- [143] Thomas Söllner, Sidney W. Whiteheart, Michael Brunner, Hediye Erdjument-Bromage, Scott Geromanos, Paul Tempst, and James E. Rothman. SNAP receptors implicated in vesicle targeting and fusion. *Nature*, 362(6418):318–324, 1993.
- [144] Thomas Söllner, Mark K. Bennett, Sidney W. Whiteheart, Richard H. Scheller, and James E. Rothman. A protein assembly-disassembly pathway in vitro that may correspond to sequential steps of synaptic vesicle docking, activation, and fusion. *Cell*, 75(3):409–418, 1993.
- [145] Yukiko Goda. SNAREs and regulated vesicle exocytosis. *Proc. Natl. Acad. Sci. U.S.A.*, 94(3):769–772, 1997.
- [146] Yu A. Chen and Richard H. Scheller. Snare-mediated membrane fusion. *Nat. Rev. Mol. Cell Biol.*, 2(2):98–106, 2001.
- [147] Jeffrey F. Ellena, Binyong Liang, Maciej Wiktor, Alexander Stein, David S. Cafiso, Reinhard Jahn, and Lukas K. Tamm. Dynamic structure of lipid-bound synaptobrevin suggests a nucleation-propagation mechanism for trans-snare complex formation. *Proc. Natl. Acad. Sci. U.S.A.*, 106(48):20306–20311, 2009.
- [148] Ajaybabu V. Pobbati, Alexander Stein, and Dirk Fasshauer. N- to c-terminal snare complex assembly promotes rapid membrane fusion. *Science*, 313(5787):673–676, 2006.
- [149] Thomas Weber, Boris V. Zemelman, James A. McNew, Benedikt Westermann, Michael Gmachl, Francesco Parlati, Thomas H. Söllner, and James E. Rothman. SNAREpins: Minimal Machinery for Membrane Fusion. *Cell*, 92(6):759–772, 1998.
- [150] Dirk Fasshauer, Henning Otto, William K. Eliason, Reinhard Jahn, and Axel T. Brünger. Structural changes are associated with soluble n-ethylmaleimide-sensitive fusion protein attachment protein receptor complex formation. *J. Biol. Chem.*, 272(44):28036–28041, 1997.
- [151] R. Bryan Sutton, Dirk Fasshauer, Reinhard Jahn, and Axel T. Brünger. Crystal structure of a snare complex involved in synaptic exocytosis at 2.4 resolution. *Nature*, 395(6700):347–353, 1998.
- [152] Mathias Winterhalter. Black lipid membranes. *Curr. Opin. Colloid Interface Sci.*, 5:250–255, 2000.
- [153] Jan Wilschut and Dick Hoekstra. Special issue: Liposomes/membrane fusion: Lipid vesicles as a model system. *Chem. Phys. Lipids*, 40(2):145–166, 1986.
- [154] Abhinav Nath, William M. Atkins, and Stephen G. Sligar. Applications of phospholipid bilayer nanodiscs in the study of membranes and membrane proteins. *Biochemistry*, 46(8):2059–2069, 2007.
- [155] Adrienne A. Brian and Harden M. McConnell. Allogeneic stimulation of cytotoxic t cells by supported planar membranes. *Proc. Natl. Acad. Sci. U.S.A.*, 81(19):6159–6163, 1984.
- [156] E. Novakova, G. Mitrea, C. Peth, J. Thieme, K. Mann, and T. Salditt. Solid supported multicomponent lipid membranes studied by x-ray spectromicroscopy. *Biointerphases*,

- 3:44–54, 2008.
- [157] Yee-Hung M Chan and Steven G Boxer. Model membrane systems and their applications. *Curr. Opin. Chem. Biol.*, 11(6):581–587, 2007.
- [158] E. Sackmann. Supported membranes: Scientific and practical applications. *Science*, 271:43, 1996.
- [159] Yulia Lyatskaya, Yufeng Liu, Stephanie Tristram-Nagle, John Katsaras, and John F. Nagle. Method for obtaining structure and interactions from oriented lipid bilayers. *Phys. Rev. E*, 63:011907, 2000.
- [160] N. Bunjes, E. K. Schmidt, A. Jonczyk, F. Rippmann, D. Beyer, H. Ringsdorf, P. Gräber, W. Knoll, and R. Naumann. Thiopeptide-supported lipid layers on solid substrates. *Langmuir*, 13(23):6188–6194, 1997.
- [161] Norbert Kucerka, Jeremy Pencer, Jonathan N. Sachs, John F. Nagle, and John Katsaras. Curvature effect on the structure of phospholipid bilayers. *Langmuir*, 23(3):1292–1299, 2007.
- [162] Loraine Silvestro and Paul H. Axelsen. Infrared spectroscopy of supported lipid monolayer, bilayer, and multibilayer membranes. *Chem. Phys. Lipids*, 96:69–80, 1998.
- [163] Gareth Roberts, editor. *Langmuir-Blodgett Films*. Springer Science&Business Media LLC, 1990.
- [164] Claudio Nicolini, Victor Erokhin, Francesco Antolini, Paolo Catasti, and Paolo Facci. Thermal stability of protein secondary structure in langmuir-blodgett films. *BBA - General Subjects*, 1158(3):273–278, 1993.
- [165] J. B. Peng, M. Prakash, R. Macdonald, Pulak. Dutta, and J. B. Ketterson. Formation of multilayers of dipalmitoylphosphatidylcholine using the langmuir-blodgett technique. *Langmuir*, 3(6):1096–1097, 1987.
- [166] Stephanie A. Tristram-Nagle. Preparation of Oriented, Fully Hydrated Lipid Samples for Structure Determination Using X-Ray Scattering. In AlexM. Dopico, editor, *Methods Molecular Biology*, volume 400, pages 63–75. Humana Press, 2007.
- [167] U. P. Fringeli and Hs. H. Günthard. *Infrared Membrane Spectroscopy*, pages 270–332. Springer Berlin Heidelberg, Berlin, Heidelberg, 1981.
- [168] Chenghao Li, Doru Constantin, and Tim Salditt. Biomimetic membranes of lipid-peptide model systems prepared on solid support. *J. Phys.: Condens. Matter*, 16(26):S2439–S2453, 2004.
- [169] Ewa Goreckac Damian Pociachac Edward Rojc Adrianna Slawinska-Brychd Mariusz Gagosa Marta Arczewskaa, Daniel M. Kaminska. The molecular organization of prenylated flavonoid xanthohumol in DPPC multibilayers: X-ray diffraction and FTIR spectroscopic studies. *BBA - Biomembranes*, 1828(2):213–222, 2013.
- [170] Erik Goormaghtigh, Veronique Cabiaus, and Jean-Marie Ruyschaert. Secondary structure and dosage of soluble and membrane proteins by attenuated total reflection

- Fourier-transform infrared spectroscopy on hydrated films. *Eur. J. Biochem*, 193:420, 1990.
- [171] Edwin Kalb, Sammy Frey, and Lukas K. Tamm. Formation of supported planar bilayers by fusion of vesicles to supported phospholipid monolayers. *BBA - Biomembranes*, 1103(2):307–316, 1992.
- [172] Lando L. G. Schwenen, Raphael Hubrich, Dragomir Milovanovic, Burkhard Geil, Jian Yang, Alexander Kros, Reinhard Jahn, and Claudia Steinem. Resolving single membrane fusion events on planar pore-spanning membranes. *Scientific Reports*, 5:12006, 2015.
- [173] Dirk Fasshauer, R. Bryan Sutton, Axel T. Brunger, and Reinhard Jahn. Conserved structural features of the synaptic fusion complex: SNARE proteins reclassified as Q-and R-SNAREs. *Proc. Natl. Acad. Sci. U.S.A.*, 95(26):15781–15786, 1998.
- [174] Alexander Stein, Anand Radhakrishnan, Dietmar Riedel, Dirk Fasshauer, and Reinhard Jahn. Synaptotagmin activates membrane fusion through a Ca²⁺-dependent trans interaction with phospholipids. *Nat. Struct. Mol. Biol.*, 14(10):904–911, 2007.
- [175] Geert van den Bogaart, Matthew G Holt, Gertrude Bunt, Dietmar Riedel, Fred S Wouters, and Reinhard Jahn. One snare complex is sufficient for membrane fusion. *Nat. Struct. Mol. Biol.*, 17(3):358–364, 2010.
- [176] Javier Matias Hernandez. *Reconstituted SNARE-mediated fusion: Towards a mechanistic understanding*. PhD thesis, Georg-August-Universität-Göttingen, 2012.
- [177] Javier M. Hernandez, Alex J. B. Kreuzberger, Volker Kiessling, and Reinhard Tamm, Lukas K. and Jahn. Variable cooperativity in snare-mediated membrane fusion. *Proc. Natl. Acad. Sci. U.S.A.*, 111(33):12037–12042, 2014.
- [178] M. R. Wenk, T. Alt, A. Seelig, and J. Seelig. Octyl-beta-d-glucopyranoside partitioning into lipid bilayers: thermodynamics of binding and structural changes of the bilayer. *Biophys. J.*, 72(4):1719–1731, 1997.
- [179] Ralf P Richter, Rémi Bérat, and Alain R. Brisson. Formation of solid-supported lipid bilayers: An integrated view. *Langmuir*, 22(8):3497–3505, 2006.
- [180] P. Pernot, A. Round, R. Barrett, A. De Maria Antolinos, A. Gobbo, E. Gordon, J. Huet, J. Kieffer, M. Lentini, M. Mattenet, C. Morawe, C. Mueller-Dieckmann, S. Ohlsson, W. Schmid, J. Surr, P. Theveneau, L. Zerrad, and S. McSweeney. Upgraded ESRF BM29 beamline for SAXS on macromolecules in solution. *J. Synchrotron Rad.*, 20:660–664, 2013.
- [181] Adam Round, Franck Felisaz, Lukas Fodinger, Alexandre Gobbo, Julien Huet, Cyril Villard, Clement E. Blanchet, Petra Pernot, Sean McSweeney, Manfred Roessle, Dmitri I Svergun, and Florent Cipriani. BioSAXS Sample Changer: a robotic sample changer for rapid and reliable high-throughput X-ray solution scattering experiments. *Acta Crystallogr. Sect. D: Bio. Crystallogr.*, 71:67–75, 2014.
- [182] http://www.esrf.eu/home/UsersAndScience/Experiments/MX/About_our_beamlines/bm29/beamline-setup/sample-changer.html.

- [183] P Pernot, P Theveneau, T Giraud, R. Nogueira Fernandes, D. Nurizzo, D. Spruce, J. Surr, S. McSweeney, A. Round, Felisaz F, L. Foedinger, A. Gobbo, J. Huet, C. Villard, and F Cipriani. New beamline dedicated to solution scattering from biological macromolecules at the ESRF. *J. Phys: Conf. Ser.*, 247:012009–, 2010.
- [184] Marie Françoise Incardona, Gleb P. Bourenkov, Karl Levik, Romeu A. Pieritz, Alexander N. Popov, and Olof Svensson. EDNA: a framework for plugin-based applications applied to x-ray experiment online data analysis. *J. Synchrotron Rad.*, 16(6):872–879, Nov 2009.
- [185] <https://www.esrf.fr/ispyb/security/logon.do>.
- [186] O. Glatter and O. Kratky, editors. *Small Angle X-ray Scattering*. Academic Press Inc. (London) LTD, 1982.
- [187] W. Ehrenberg and A. Franks. Small-angle x-ray scattering. *Nature*, 170(4338):1076–1077, 1952.
- [188] J. Als-Nielsen. *Elements of Modern X-Ray Physics*. Wiley, 2001.
- [189] Pablo Székely, Avi Ginsburg, Tal Ben-Nun, and Uri Raviv. Solution x-ray scattering form factors of supramolecular self-assembled structures. *Langmuir*, 26(16):13110–13129, 2010.
- [190] Doris Orthaber, Alexander Bergmann, and Otto Glatter. SAXS experiments on absolute scale with Kratky systems using water as a secondary standard. *J. Appl. Crystallogr.*, 33(2):218–225, 2000.
- [191] Efstratios Mylonas and Dmitri I. Svergun. Accuracy of molecular mass determination of proteins in solution by small-angle X-ray scattering. *Journal of Applied Crystallography*, 40:s245–s249, 2007.
- [192] Mary Luckey. *Membrane Structural Biology: With Biochemical and Biophysical Foundations*. Cambridge University Press, 2014.
- [193] Charles Tanford. Micelle shape and size. *The Journal of Physical Chemistry*, 76(21):3020–3024, 1972.
- [194] Rémi Lazzari. *IsGISAXS*: a program for grazing-incidence small-angle X-ray scattering analysis of supported islands. *J. Appl. Crystallogr.*, 35(4):406–421, Aug 2002.
- [195] A. Guinier and G. Fournet. *Small angle scattering of x-rays*. J. Wiley & Sons, New York, 1955.
- [196] Jan Lipfert, Linda Columbus, Vincent B. Chu, Scott A. Lesley, and Sebastian Doniach. Size and shape of detergent micelles determined by small-angle x-ray scattering. *J. Phys. Chem. B*, 111(43):12427–12438, 2007.
- [197] Ryan C. Oliver, Jan Lipfert, Daniel A. Fox, Ryan H. Lo, Sebastian Doniach, and Linda Columbus. Dependence of micelle size and shape on detergent alkyl chain length and head group. *PLoS One*, 8(5):e62488, 2013.
- [198] Jan Skov Pedersen. Analysis of small-angle scattering data from colloids and polymer

- solutions: modeling and least-squares fitting. *Adv. Colloid Interface Sci.*, 70:171–210, 1997.
- [199] Simon Castorph. *Synapti Vesicles Studied by Small-Angle X-Ray Sattering*. PhD thesis, Georg-August-Universität Göttingen, 2010.
- [200] Ruitian Zhang, Palma Ann Marone, P. Thiyagarajan, and David M. Tiede. Structure and molecular fluctuations of n-alkyl- β -d-glucopyranoside micelles determined by x-ray and neutron scattering. *Langmuir*, 15(22):7510–7519, October 1999.
- [201] Michel Ollivon, Ofer Eidelman, Robert Blumenthal, and Anne Walter. Micelle-vesicle transition of egg phosphatidylcholine and octyl glucoside. *Biochemistry*, 27(5):1695–1703, 1988.
- [202] S Almog, BJ Litman, W Wimley, J Cohen, EJ Wachtel, Y Barenholz, A Ben-Shaul, and D Lichtenberg. States of aggregation and phase transformations in mixtures of phosphatidylcholine and octyl glucoside. *Biochemistry*, 29(19):4582–4592, 1990.
- [203] Grethe Vestergaard Jensen, Reidar Lund, JÃ©mie Gummel, Michael Monkenbusch, Theyencheri Narayanan, and Jan Skov Pedersen. Direct observation of the formation of surfactant micelles under nonisothermal conditions by synchrotron saxs. *J. Am. Chem. Soc.*, 135(19):7214–7222, May 2013.
- [204] Michael R. Brzustowicz and Axel T. Brunger. X-ray scattering from unilamellar lipid vesicles. *J. Appl. Crystallogr.*, 38(1):126–131, Feb 2005.
- [205] Georg Pabst, Michael Rappolt, Heinz Amenitsch, and Peter Laggner. Structural information from multilamellar liposomes at full hydration: Full q-range fitting with high quality x-ray data. *Phys. Rev. E*, 62(3):4000–4009, 2000.
- [206] J.A. Bouwstra, G.S. Gooris, W. Bras, and H. Talsma. Small angle x-ray scattering: possibilities and limitations in characterization of vesicles. *Chem. Phys. Lipids*, 64(1):83–98, 1993.
- [207] Helmut Hauser. Some aspects of the phase behaviour of charged lipids. *BBA - Biomembranes*, 772(1):37–50, 1984.
- [208] Frederick de Meyer and Berend Smit. Effect of cholesterol on the structure of a phospholipid bilayer. *Proc. Natl. Acad. Sci. U.S.A.*, 106(10):3654–3658, 2009.
- [209] Borislav Angelov, Michel Ollivon, and Angelina Angelova. X-ray diffraction study of the effect of the detergent octyl glucoside on the structure of lamellar and nonlamellar lipid/water phases of use for membrane protein reconstitution. *Langmuir*, 15(23):8225–8234, 1999.
- [210] Perttu Niemelä, Marja T. Hyvönen, and Ilpo Vattulainen. Structure and dynamics of sphingomyelin bilayer: Insight gained through systematic comparison to phosphatidylcholine. *Biophys. J.*, 87(5):2976–2989, 2004.
- [211] Stuart McLaughlin, Jiyao Wang, Alok Gambhir, and Diana Murray. PIP2 and proteins: interactions, organization, and information flow. *Annu. Rev. Biophys. Biomol. Struct.*,

- 31(1):151–175, 2002.
- [212] Stuart McLaughlin. The electrostatic properties of membranes. *Annu. Rev. Biophys. Biophys. Chem.*, 18(1):113–136, 1989.
- [213] I. Levental, P.A. Janmey, and A. Cēbers. Electrostatic contribution to the surface pressure of charged monolayers containing polyphosphoinositide s. *Biophys. J.*, 95(3):1199–1205, 2008.
- [214] S. G. A. McLaughlin, G. Szabo, and G. Eisenman. Divalent ions and the surface potential of charged phospholipid membranes. *The Journal of General Physiology*, 58(6):667–687, 1971.
- [215] Marta K. Domanska, Volker Kiessling, Alexander Stein, Dirk Fasshauer, and Lukas K. Tamm. Single vesicle millisecond fusion kinetics reveals number of SNARE complexes optimal for fast SNARE-mediated membrane fusion. *J. Biol. Chem.*, 284(46):32158–32166, 2009.
- [216] J. Lasch, J. Hoffman, W. G. Omelyanenko, A. A. Klivanov, V. P. Torchilin, H. Binder, and K. Gawrisch. Interaction of triton x-100 and octyl glucoside with liposomal membranes at sublytic and lytic concentrations. spectroscopic studies. *BBA - Biomembranes*, 1022(2):171–180, 1990.
- [217] Terence Allen. *Powder sampling and particle size determination*. Elsevier, 2003.
- [218] Michael J. Skaug, Marjorie L. Longo, and Roland Faller. The impact of texas red on lipid bilayer properties. *J. Phys. Chem. B*, 115(26):8500–8505, 2011.
- [219] Michael J. Skaug, Marjorie L. Longo, and Roland Faller. Computational Studies of Texas Red 1,2-Dihexadecanoyl-sn-glycero-3-phosphoethanolamine Model Building and Applications. *The Journal of Physical Chemistry B*, 113(25):8758–8766, 2009.
- [220] Wim H De Jeu. *Basic X-Ray Scattering for Soft Matter*. Oxford University Press, 2016.
- [221] John F Nagle, Kiyotaka Akabori, Bradley W Treece, and Stephanie Tristram-Nagle. Determination of mosaicity in oriented stacks of lipid bilayers. *Soft Matter*, 12:1884–1891, 2016.
- [222] J.F. Nagle, R. Zhang, S. Tristram-Nagle, W. Sun, H.I. Petrache, and R.M. Suter. X-ray structure determination of fully hydrated l alpha phase dipalmitoylphosphatidylcholine bilayers. *Biophys. J.*, 70(3):1419–1431, 1996.
- [223] Lobat Tayebi, Yicong Ma, Daryoosh Vashaee, Gang Chen, Sunil K. Sinha, and Atul N. Parikh. Long-range interlayer alignment of intralayer domains in stacked lipid bilayers. *Nat. Mater.*, 11(12):1074–1080, 2012.
- [224] David R. Nelson. *Defects and geometry in condensed matter physics*. Cambridge University Press, 2002.
- [225] Frederik Nilsson and Olle Söderman. Physical-Chemical Properties of the n-Octyl β -d-Glucoside/Water System. A Phase Diagram, Self-Diffusion NMR, and SAXS Study. *Langmuir*, 12(4):902–908, 1996.

-
- [226] Annela M. Seddon, Paul Curnow, and Paula J. Booth. Membrane proteins, lipids and detergents: not just a soap opera. *BBA - Biomembranes*, 1666(1):105–117, 2004.
- [227] Xiangbing Zeng, Goran Ungar, Yongsong Liu, Virgil Percec, Andres E. Dulcey, and Jamie K. Hobbs. Supramolecular dendritic liquid quasicrystals. *Nature*, 428(6979):157–160, 2004.
- [228] Ying Feng, Dominique Rainteau, Claude Chachaty, Zhi-Wu Yu, Claude Wolf, and Peter J. Quinn. Characterization of a quasicrystalline phase in codispersions of phosphatidylethanolamine and glucocerebroside. *Biophys. J.*, 86(4):2208–2217, 2004.
- [229] Charlotte E. Conn, Connie Darmanin, Xavier Mulet, Adrian Hawley, and Calum J. Drummond. Effect of lipid architecture on cubic phase susceptibility to crystallisation screens. *Soft Matter*, 8:6884–6896, 2012.
- [230] Pawan Kumar, Samit Guha, and Ulf Diederichsen. SNARE protein analog-mediated membrane fusion. *J. Pept. Sci.*, 21(8):621–629, 2015.

Own publications

1. Z. Khattari, S. Köhler, Y. Xu, S. Äffner and T. Salditt. Stalk formation as a function of lipid composition studied by x-ray reflectivity. *BBA-Biomembranes* (2015).
2. U. Rost¹, Y. Xu¹, T. Salditt and U. Diederichsen. Heavy-Atom Labeled Transmembrane β -Peptides: Synthesis, CD-Spectroscopy, and X-ray Diffraction Studies in Model Lipid Multilayer. *ChemPhysChem* (2016).
3. Y. Xu, J. Kuhlmann, M. Brennich, K. Komorowski, R. Jahn, C. Steinem and T. Salditt. Reconstitution of SNARE proteins into solid-supported lipid bilayer stacks and x-ray structure analysis. *BBA-Biomembranes* (submitted).
4. K. Komorowski, A. Salditt, Y. Xu, H. Yavuz, M. Brennich, R. Jahn, and T. Salditt. Vesicle adhesion and fusion studied by small-angle x-ray scattering. *Biophysical Journal* (submitted).
5. Y. Xu, A. Dong, Y. Zhao, T. Zhang, Z. Jiang, S. Wang and H. Chen. Synthesis, Characterization and Biomedical Properties of UV-Cured Polyurethane Acrylates Containing a Phosphorylcholine Structure. *Journal of Biomaterials Science, Polymer Edition* (2012).

¹ These authors contributed equally

Acknowledgment

My studying in Germany has been full of remarkable experiences and meanwhile full of challenges. It is the kind help from many that has made this thesis possible. Here I would like to express my sincere gratitude to them.

At the beginning of my PhD program, I didn't have much idea of how things worked in this new institute and how people lived in this new country. Luckily many of my colleagues helped me out. They offered me a lot of helpful instructions and suggestions, both in and outside the lab. Therefore I would like to thank Dr. Anna-Lena Robisch, Aike Ruhlandt, Bastian Hartmann, Jan Goeman, Jochen Herbst, Karlo Komorowski, Kerstin Pluschke, Mareike Töpferwien, Dr. Marius Priebe, Dr. Markus Osterhoff, Dr. Marten Bernhardt, Dr. Martin Krenkel, Mike Kanbach, Peter Nieschalk, Dr. Sebastian Äffner, Sebastian Köhler, Sabine Balder, Dr. Tobias Reusch and also the other IRPers.

As I gained more knowledge of work and life here, I gradually started my own experiments in the lab as well as some collaborations with the group of Diederichsen, Janshoff, Jahn and Steinem. During this period of time, I received a lot of help from my collaborators in other groups and beamline scientists in synchrotron centers, besides from my colleges in IRP that I have mentioned above. For this I would like to thank Jan Kuhlmann, Torben-Tobias Kliesch and Dr. Ulrike Rost from the chemistry department of university göttingen, Dr. Jan Hilhorst from beamline ID01 of ESRF and Dr. Martha Brennich from beamline BM29 of ESRF.

I also would like to acknowledge Prof. Dr. Andreas Janshoff, Prof. Dr. Claudia Steinem and Prof. Ulf Diederichsen. Thank them for the helpful advice and discussions during the constructive collaborations on E- and K-peptide, SNARE proteins and β -peptides. In particular, I would like to thank Prof. Dr. Andreas Janshoff and Prof. Ulf Diederichsen for their supervision as my thesis committee members.

I am sincerely grateful to my doctoral supervisor, Prof. Dr. Tim Salditt. It is him that provides me this precious opportunity to study in this distinguished institute together with so many outstanding colleges, and to experience the incredible culture of this remarkable country. I have received patient and enlightening supervision from him within these four years, despite my non-physics scientific background. Moreover, I also appreciate his care about my living in göttingen and his attitude towards life outside science. What impresses me the most is the memorable Christmas evening with the Salditt family, and the hiking on La Bastille in Grenoble, France where we enjoyed breathtaking views.

In the end, I would like to thank SFB 803 "*Functionality Controlled by Organization in and Between Membranes*" of German Science Foundation (DFG) for the financial support, and "Göttingen Graduate School for Neuroscience, Biophysics and Molecular Biosciences" (GGNB) for organizing this international PhD program.

Curriculum vitae

Personal information

Name: Yihui Xu
Date of birth: 18. Oct. 1987
Place of birth: Yancheng, China
Citizenship: Chinese

Education

10/2012-present: PhD student and scientific employee in the Group of Tim Salditt, Institute for X-ray Physics, Universität Göttingen, Göttingen, Germany;
Member of the “International Max Planck Research School for Physics of Biological and Complex Systems” (IMPRS-PBCS) under “Göttingen Graduate School for Neuroscience, Biophysics and Molecular Biosciences” (GGNB);
Funded by German Science Foundation DFG (SFB 803)

09/2009-06/2012: Master student in the Group of Tao Zhang, Department of Materials Science & Engineering, Nanjing University, Nanjing, China

09/2005-06/2009: Bachelor student, Department of Materials Science & Engineering, Nanjing University, Nanjing, China

09/2002-06/2005: Yancheng Middle School, Yancheng, China

Previously, our group successfully characterized the effect of various lipids on the stalk formation in pure lipid multibilayers by means of x-ray scattering. In this model system, the energy required for stalk formation was supplied by the osmotic pressure of the aqueous vapor. Despite its remarkable simplicity and efficiency, the sample environment of this method was distinct from the fusion sites in vivo. This work aims to extend the x-ray study of stalk formation to more physiological conditions. To this end, efforts on three levels have been devoted, namely the lipid level, the peptide level and the protein level. On the lipid level, PEG solutions rather than aqueous vapor were used as the stressor to promote stalk formation in pure lipid bilayers. On the peptide level, D- β -peptides were incorporated into model lipid multibilayers to investigate its transmembrane behaviors. Lastly, on the protein level, a novel solvent-free protocol was developed, and SNAREs, a family of proteins which mediate vesicle fusion, were reconstituted into the multibilayers via the micelle-vesicle-multibilayer pathway.



ISBN 978-3-86395-304-1
eISSN 2512-6326

Universitätsverlag Göttingen